Responsive Space Launch with the Mark 41 Vertical Launching System

Master's Thesis

J. Provoost

TU Delft

Responsive Space Launch with the Mark 41 Vertical Launching System

Master's Thesis

by

J. Provoost

Student number: 4496493
Version: 1.1

Cover image credit: `https://www.aerospacemanufacturinganddesign.com/article/raytheon-receives-standard-missile-production-080816/`

Summary

For decades the space domain has been used for military purposes. When enemy forces establish counter-space capabilities, this could become a weakness. Responsive Space is a concept that focuses on replenishing lost capabilities or granting additional capabilities from space assets quickly. The continuous miniaturization of technologies has enabled small satellites to fulfill many desired functions. To launch such satellites, it might be possible to modify a missile into a small launch vehicle that can be launched from a naval ship using a shipborne missile canister launching system, the Mark 41 Vertical Launching System (VLS), thereby giving the military autonomous and quick-response space launch capability. Modifying a missile that has already been integrated in the VLS instead of developing a fully new launch vehicle could have the benefit that integration cost could be lower. Also, a fully new vehicle would require more development, which can be costly and time consuming. This has led to the following research question:

Is it technically feasible to launch a microsatellite from the Mark 41 Vertical Launching System by modifying an already integrated missile?

The Block IIA version of the Standard Missile-3 anti-ballistic missile is determined to be the most capable missile to modify. A multidisciplinary design optimization tool has been created that maximizes the payload mass and the perigee altitude of the orbit of the new launch vehicle. The payload mass includes the payload adapter mass and avionics mass of the upper stage.

The highest payload masses at a certain perigee altitude are found when launching from the equator to an equatorial orbit. Doing so achieves optimal solutions where a payload mass of 17.8 kg is found at an orbit with a perigee altitude of 200 km which decreases almost linearly to 12.1 kg at 700 km perigee altitude. So, a microsatellite can be launched to these orbits by the new launch vehicle.

Also, different launch locations and orbits are evaluated. The new launch location is chosen to be the main base of the Royal Netherlands Navy which has a latitude angle of 52.958 degrees and a longitude angle of 4.786 degrees. From this location the launch vehicle is launched to a polar orbit and an orbit with 58 degrees inclination. For a 58 degrees inclination orbit a payload mass of 15.8 kg at 200 km perigee altitude is reached and for the polar orbit 13.6 kg can be launched at the same perigee altitude. At 700 km perigee altitude, the values are 10.7 kg and 9.2 kg, respectively.

Sensitivity analyses have been performed to find the sensitivity of the solutions to uncertainties in several parameters and constraints. Also, possible changes in design parameters have been analyzed. The sensitivity analyses were performed for the equatorial orbit.

None of the uncertainties had such a large effect on the payload mass that they would prevent the launch vehicle from launching a payload mass of over 10 kg over the whole range of orbital altitudes. The largest effect from an uncertainty caused a change payload mass of roughly 1 kg. Choosing a chamber pressure close to the deflagration limit of the propellant or reducing the burn rate exponent can increase performance.

Preface

This report concludes my Master's thesis in Aerospace Engineering at Delft University of Technology. With my background of working in the navy, not everyone readily saw the logic of studying spaceflight. With this thesis I show that there are important common grounds between the two fields.

First, I would like to thank my TU Delft supervisor Marc Naeije for his support during the project and for remembering the contents of the Defence Innovation Game he attended, which ultimately led to me doing my thesis on this subject.
Also, I would like to thank my supervisors from TNO, Wouter Halswijk and Michiel Bergsma, for seeing the merit in me doing this research at TNO and their feedback and guidance during the project.

Furthermore, my thanks goes out to the guys from T-Minus Engineering for their enthusiasm and the time they took to help me.
Lastly, I would like to thank everyone who has in any way been a help to me in my endeavour of graduating for this Master in Aerospace Engineering.

J. Provoost
Delft, June 2020

Contents

List of Figures

List of Tables

Nomenclature

Latin Symbols

a	Semimajor axis	[m]
A_e	Nozzle exit area	[m^2]
A_t	Throat area	[m^2]
a_x	Axial acceleration	[m/s^2]
B	Set of neighbours, Spalding Number	[-], [-]
b	Atmospheric layer	[-]
c^*	Characteristic velocity	[m/s]
C_D	Drag coefficient	[-]
c_eff	Effective exhaust velocity	[m/s]
C_F	Thrust coefficient	[-]
C_L	Lift coefficient	[-]
C_p	Specific heat at constant pressure	[J/mol·K]
D	Drag	[N]
D_case	Motor case diameter	[m]
D_exit	Nozzle exit diameter	[m]
e	Eccentricity, Truncation error	[-], [-]
F	Gravitational force	[N]
f	Safety factor	[-]
f_F	Fanning friction factor	[-]
f_i	Sub-objective	
G	Gravitational constant	[m^3/kgs^2]
g_0	Gravitational acceleration on Earth	[m/s^2]
H	Geopotential altitude	[m]

h	Altitude, Step size	[m], [-]
h_α	Coefficient of convective heat transfer	[W/m^{2}K]
i	Inclination	[rad]
I_{sp}	Specific Impulse	[s]
k	Boltzmann constant	[Nm/K]
L	Lift	[N]
L_{case}	Motor case length	[m]
L_{con}	Length of the nozzle convergent section	[m]
L_{c}	Length of the cylindrical case section	[m]
L_{div}	Length of the nozzle divergent section	[m]
L_{e}	Length of the elliptical case top	[m]
$L_{\mathrm{M,b}}$	Molecular temperature gradient in layer b	[K/km]
M	Molecular mass, Mean anomaly, Mass, Mach number	[kg/mol], [rad], [kg], [-]
$\dot{m}$	Mass flow	[kg/s]
M_0	Initial mass	[kg]
$\dot{m}_{\mathrm{cr}}$	Critical mass flow	[kg/s]
M_{e}	End mass	[kg]
M_{f}	Fairing mass	[kg]
M_{n}	Nozzle mass	[kg]
M_{p}	Propellant mass	[kg]
M_{u}	Payload mass	[kg]
N	Total density number	[-]
n	Burn rate exponent	[-]
n	Burning rate exponent	[-]
N_{A}	Avogadro number	[mol^{-1}]
p_{a}	Ambient pressure	[bar]
p_{c}	Chamber pressure	[bar]
p_{e}	Exit pressure	[bar]

p_{t}	Nozzle throat pressure	[]
Pr	Prandtl Number	[-]
q	Dynamic pressure	[N/m^2]
q_α	Convective heat flux	[W/m^2]
Q_{c}	Convective heat flux at the stagnation point	[W/m^2]
R	Specific gas constant	[J/kgK]
r	Distance, regression rate	[m], [mm/s]
R^*	Universal gas constant	[J/molK]
R_{e}	Radius of the Earth	[m]
R_{g}	Maximum radius of the propellant grain	[m]
r_{TPS}	Regression rate of the TPS material	[m/s]
S	Reference area, burn surface	[m^2]
St	Stanton Number	[-]
T	Thrust, Temperature	[N], [K]
$t_{\mathrm{b,t}}$	Burn time in the case top	[s]
t_{b}	Burn time	[s]
t_{coast}	Coasting time	[s]
T_{c}	Chamber temperature	[K]
t_{e}	Wall thickness of the elliptical case top	[m]
t_{po}	Linear pitch angle decrease time during pitch-over	[s]
$t_{\mathrm{TPS,n}}$	TPS material thickness in the motor case at nozzle side	[m]
$t_{\mathrm{TPS,t}}$	TPS material thickness in the case top	[m]
T_{vac}	Vacuum thrust	[N]
T_{w}	Wall temperature	[K]
T_∞	Exo-atmospheric reference temperature	[K]
U	Flow velocity	[m/s]
U_{B}	Spherical harmonic potential	[J/kg]
U_{eq}	Equivalent exhaust velocity	[m/s]

U_e	True exhaust velocity	[m/s]
V	Velocity	[m/s]
v	Flow velocity	[m/s]
$V_\text{f,req}$	Required fairing volume	[m^3]
V_f	Volume of a cone frustum, Fairing volume	[m^3]
V_G	Ground speed	[m/s]
$V_\text{p,cyl}$	Propellant volume of the cylindrical section of the motor	[m^3]
$V_\text{p,t}$	Propellant volume of the case top section of the motor	[m^3]
w_i	Weighting factor	[-]
x	Vector of independent variables	
y_next	Value of the next integration step	[-]
Z	Geometric altitude	[m]
z^*	Reference point	[-]

Greek Symbols

α	Angle of attack	[rad]
γ	Flight path angle, Specific heat ratio	[rad], [-]
Γ	Vandenkerckhove function	[-]
δ	Latitude	[rad]
ε	Expansion ratio	[-], [-]
θ	Pitch angle, True anomaly	[rad], [rad]
λ	Set of weight vectors	[-]
Λ	Mass ratio	[-]
μ	Gravitational parameter	[m^3/s^2]
ξ	Bilinear tangent law exponent	[-]
ρ	Density	[kg/m^3]
ρ_p	Density of propellant	[kg/m^3]

ρ_{TPS}	Density of TPS material	[kg/m^3]
τ	Longitude	[rad]
ϕ	Propellant mass ratio	[-]
Φ	Increment per time step	[-]
χ	Heading angle	[rad]
ω	Argument of perigee	[rad]
Ω	Longitude of the ascending node	[rad]

Acronyms and Abbreviations

AAO	All-at-once
ACO	Ant Colony Optimization
AIS	Automatic Identification System
Al	Aluminium
AP	Ammonium-Perchlorate
ASAS	Advanced Solid Axial Stage
BMD	Ballistic Missile Defense
CBS	Cost Breakdown Structure
CEA	Chemical Equilibrium with Applications (NASA)
CEM	Cost Estimation Method
CER	Cost Estimation Relationship
CMDB	Composite Modified Double Base
COMM	Communication Infrastructures
CTPB	Carboxyl Terminated Polybutadiene
DTRM	Dual Thrust Rocket Motor
EO	Earth Observation
EP	External Population

ESA	European Space Agency
GA	Genetic Algorithm
GTOW	Gross Take-Off Weight
HRE	Hybrid Rocket Engine
HTPB	Hydroxyl Terminated Polybutadiene
ICBM	Intercontinental Ballistic Missile
IHS	Improved Harmony Search
ITAR	International Traffic in Arms Regulations
LEO	Low Earth Orbit
LRE	Liquid Rocket Engine
MDO	Multidisciplinary Design Optimization
MEOP	Maximum Expected Operating Pressure
MOEA/D	Multi-Objective Evolutionary Algorithm with Decomposition
NAFCOM	NASA Air Force Cost Model
NASA	National Aeronautics and Space Administration
NSGA2	Non-dominated Sorting Genetic Algorithm 2
PaGMO	Parallel Global Multiobjective Optimizer
PBAN	Polybutadiene Acrylonitrile
PSO	Particle Swarm Optimization
RK4	Runge-Kutta 4
RKF	Runge-Kutta-Fehlberg
SBIRS	Space-Based Infrared Surveillance Satellites
SEE	Standard Estimation Error
SIGINT	Signal Intelligence
SM	Standard Missile
SNaP	Strategic Command's Nanosatellite Program
SRM	Solid Rocket Motor
SSCM	Small Satellite Cost Model

TPS	Thermal Protection System
TSRM	Third Stage Rocket Motor
Tudat	TU Delft Astrodynamics Toolbox
TVC	Thrust Vector Control
USCM	Unmanned Space Vehicle Cost Model
VLS	Vertical Launching System
WBS	Work Breakdown Structure

1

Introduction

The space domain has been used for military purposes for decades. Operations Desert Storm and Iraqi Freedom showed that space systems effectuate a force-multiplication effect on military capabilities [15]. An enhanced situational awareness, high-speed global communications and GPS-guided munition all helped contribute to the success of the US military. However, the dependency on space capabilities can also become a weakness when enemy forces establish counter-space capabilities. To re-enforce the space force, the concept of Responsive Space was brought up. The goal of Responsive Space is to achieve the ability of having responsive, on-demand access to, through and from space. This quick access can be necessary to replenish a lost capability or grant additional capabilities to ongoing missions. An essential part in this is access to Responsive Space launch capabilities, also called Responsive Space Lift. Several concepts for these capabilities have been proposed in the first decade of the twenty-first century such as the use of air launch [16] and sea-launch [1]. The latter proposes the use of dedicated launch ships as shown in Figure 1.1. However, as a dedicated means of realizing Responsive Space Lift those concepts have not yet found their way into practice. In those articles it is assumed that to achieve the desired capabilities, a payload mass of at least a few hundred kilograms is needed. However, in the years since the publication of those articles, advances in satellites technology have enabled satellites of just a few kilograms to fulfill many of the desired functions. Additionally, the advances in launch vehicle technology have resulted in more powerful rockets in relation to their size. The technologies in these fields are still improving, but in their current state some interesting options for Responsive Space launch capabilities might be at hand.

The Royal Netherlands Navy is in possession of a technologically advanced fleet. This fleet contains four highly advanced air-defence and command frigates of the De Zeven Provinciën-class. These frigates feature the Mark 41 Vertical Launching System (VLS), a shipborne missile canister launching system. The Mk 41 VLS is installed below the deck of a ship. It consists of multiple canisters which can hold missiles for all kinds of engagements [2]. Three different versions of the Mk 41 VLS exist, which have different canister sizes. In this study, only the version used by the Royal Netherlands Navy is considered. This version accommodates missiles with a maximum length of 6.55 m (with the hatch closed, which is assumed to be required), 0.53 m diameter and a maximum encanistered weight of 4091 kg [17]. For this research, options will be investigated for using the Mk 41 VLS for Responsive Space Launch. No sources have been found that suggest that there is already a

Figure 1.1: Computer-generated image of a Cargo Ship Launching a Small Launch Vehicle [1]

military force in the world that has the capability of launching satellites from naval ships. It could, however, be of great value as it gives the opportunity to fully exploit the force-multiplication of space assets wherever that is required for the mission, with the additional advantage of a much more flexible launch site by launching from sea. If a launch vehicle is designed that fits inside the Mk 41 VLS canister, it will be the smallest orbital launch vehicle according to the Guinness Book of World Records, which lists the current record to be held by the Japanese SS520-5 launch vehicle [18].

To achieve a Responsive Space launch capability with the Mk 41 VLS, assuming no qualified missile already exists, two options can be distinguished.

The first option is to design a launch vehicle from scratch and integrate it with the existing VLS infrastructure. This option gives a lot of potential for optimization and could therefore produce a very capable solution. However, the whole process of development, integration and qualification for use of a naval vessel of a new system will probably be very costly and time-consuming.

The second option is to use an already qualified and integrated missile and modify it to accommodate its new functionality. If the missile is modified only slightly, the integration and qualification process will be much easier. This could make this option cheaper, faster to realize and therefore overall more realistic. Therefore, the second option is investigated in this thesis research.

For the VLS, a range of missiles is qualified, of which some are interesting to study for Responsive Space applications. In Figure 1.2 some of the qualified missiles are depicted in the Mk 41 VLS. Eight different types of missiles can currently be launched with the VLS. These missiles are designed for different purposes and can be divided into categories. First there is the category of anti-aircraft missiles. The anti-aircraft missiles are the RIM-66 Stan-

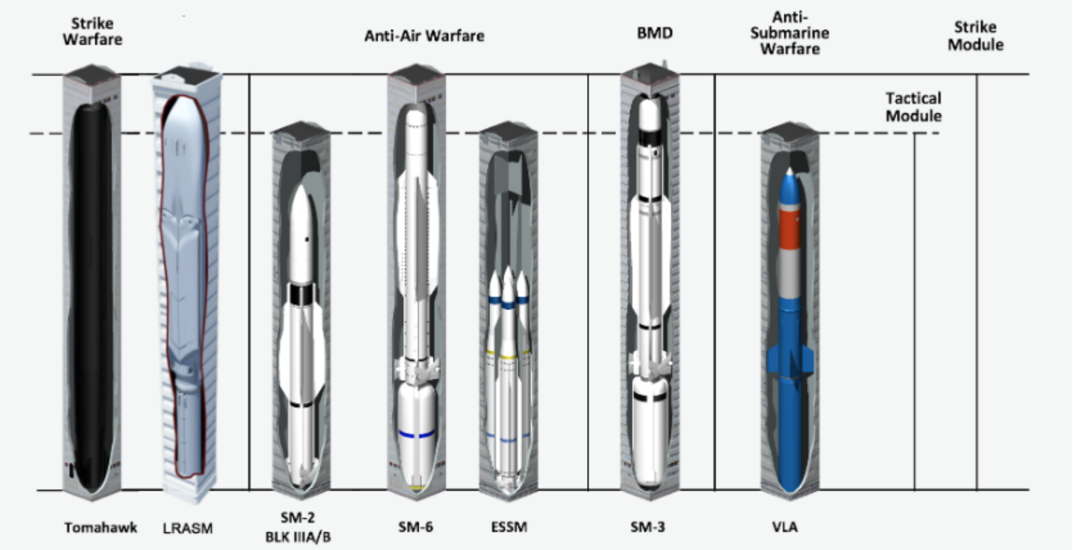

Figure 1.2: Some of the qualified missiles of the Mark 41 VLS depicted in the canister [2]

dard Missile 1 and 2, RIM-67 Standard Missile 1ER/2ER, RIM-174 Standard ERAM or Standard Missile 6 (SM6), RIM-7 Sea Sparrow, and RIM-162 ESSM. It can also launch a type of cruise missile, the RGM-109 Tomahawk, an anti-submarine missile, the RUM-139 VL-ASROC (VLA in Figure 1.2) and the RIM-161 Standard Missile 3 (SM-3), which has the purpose of intercepting short and intermediate range ballistic missiles. The LRASM shown in Figure 1.2 is a Long Range Anti-ship Missile, which could be integrated in the VLS in the future. Of these qualified missiles the RIM-161 Standard Missile 3 is the most likely candidate. Current versions of the other missiles all have limited deltaV performance and are unlikely to be made capable of satellite launch with moderate modifications. The Block IIA variant of the SM-3, which is manufactured by Raytheon and Mitsubishi Heavy Industries, has the best kinematic performance compared to the other missiles including the Block IB variant of the SM-3. The SM-3 shown in Figure 1.2 is the Block IB version. The Block IIA is reported by multiple sources to have a burn-out velocity of 4.5 km/s, which is significantly higher than the 3.0 km/s that is reported by sources for the Block IB [9, 19, 20]. However, these numbers have not been confirmed officially.

A burn-out velocity of 4.5 km/s is obviously not enough for satellite launch as for Low Earth Orbits (LEO) an orbital velocity of around 7.9 km/s is required. Also taking gravity and drag losses into account makes that the total required deltaV is 1-1.5 km/s larger than the orbital velocity [17]. For this reason the missile needs to be modified. An extra stage is needed to produce the additional deltaV. Adding extra stages and boosters has been put into practice earlier to modify intercontinental ballistic missiles (ICBM) to be used as a launch vehicle. A study has been found in which a conceptual design of the Peacekeeper ICBM is discussed for space launch capabilities [21]. However, with the use of the Mk 41 VLS, a big challenge lies in accommodating the launch vehicle to the Mk 41 VLS canister, which gives strict dimension constraints. Such constraints are much more lenient when modifying an ICBM and, thus, such a problem becomes quite different.

The following research question is established:

Is it technically feasible to launch a microsatellite from the Mark 41 Vertical Launching System by modifying an already integrated missile?

By definition, a microsatellite is a satellite with a mass between 10 and 100 kg. To help answer the research question, sub-questions are established:

What is the optimal performance in terms of payload mass in orbit of the new launch vehicle?

another sub question is:

How does a change in launch conditions and target orbit affect the optimal design?

and also:

How sensitive is the optimal solution to uncertainties in parameters?

In the design of a modified missile, many different disciplines play an important role and are interconnected. Therefore, this research will be focused on a multidisciplinary design optimization (MDO) of the modified Standard Missile-3 to fit its new functionality as a launch vehicle. Many different studies have been conducted on the multidisciplinary design optimization of complete launch vehicles [11, 14, 22–27]. Some are focused on conventional launch vehicles and some on air-launched launch vehicles. These studies have the same goal of designing an optimized launch vehicle, albeit for different optimization objectives. These studies give a valuable insight into the multidisciplinary design optimization of a launch vehicle.
Modifying an SM-3 to a launch vehicle is not cheap. The fiscal year 2014 price of an SM-3 Block IIA is reported to be 24.3 million dollars [19]. However, the Block IB price dropped from 11.6 million dollars in 2011 to 8.5 million dollars in 2015, which is a price decrease of 27% [19]. The idea that modifying an SM-3 could be a cost-effective method comes from the fact that integration cost could be significantly lower when using a launch vehicle that has for a large part already been integrated with the launch system. Also, development and manufacturing would be more costly and time consuming when creating a whole new launch vehicle. However, estimating the cost for using a modified SM-3 as a launch vehicle is a difficult task. It is likely that certain subsystems of the SM-3 are not required when it is used as a launch vehicle. This could possibly reduce unit cost significantly. Unfortunately, no detailed breakdown of subsystems is available for the SM-3. Thus, obviously, it is not known which subsystems contribute most to the total unit cost or whether they can be omitted when the missile is used to launch a satellite either. A meeting with a TNO costing expert also led to the conclusion that not enough data on the system or similar cases is available to accurately determine integration cost. Additionally, determining the cost of the small new upper stage turned out to be a difficult task. Cost models are valid for a limited range of parameter values. The parameters used to determine the cost are often parameters such as total mass or subsystem mass. The lower boundaries for these parameters

in the cost models are, even for cost models for small launch vehicles, significantly larger than the values that occur in the generated upper stages in the MDO. They can therefore not be used for accurate estimation of the new upper stage cost. Also, meetings with rocket engineers from T-Minus Engineering did unfortunately not lead to a valid cost estimation method.
A detailed cost analysis can therefore not be included in this thesis research.

1.1. Applications of Payloads of the New Launch Vehicle

The goal of the system is to acquire a certain operational capability by inserting a payload into orbit. The launch vehicle is just the means to bring to payload to the desired orbit. To have an idea of the utility of such a launch vehicle, it is therefore important to determine the applications that the payloads can have. A small vehicle that can fit in the Mk 41 VLS canisters, can only be used to launch small payloads. The SS520-5, the smallest orbital launch vehicle, successfully launched a 4 kg cubesat into an 30.78 degree inclination orbit with perigee and apogee altitudes of 183 km and 2010 km, respectively. Using the vis-viva equation, it can be determined that such an orbit requires the same orbital energy as a circular orbit at approximately 1000 km altitude [28]. It is also important to mention that the SS520-5 was not a fully optimized launch vehicle. It was based on the SS520 sounding rocket, supplemented with a commercial-of-the-shelf (COTS) solid rocket motor [18]. The new launch vehicle might be more optimized, but will also be smaller than the SS520-5. Some examples of applications of low mass satellites that the new launch vehicle might be able to carry to orbit will be discussed here.

Communication

Small satellites are used for communication between a lot of different units. For example, it can be used for a tactical data link between fighter jets or beyond-line-of-sight communications for the warfighter on the ground [29, 30]. A good example of this are the U.S. Army Space and Missile Defense Command/Army Forces Strategic Command's Nanosatellite Program, or SNaP. SNaP is a small satellite communication constellation used to enable communication using existing UHF tactical radios. SNaP satellites are 5 kg cubesats which have a size of a loaf of bread. A mobile launch platform such as a ship could also be used to launch satellites for communication in hard to reach places [17].

Surveillance and Reconnaissance

For a military force it is important to have a good situational awareness. It is therefore important to gather as much information as possible. Surveillance is the act of monitoring behaviour and communication to gather intelligence. Reconnaissance is very similar, but has the difference that the intelligence is gathered from non-friendly areas.
An example of this are the space-based infrared surveillance satellites (SBIRS) that are used to detect ballistic missile launches early [31]. Another example is the use of pico-satellites for maritime security applications [32]. A pico-satellite has a mass between 0.1 and 1 kg. Such satellites are proposed to use for surveillance in the maritime domain to detect activities such as piracy and cross-border illegal activities such as human trafficking or illegal transportation of goods.

Navigation

Usually for navigation GPS is used to keep track of the user's position. However, also small satellites can be used for navigation purposes [33]. The paper proposes a nano-satellite constellation for regional navigation for Indonesia. The proposed satellites in the constellation each weigh 3 kg.

1.2. Outline Thesis Report

The ordering of the chapters 2 to 5 is based on the order of actions in the MDO tool. After the introduction, in Chapter 2 MDO will be discussed. Also, an optimization algorithm is chosen and explained. In Chapter 3 the first discipline in the MDO will be discussed, which is the propulsion system. After some general information on solid rocket motors, the model used in the MDO will be explained and validated. Then, the launch vehicle model will be discussed in Chapter 4. It will be explained how the aerodynamic coefficients are determined and how the SM-3 Block IIA is modeled. The trajectory is discussed in Chapter 5. In that chapter the ascent environment, guidance and numerical integration are explained. At the end, the trajectory model is validated. After all disciplines have been explained, the generated results are shown and evaluated in Chapter 6. In Chapter 7 a sensitivity analysis is performed on several parameters after which a conclusion can be drawn in Chapter 8. Chapter 8 ends with recommendations for future research.

2

Optimization

Optimization is the process to find the best solution to a problem. Actually, in all decisions that are ever made, some kind of optimization process plays a role. Engineering problems always are optimization problems to a certain extent. Also in this research project, optimization techniques will be used to find an optimal solution for the determined objectives. The optimization problem for this thesis research will come in the form of a multidisciplinary design optimization. In this chapter, the theory behind the optimization techniques used will be addressed.

2.1. General Optimization Problem

First, the basics of optimization are discussed. The goal of an optimization problem is to determine a set of n independent variables $\mathbf{x} = (x_1, x_2, \ldots, x_N)^T$ that will minimize or maximize the function value of a function $f(\mathbf{x})$. The problem often has constrains in the form of equality constraints $h(\mathbf{x})$ and inequality constraints $g(\mathbf{x})$. The full general mathematical description of a minimization problem will be given below [34]:

$$min\, f(\mathbf{x}) \tag{2.1}$$

Which is subject to:

$$\mathbf{h}(\mathbf{x}) = 0 \text{ for } j = 1, 2, \ldots i \tag{2.2}$$

$$\mathbf{g}(\mathbf{x}) \geq 0 \text{ for } j = i+1, \ldots, n \tag{2.3}$$

$$x_j^L \leq x_j \leq x_j^U \text{ for } j = 1, 2, \ldots, n \tag{2.4}$$

in which i is the number of equality constraints and $n - i$ the number of inequality constraints. The number of inequality constraints is unlimited, however, the number of equality constraint can not be bigger than the number of variables. To transform this minimization problem into a maximization problem simply multiply the objective function with a factor -1.

2.2. Multidisciplinary Design Optimization

Multidiscipinary design optimization (MDO) is a field of engineering that has gained popularity in many different fields over the last decades. In MDO the optimization of multiple disciplines or subsystems is done simultaneously. The idea driving MDO is that the total performance of a system is not only affected by the individual performances of disciplines or subsystems, but also the interaction between them. One of the bigger challenges in MDO is to adequately handle the coupling between the different disciplines. A particular discipline might need the output of another disciplines as input. Also, incorporating a lot of different disciplines can increase computation time significantly.

Different MDO architectures can be used, the distributed architecture and the monolithic architecture. The distributed architecture decomposes the problem into subproblems and optimizes them separately, after which an overall optimizer is used to combine subproblems. Here, a monolithic architecture will be used, which means that one global optimizer is used to optimize the complete MDO problem. Also, the MDO will use an all-at-once (AAO) approach, meaning that all types of variables and constraints are written in the problem statement.

The MDO will be performed with Tudat (TU Delft Astrodynamics Toolbox). Tudat is a C++ environment that is used for simulations in the field of astrodynamics. It has been developed within the Astrodynamics & Space Missions section of the faculty of Aerospace Engineering of the TU Delft. It has been designed focusing on modularity. The library contains, for example, a good range of relevant reference frames, environmental models and numerical integrators, the latter two will be discussed in later chapters. Along with Tudat, use will be made of the Parallel Global Multiobjective Optimizer (PaGMO). PaGMO is a platform in C++ and a scientific library for massively parallel optimization. It is built with the goal of providing a unified interface for optimization algorithms and for optimization problems and to make their usage in massively parallel environments simple [35]. The use of PaGMO comes with the advantage that it can be used in conjunction with Tudat. Tudat and PaGMO have been used successfully in many earlier thesis research projects, including ones with similar applications [14, 26].

2.3. Optimization Algorithms

To optimize the problem, an optimization algorithm is required. Two types of algorithms are distinguished here; gradient-based algorithms and heuristic algorithms.

Gradient-based algorithms require gradient information to converge to a minimum. The solution that the algorithms converge to is a local minimum. Only if the objective function is convex, it can be concluded that the local minimum found is also the global minimum. In an MDO with many design variables and complex coupling between disciplines, the objective function is unlikely to be convex. Consequently, to converge to the global minimum a good initial guess is needed, but finding the right initial conditions needs an optimization in itself. Therefore, gradient-based methods will not be used for the MDO.

Instead, use will be made of heuristic algorithms. Heuristic algorithms give the possibility of working with non-differentiable functions and constraints whereas gradient-based algorithms need some differentiability of the objective and the constraints [11]. Heuristic methods are global optimization methods. The search for the optimum is performed in a stochastic manner. A disadvantage of the use of heuristic algorithms is that a lot of computation effort may be needed to find a good solution depending on the complexity of the problem and, because of the random behaviour, there may not be a clear convergence. However, they are relatively easy to use and no detailed insight in the problem is needed.

Developing a well-functioning heuristic algorithm is very time-consuming. For that reason, using PaGMO comes with a big advantage. PaGMO contains verified versions of a lot of different optimization methods, such as Genetic Algorithms (GA), Evolutionary Algorithms (EA), Particle Swarm Optimization (PSO), Ant Colony Optimization (ACO) and more [35].

2.4. Objectives

The exact missions that the launch vehicle will be used for are not yet known. It is therefore important to determine the performance over a range of orbits. Thus, the objective is to find the maximal payload capability of the launch vehicle for the relevant range of orbits. More specifically, the two objectives will be the payload mass and the perigee altitude of the orbit, which both are to be maximized. Perigee altitudes from 200 km to 700 km will be evaluated. The constraints that affect these objectives will be discussed in the chapters of the disciplines they occur in.
Thus, the optimization will be a multi-objective optimization.

2.5. Multi-Objective Optimization

For a single-objective optimization problem the optimal solution would simply be the smallest or largest value that can be found. For a multi-objective problem a different method must be implemented to determine the optimum. A method that is very commonly used is combining multiple objectives into a single scalar objective function f_{tot} by multiplying the sub-objectives f_i with a weighting factor w_i [36]:

$$f_{tot} = \sum_{i=1}^{j} w_i \cdot f_i \tag{2.5}$$

with

$$\text{all } w_i > 0, \quad \sum_{i=1}^{j} w_i = 1 \tag{2.6}$$

However, even though the use of a multi-objective algorithm is no longer needed when using this algorithm, determining suitable values for the weight factors is a difficult process.

Another method is the use of Pareto Optimality to rank the solutions. A local Pareto set is a collection of individuals that has the best performance when all objectives are taken into account. A Pareto improvement makes a one or more objectives of an individual better, without making any other objective worse. When no more Pareto improvement is possible, Pareto Optimality has been achieved. When the first Pareto front is found, it can be removed from the population to find the second and so-forth [3]. In this way a ranking can be made of Pareto fronts. An example of this is shown in Figure 2.1. The figure shows a population of 500 individuals for an arbitrary problem that minimizes sub-objectives f_1 and f_2. In the figure the first Pareto front (the individuals with the best performance) and some arbitrary higher ranked Pareto fronts have been highlighted with a blue line.

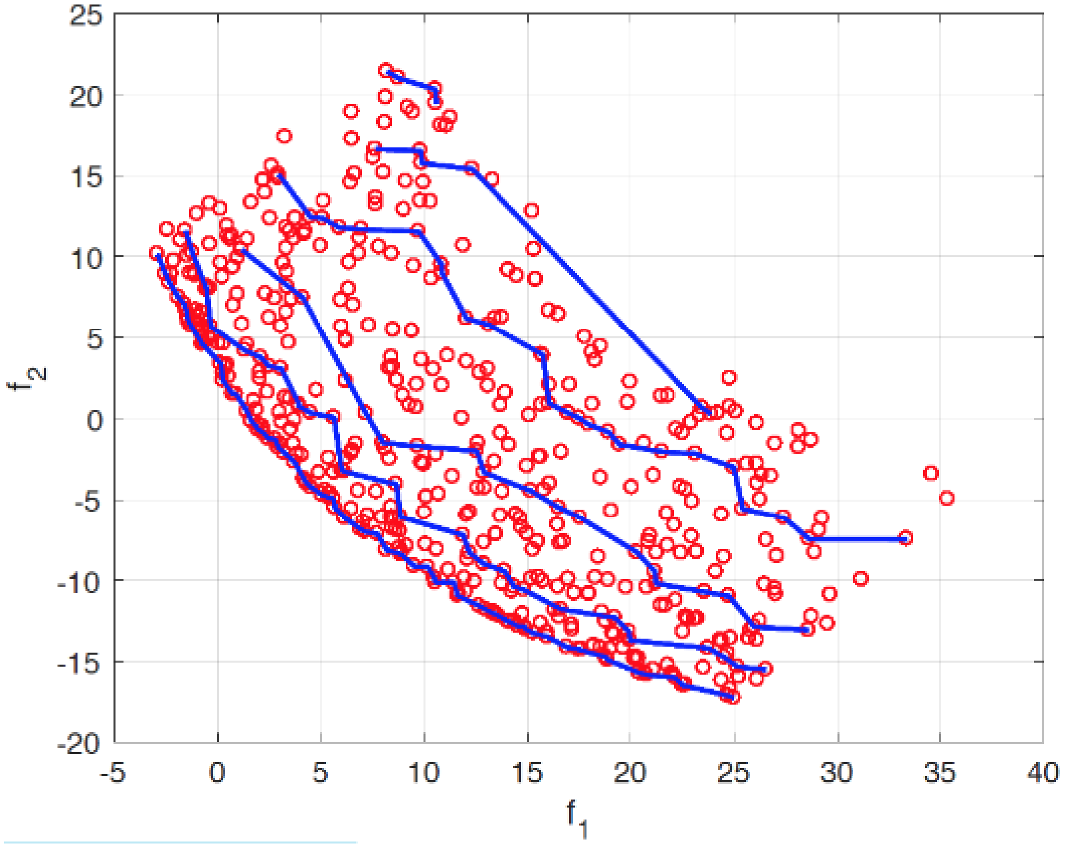

Figure 2.1: Ranking of Pareto fronts for an arbitrary minimization problem of two objectives [3]

2.6. Algorithm Choice

In the version of Tudat and PaGMO that is used, only three multi-objective optimization methods are available. The three methods available are the Improved Harmony Search (IHS), Non-dominated Sorting Genetic Algorithm (NSGA2), and Multi-objective Evolutionary Algorithm with Decomposition (MOEA/D) [35]. The methods have been evaluated with testing and found research.

With testing, the IHS method showed a very limited range of solutions in the final generations and it went through the generations so quickly that is seemed that it did not function properly. Tweaking of the settings did not improve the performance. The IHS method is therefore omitted from the options for the MDO.

An advantage of the NSGA2 optimizer is that it has the aim to find multiple Pareto optimal solutions with good diversity [37]. NSGA2 has been used successfully in optimization problems before [38, 39]. However, literature suggests that MOEA/D should outperform NSGA2 in most cases in terms of solution quality and computational efficiency [40–42]. Though, it also states that MOEA/D might not work very well if the solutions to neighbouring sub-problems are not very close in the design space. This problem could be overcome by choosing the correct settings. Determining these settings, however, can be hard and time consuming. A recent Master's thesis concluded that the use of the MOEA/D method was better than NSGA2 for the optimization of the ascent trajectory of a spaceplane. In that thesis the standard settings of MOEA/D in Pagmo were used [43]. Therefore, it is chosen to use MOEA/D for the optimization. The working principles of the method are explained in the next section.

2.6.1. MOEA/D

The Multi-Objective Evolutionary Algorithm with Decomposition was introduced in 2007 [42]. The algorithm decomposes the multi-objective optimization problem into a number of scalar optimization sub-problems, which are then optimized simultaneously. For the optimization of each sub-problem only information from the neighbouring sub-problems is used, which is the reason why this algorithm is less computationally complex than, for example, NSGA-2. Three approaches can be used for decomposition; the weighted-sum approach, the Tchebycheff approach and the boundary intersection (BI) approach. Testing has shown that the weighted-sum approach did not create a diverse Pareto front. It only optimized near the boundaries of the evaluated range of perigee altitudes. The Tchebycheff and BI approaches did create a more diverse Pareto front. However, the Tchebycheff method optimized the front slightly better. It is therefore chosen to use the Tchebycheff method furtherly. It has also been used successfully in earlier thesis research [43]. The test results can be found in Appendix D. For the Tchebycheff approach, the scalar optimization problem is represented by [42]:

$$\text{minimize } g\left(x|\lambda, z^*\right) = \max_{1\leq i\leq m}\left\{\lambda_i\left|f_i(x) - z_i^*\right|\right\} \tag{2.7}$$

Here, $z^* = \left(z_1^*, \ldots, z_m^*\right)^T$ is called the reference point, which means that $z_i^* = \max\left\{f_i(x)\right\}$ for each $i = 1, \ldots, m$. For every Pareto optimal point x^* a weight vector λ exists such that x^* is the optimal solution of Equation 2.7 and each optimal solution of Equation 2.7 is a Pareto optimal solution of the overall optimization problem. Then when the weight vector is altered, different Pareto optimal solutions can be found. A step-wise breakdown is given of the working mechanism of the algorithm [44]:

1. Initialize:
   - 1.1. An external population (EP), which is a vector consisting of non-dominated solutions (or Pareto solutions) encountered during the search, is initialized.
   - 1.2. For a set of N evenly spread weight vectors, the Euclidean distances are computed between any two weight vectors and then the T nearest weight vectors are determined for each weight vector. For each sub-problem $i = 1, \ldots, N$ set $B(i) = \{i_1, \ldots, i_T\}$, where $\lambda^{i_1}, \ldots, \lambda^{i_T}$ are the nearest weight vectors to weight vector λ^i.
   - 1.3. A random initial population is generated and the corresponding objective function values are determined.
   - 1.4. The reference point vector z^* is initialized, in which the best solutions are stored for all sub-problems.
2. Population is updated, for $i = 1, \ldots, N$ the next steps occur:
   - 2.1. A random number v is generated from an uniform distribution $[0,1]$. The solution is compared with δ, which is the probability that parent solutions are selected from the neighbourhood. Then:

$$P = \begin{cases} B(i) & \text{if } v < \delta \\ \{1, \ldots, N\} & \text{otherwise.} \end{cases}$$

- 2.2. $a = i$ and two entries b and c are randomly selected from P. Then from x^a, x^b and x^c a new solution $\bar{y}$ is obtained. Then considering mutation probability, a mutation operator is performed on solution $\bar{y}$ to obtain solution y.
- 2.3. If a design variable of the new solution is outside of its allowed range, the value is reset to a random value inside the boundaries of the variable.
- 2.4. The reference point vector z is updated. For each $j = 1, \ldots, m$, if $z_j > f_j(y)$, then $z_j = f_j(y)$.
- 2.5. $q = 0$ and q is compared with n_r, which is the maximal number of solutions replaced by each child solution. An entry j is randomly picked from P. If $g\left(y|\lambda^j, z\right) \leq g\left(x^j|\lambda^j, z\right)$, then $x^j = y$ and the objective function values are updated correspondingly. Then, $q = q + 1$ and entry j is removed from P. This is repeated until $q = n_r$.

3. It is evaluated if the stopping criterion has been satisfied. In this research a maximal number of generations will be used. If the stopping criterion is satisfied, the search is stopped. If not, a reiteration occurs from step 2.

The optimizer settings used in this research will be mostly the standard settings in PaGMO [35]. For reproducibility, the settings will be stated explicitly here. A grid approach is used for weight generation. The constants used for Differential Evolution, C_R, F and η_m are 0.9, 0.5 and 20, respectively. The probability that the whole population is considered instead of just the neighbourhood is set to 0.9. The maximum number of copies reinserted in the population n_r is set to 2. The diversity preservation mechanisms are set to true. The only setting that is changed is the size of the weights neighbourhood. The standard for this setting is 10. Different values for this setting were tested. Although the differences were small for the largest part of the range of perigee altitudes, a neighbourhood size of 40 had a slightly more developed Pareto front at lower orbital altitudes after 400 generations. Therefore, this setting is set to 40 for the simulations in this report.

It was found that using the unchanged values of the payload mass and perigee altitude as objectives did not create a diverse Pareto front. It would prioritize the perigee altitude and almost all individuals would converge to higher perigee altitudes. Trial and error with different scaling values has shown that scaling the payload mass with a factor of 125 in the objective function would create a diverse Pareto front that had a good distribution of individuals along the entire range of perigee altitudes. Therefore, for all simulations the payload mass will be multiplied with a factor of 125 in the objective function. The values for the perigee altitudes will be unchanged.

3

Propulsion

In this chapter, the modeling of the propulsion will be discussed. To have accurate results for the dynamic simulation, an accurate propulsion system model is required. The accelerations of the launch vehicle are directly dependent on the performance of the propulsion system. The first three stages of the Standard Missile 3 are set and therefore only the fourth stage will be optimized. First, general information on rocket propulsion is given. Then it is shown how the performance of the propulsion system is evaluated and how the upper stage is optimized. The methods for determining the mass of the propulsion system is also included in this chapter.

3.1. Chemical Rocket Propulsion

In this section, general information about chemical rocket propulsion is discussed. The contents of this section apply to all types of chemical rocket engines (solid, liquid, hybrid). Chemical propulsion is the most used type of propulsion. In a chemical rocket the energy is stored internally in the propellant and is released through a chemical reaction. Then, a working fluid is heated in the combustion chamber and accelerated through an exit nozzle. Then, in accordance to Newton's Third Law, the change in momentum of the fluid also causes a force to act on the rocket. This force is called the thrust force. The thrust force is one of the main forces exerted on a launch vehicle, especially at higher altitude. Therefore, it is an important factor to determine for evaluating the dynamics of a launch vehicle. In an atmosphere environment the thrust is written as [5]:

$$T = \dot{m} \cdot U_\mathrm{e} + A_\mathrm{e} \cdot \left(p_\mathrm{e} - p_\mathrm{a}\right) \tag{3.1}$$

where $\dot{m}$ is the mass flow rate, U_e is the true exhaust velocity, A_e is the nozzle exit area, p_e is the exit pressure and p_a is the ambient pressure. In Equation 3.1 on the right hand side, the first term is called the moment thrust and the second term is called the pressure thrust. In a vacuum the ambient pressure is zero and the pressure thrust is only the product of the nozzle exit area and the exit pressure. Ideal expansion is the situation when the exit pressure is equal to the ambient pressure. With ideal expansion a maximum efficiency is achieved.

3.1.1. Ideal Rocket Theory

When some assumptions are made, it is possible to use analytical expressions for modeling a chemical rocket. These assumption are quoted from [45]:

1. The working substance (or chemical reaction products) is homogeneous.
2. All the species of the working fluid are gaseous. Any condensed phases (liquid or solid) add a negligible amount to the total mass.
3. The working substance obeys the perfect gas law.
4. There is no heat transfer across the rocket walls; therefore, the flow is adiabatic.
5. There is no appreciable friction and all boundary layer effects are neglected.
6. There are no shock waves or discontinuities in the nozzle flow.
7. The propellant flow is steady and constant. The expansion of the working fluid is uniform and steady, without vibration. Transient effects (i.e., start up and shut down) are of very short duration and may be neglected.
8. All exhaust gases leaving the rocket have an axially directed velocity.
9. The gas velocity, pressure, temperature, and density are all uniform across any section normal to the nozzle axis.
10. Chemical equilibrium is established within the rocket chamber and the gas composition does not change in the nozzle (frozen flow).
11. Stored propellants are at room temperature. Cryogenic propellants are at their boiling points.

Even though with these assumptions the real performance of a rocket can be approximated, these assumptions are not realistic and in reality a rocket motor is never ideal. Therefore, corrections will need to be made on the output of the propulsion system to account for losses that are not taken into account by Ideal Rocket Theory. The correction factors will be determined when validating the propulsion system model.

3.2. Solid Rocket Motor Modelling

Besides the liquid fuel used in the Tomahawk's air-breathing engine, all motors of the missiles qualified for the Mark 41 VLS are solid-propelled. The reason for that is that for military applications solid rocket motors give relevant benefits. Most importantly, solid rockets can be stored for a long time without attention and can then be fired reliably without preparation. This makes them more operable than liquid rocket engines (LRE) or hybrid rocket engines (HRE), which may need a lot of preparation time. Solid rocket motors (SRM) are simpler than liquid propellant rockets and are therefore cheaper and easier to develop. And lastly, SRMs are usually more compact because of the high density of the propellant. This is an advantage, because the dimension restrictions of the VLS make it desirable to use high density propellants.

For these reasons, it is chosen to also model the fourth stage as a solid rocket motor. Therefore, the next sections will be used to explain the basics of solid rocket motors and, furtherly, how the propulsion system is optimized for this research.

3.2.1. Basic Configuration of the SRM

Thermodynamically a solid propellant engine is identical to a liquid rocket engine. However, SRMs have fewer complicated components and thus differ quite a bit. In Figure 3.1, a schematic is given of a basic SRM.

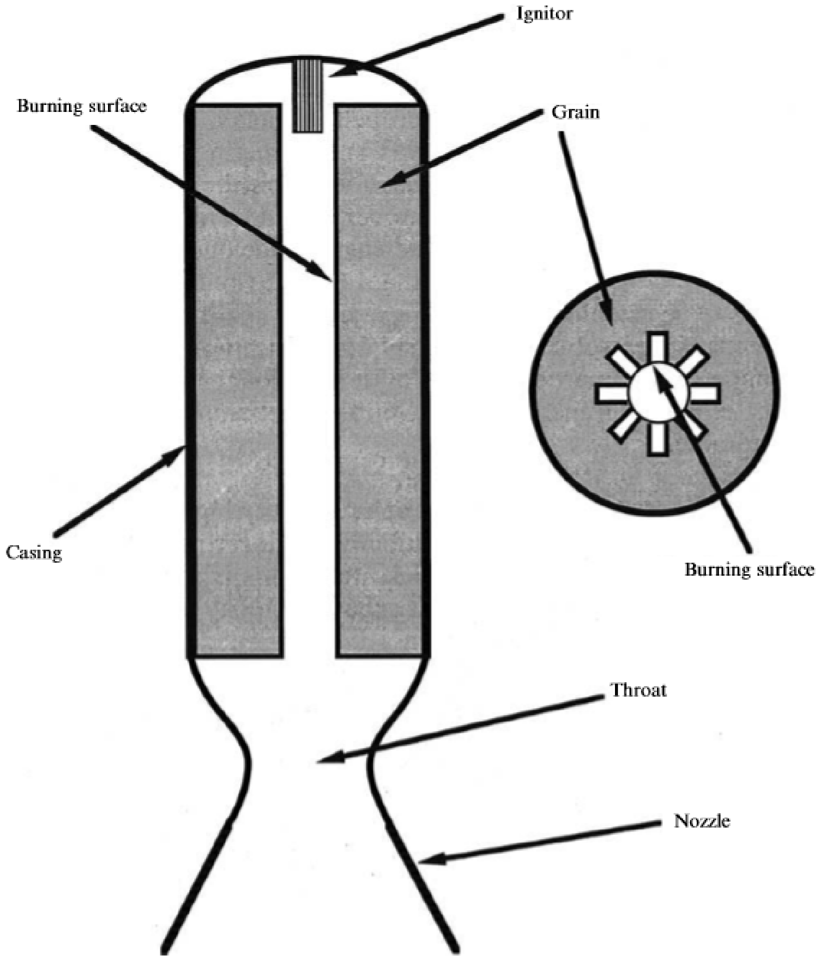

Figure 3.1: Illustration of solid-fuelled rocket motor[4]

The motor casing is often a cylindrical or spherical cover that holds the propellant grain, insulation and igniter. The casing must be designed to be able to withstand the high pressures that form in the combustion chamber as well as the thermal load. Usually safety factors are applied as an extra insurance that the structure is strong enough. Also, forces during flight must be withstood, such as the bending load or axial acceleration. Solid rocket motors do not have any form of active cooling and hence uses insulation to protect the casing from overheating [4]. The grain is set off by the igniter. The igniter is an electrically activated device that gives enough energy to initiate the combustion [45]. The grain will

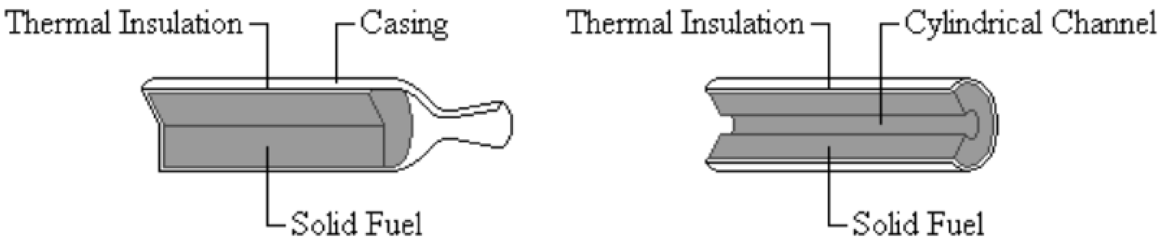

Figure 3.2: Illustration of the two main types of propellant grain for solid rocket motors; end-burning (left) and internal-burning (right) [5]

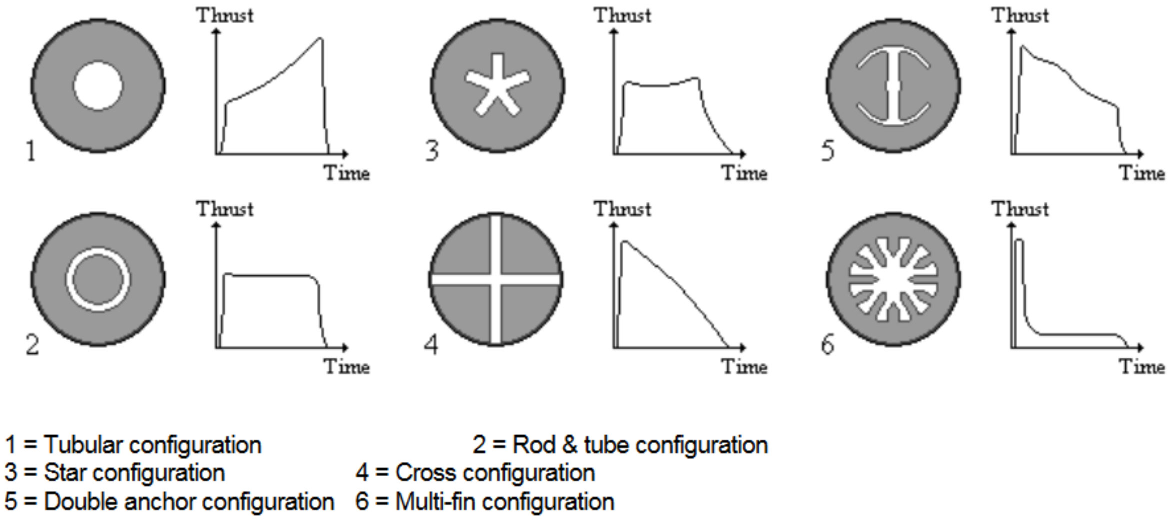

Figure 3.3: Internal-burning grain designs with their thrust-time profiles [5]

then start to burn at its exposed surfaces in the combustion chamber. Typically 82%-94% of the total motor mass is occupied by the propellant [45]. The propellant grain can have many different types of configurations, which each induce a different type of thrust profile. Three types of burning can be distinguished:

- Neutral burning grain: the thrust remains constant during the burn
- Progressive burning grain: the thrust increases during the burn
- Regressive burning grain: the thrust decreases during the burn

Two main types of grain configurations are used in spaceflight, the end-burning grain and the internal-burning grain (see Figure 3.2). The end-burning grain has a smaller burn surface than the internal-burning grain. End-burning geometries have been used in research for upper stage engines [23]. However, they are not often seen in real launch vehicles. The larger burning surfaces of the internal-burning grains can generate a higher thrust which of often advantageous, especially for lower stages. Figure 3.3 shows some options for internal-burning grains and their thrust profile with time. Figure 3.3 shows that internal-burning grains can be neutral, progressive or regressive. The thrust profile changes as the shape of the grain geometry changes during the burn. An example of this shape change is shown in

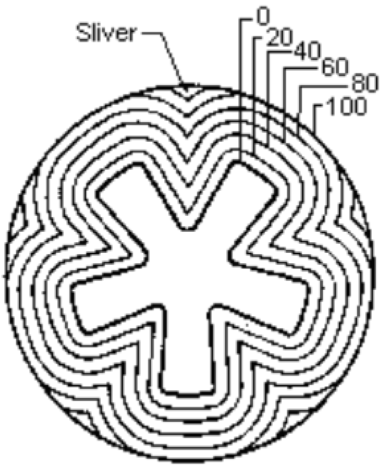

Figure 3.4: Evolution of burning area in time [5]

Figure 3.4. Slivers are parts of the grain that are not used and remain in the motor casing at the end of the burn. The mass flow from the grain of a SRM is determined with:

$$\dot{m} = \rho_{\mathrm{p}} \cdot S \cdot r \tag{3.2}$$

where ρ_{p} is the density of the propellant, S is the burning surface and r is the regression rate of the grain. The regression rate can be approximated well with De Vieille's law in which it is related to the chamber pressure:

$$r = a \cdot p_{\mathrm{c}}^{n} \tag{3.3}$$

where a is called the burning rate coefficient and n the burning rate exponent.
The gas generated in the chamber flows through a convergent-divergent nozzle. The nozzle is designed to optimize the conversion from internal energy to kinetic energy.

3.2.2. Solid Propellant

Propellant choice is an important step in the design of a rocket motor. In this section the main propellant classes will be discussed; homogeneous propellants and heterogeneous propellants. For this section [5] and [4] will be used.
Homogeneous propellants are propellant where the fuel and oxidizer belong to the same molecule. An example of a homogeneous propellant is nitrocellulose, which is also a single base propellant. Homogeneous propellants can also be double or triple base propellants.
The second class are the heterogeneous propellants. These propellants are made up of a separate fuel and oxidizer in initially liquid plastic or rubbery binder material. The most encountered modern solid propellant is based on polybutadiene synthetic rubber binder with an oxidizer of ammonium-perchlorate and about 12-16% of aluminium powder as fuel. The boosters of the Space Shuttle, the Ariane 5 and many upper stage engines use this type of propellant. Typical polybutadiene used currently is hydroxyl terminated polybutadiene (HTPB), in older designs use was often made of carboxyl terminated polybutadiene (CTPB) or polybutadiene acrylonitrile (PBAN). HTPB based propellants have better mechanical properties and processing compared to propellants based on CTPB or PBAN. More advantages of HTPB propellants are that a wide range of burn rates can be achieved, they

have good storage stability, stable combustion and they have better solids loading % and performance than CTPB and PBAN [45].
A third class are the Composite Modified Double Base (CMDB) propellants. These propellants are in between the other two classes.

In the MDO, TPH-3340 will be used as propellant for the upper stage, as it has been used in upper stages in reality and the burn characteristics were found in literature. TPH-3340 is a HTPB-AP-Al propellant used in several STAR-series solid rocket motors [46]. The propellant is composed of 11% HTPB, 71% ammonium-perchlorate and 18% of aluminium powder. Burn parameters of this propellant were found based on the regression rate of the STAR 48B [47]. In correspondence with the constants in Equation 3.3, the burn rate exponent n is 0.3, which falls in the range of HTPB propellants [45, 48]. It is given that the regression rate is 0.228 inches per second for a chamber pressure of 1000 psia. Switching to SI units gives a burning rate coefficient a of $1.626 \cdot 10^{-3}$. Typically, the values for the burn rate exponent for solid propellants are only valid over a certain range of pressures. At a characteristic pressure value a "slope break" will occur where the burn rate changes to a higher value. In AP-propellants, the slope break generally is observed around 140 bar [48].
To analyze the propellant performance the tool CEA (Chemical Equilibrium with Applications) developed by NASA is used. CEA is software that "calculates chemical equilibrium product concentrations from any set of reactants and determines thermodynamic and transport properties for the product mixture. Applications include calculation of theoretical rocket performance and combustion properties" [49]. To calculate the performance, the composition of the propellant is input in CEA. Aluminium and ammonium-perchlorate are available from the CEA database, but HTPB is not. Therefore, HTPB is input manually with a heat of decomposition of -52.58 kJ/mol and a chemical formula of C 10, H 15.09, O 0.23, N 0.10 [50]. CEA outputs the chamber temperature, molar mass and specific heat ratio of the propellant for a range of chamber pressures. From the densities of the compositions given in [50], it is estimated that TPH-3340 has a density (ρ_p) of 1820 kg/m^3. This value falls in the range of reported densities for HTPB-AP-Al propellants [45]. The CEA output for the propellant is given in Appendix A.

3.2.3. Design of Upper Stage Solid Rocket Motor

To reach orbit, an extra upper stage must be added to the nominal three stages of the SM-3. To design this stage, design variables must be established with which all relevant performance parameters can be determined. In this thesis, it will not include a detailed optimization of the grain configuration . The model only includes constant thrust configurations. It is chosen to use an end-burning grain configuration for the upper stage motor, because the burn surface is relatively small and remains roughly constant during the burn. A small burn surface results in a smaller thrust force, which in this thesis is important to limit the axial acceleration as the payload mass is unusually small. The axial acceleration constraint will be discussed in more detail in the Trajectory chapter. In this section the design variables and input parameters are given and the method to calculate the performance is shown. It also includes the mass estimations of the motor.
Five design variables are determined, which are the following:

- Length of cylindrical motor case section (L_c): In this part the thermal protection layer decreases linearly from the the nozzle side to the top side. As the grain regresses, a larger area of the case will be exposed to the hot flow in the chamber. The case at nozzle side will have the longest exposure and therefore the biggest thermal protection thickness.

- Maximum radius of the grain (R_g): As the thermal protection thickness decreases towards the case top, the grain radius increases until it reaches a maximum at the end of the cylindrical section.
- Length of the elliptical case top (L_e): The case top is modelled elliptical as a trade-off between propellant mass capacity and wall thickness. Because of the length restriction, the case with a flat top could hold the most propellant, but this is also relatively heavy [5]. A spherical top is light, but limits the propellant volume. Therefore, the length of the top is left as a design variable and the propellant volume and case top mass can be optimized.
- Chamber pressure (p_c): The chamber pressure is constant during the burn.
- Exit pressure (p_e): The exit pressure is also constant during the burn.

Firstly, with the chamber pressure, the corresponding values for the chamber temperature (T_c), molar mass (M) and specific heat ratio (γ) are read from a file that is generated with CEA. Then with the Vandenkerckhove function, which is defined as:

$$\Gamma = \sqrt{\gamma} \cdot \left(\frac{2}{\gamma+1}\right)^{\left(\frac{\gamma+1}{2(\gamma-1)}\right)} \tag{3.4}$$

and the pressure ratio, the expansion ratio can be determined:

$$\varepsilon = \frac{A_\mathrm{e}}{A_\mathrm{t}} = \frac{\Gamma}{\sqrt{\frac{2\gamma}{\gamma-1} \cdot \left(\frac{p_\mathrm{e}}{p_\mathrm{c}}\right)^{\left(\frac{2}{\gamma}\right)} \left(1 - \left(\frac{p_\mathrm{e}}{p_\mathrm{c}}\right)^{\left(\frac{\gamma-1}{\gamma}\right)}\right)}} \tag{3.5}$$

The mass flow is constant and determined by the mass flow from the grain given by Equation 3.2 and Equation 3.3. In Equation 3.2 the burn surface S is determined with:

$$S = \pi R_\mathrm{g}^2 \tag{3.6}$$

This mass flow is equal to the critical mass flow through the throat:

$$\dot{m}_\mathrm{cr} = \frac{\Gamma \cdot p_\mathrm{c} \cdot A_\mathrm{t}}{\sqrt{R \cdot T_\mathrm{c}}} \tag{3.7}$$

in which R is the specific gas constant. The specific gas constant is obtained with the universal gas constant R^* (8,314 kJ/mol) and the molar mass:

$$R = \frac{R^*}{M} \tag{3.8}$$

Using Equation 3.2 and Equation 3.7, the throat area can be determined:

$$A_\mathrm{t} = \frac{\dot{m}\sqrt{R \cdot T_\mathrm{c}}}{\Gamma \cdot p_\mathrm{c}} \tag{3.9}$$

Then with the expansion ratio, also the nozzle exit area can be obtained:

$$A_\mathrm{e} = A_\mathrm{t} \cdot \varepsilon \tag{3.10}$$

Then two characteristic parameters can be defined: the thrust coefficient (C_F) and the characteristic velocity (c^*). These parameters make it possible to determine the effect of the gas expansion in the nozzle and the energetic content of the expellant on the specific impulse separately[5]. The thrust coefficient determines the enlargement of the thrust caused by gas expansion in the nozzle as relative to the thrust that would occur if no chamber flow was present and if the chamber pressure only acted over the throat area. The thrust coefficient is defined as:

$$C_\mathrm{F} = \frac{T}{p_\mathrm{c} \cdot A_\mathrm{t}} \tag{3.11}$$

After rewriting, it can be calculated with previously obtained parameters:

$$C_\mathrm{F} = \Gamma \sqrt{\frac{2\gamma}{\gamma - 1}\left(1 - \left(\frac{p_\mathrm{e}}{p_\mathrm{c}}\right)^{\left(\frac{\gamma-1}{\gamma}\right)}\right)} \tag{3.12}$$

The characteristic velocity is given by:

$$c^* = \frac{1}{\Gamma}\sqrt{R \cdot T_\mathrm{c}} \tag{3.13}$$

The parameters used in the definition of the characteristic velocity show that it is a property that displays the internal energy of the propellant that is available for propulsion. Together, the characteristic velocity and the thrust coefficient give the true exhaust velocity:

$$U_\mathrm{e} = C_\mathrm{F} \cdot c^* \tag{3.14}$$

Then all parameters have been determined to fill in Equation 3.1 and calculate the ideal vacuum thrust. To obtain the real vacuum thrust, the ideal vacuum thrust is multiplied with a correction factor. The value of this correction factor will be determined in section 3.3, where this method is validated with data from real solid rocket motors. Lastly, the specific impulse is determined with the equivalent exhaust velocity and the gravitational acceleration:

$$I_\mathrm{sp} = \frac{U_\mathrm{eq}}{g_0} \tag{3.15}$$

where the equivalent exhaust velocity is defined as:

$$U_\mathrm{eq} = \frac{T_\mathrm{vac}}{\dot{m}} \tag{3.16}$$

3.2.4. Mass Estimation and Sizing

When the design variables are generated and the performance of the propulsion module is determined, it is necessary to determine the mass of the propulsion system for the dynamic simulation. The size is also necessary to determine the total launch vehicle geometry. The mass and size are determined for the individual components of the rocket motor. The motor case will have a cylindrical mid-section with elliptical tops on both sides. The nozzle will be a (slightly) submerged nozzle like most nozzles of found solid stages have, including the STAR series [46, 51].

Thermal Protection System and Propellant

The high temperature of the gaseous flow in the chamber causes the motor case material to heat up. This heating up of the material can lead to a reduction of the strength of the case structure. It is therefore important to implement a layer of thermal protection system (TPS) materials to avoid the case wall heating up to high temperatures. The TPS mass is often a considerable part of a solid rocket motor total inert mass. Especially for the chosen end-burning configuration the TPS mass will be important, as a larger part of the inner case wall will be exposed to the chamber flow for a longer amount of time than for internal-burning grains. A simplified method is used here to determine the TPS layer thickness using a material used in many of the STAR-series motors [46]. This material is silica-filled EPDM rubber which has ablative and insulation properties. With this method, the thickness will be determined based on the ablative properties only.
To determine the convective heat flux to the wall, the following equation is used [5]:

$$q_\alpha = h_\alpha (T_\mathrm{c} - T_\mathrm{w}) \tag{3.17}$$

T_c is the chamber temperature, T_w is the temperature of the ablative material, which is equal to the decomposition temperature of EPDM at 683 K [52]. h_α is determined using the Stanton number, which is defined as the ratio between the convective heat transfer and the heat contained in the flow:

$$h_\alpha = \rho v c_p \cdot \mathrm{St} \tag{3.18}$$

In which ρ is the density of the gaseous flow, v is the flow velocity and c_p is the specific heat at constant pressure. The Stanton number is determined by the Modified Reynolds Analogy, for internal flows [5]:

$$\mathrm{St} = \frac{f_F}{2} \mathrm{Pr}^{-2/3} \tag{3.19}$$

Using the modified Reynolds Analogy can lead to errors of up to 40% in the Stanton number [5]. The effect of this will be investigated in section 7.5. Pr is the Prandtl number, which is approximated with:

$$\mathrm{Pr} = \frac{4\gamma}{9\gamma - 5} \tag{3.20}$$

and f_F is the Fanning friction factor, which is 4 times smaller than the Darcy-Weisbach friction factor and therefore determined with [5]:

$$f_F = \frac{0.0032 + 0.221 \cdot \left(\frac{1}{\mathrm{Re}_\mathrm{D}}\right)^{0.237}}{4} \tag{3.21}$$

This equation is valid for a large range of Reynolds numbers ($3 \cdot 10^3$ to 10^7), which will include the values occurring in the MDO. The value for the dynamic viscosity, which is necessary to determine the Reynolds number is obtained from a relation with the chamber temperature and the molar mass of the gas [53]:

$$\mu = 8.7 \cdot 10^{-8} \cdot \sqrt{M} \cdot T_\mathrm{c}^{0.65} \tag{3.22}$$

The mass release from the ablative layer has an effect on the skin friction coefficient. Using the Spalding number (B), this effect can be determined. The friction factor (and therefore also the convective heat transfer coefficient) is scaled with a factor u:

$$u = 1,2 \cdot \ln \frac{(1 + B)}{B} \tag{3.23}$$

with the Spalding number defined as the ratio between the enthalpy difference Δh_T between the hot gases and the wall and the enthalpy needed for the gasification h_v [5]:

$$B = \frac{\Delta h_T}{h_v} \tag{3.24}$$

Specific heat of silica-filled EPDM rubber is assumed to be constant with temperature and taken as 1900 J/kgK and enthalpy needed for gasification is equal to the heat of decomposition and taken as 468 kJ/kg [54]. The regression rate of the ablative material is determined with:

$$r_\mathrm{TPS} = \frac{h_\alpha \cdot (T_\mathrm{c} - T_\mathrm{w})}{h_\mathrm{v} \cdot \rho_\mathrm{TPS}} \tag{3.25}$$

Where the density of the material ρ_TPS is estimated at 1100 kg/m^3, which is an average value of the values that are found in literature (around 1040 - 1200 kg/m^3) [54, 55]. The regression rate is considered constant during the burn at all exposed locations on the case wall.

The TPS thickness of the elliptical case top will be constant over the whole surface and is based on the burn time in the case top. This will therefore be a slight overestimation of the necessary TPS mass. The burn time in the elliptical case top is obtained from the propellant mass in the case top and the mass flow:

$$t_\mathrm{b,t} = \frac{\frac{2}{3}\pi (R_\mathrm{g})^2 L_\mathrm{e} \cdot \rho_\mathrm{p}}{\dot{m}} \tag{3.26}$$

The thickness then becomes:

$$t_\mathrm{TPS,t} = r \cdot t_\mathrm{b,t} \tag{3.27}$$

This thickness is applied uniformly over the surface of the case top. Therefore, the surface of the elliptical top is needed. First a parameter e is introduced:

$$e = \sqrt{1 - \left(\frac{L_\mathrm{e}}{R_\mathrm{g}}\right)^2} \tag{3.28}$$

Then the surface is obtained with the formula for the surface of an oblate spheroid. The case top is only half an oblate spheroid and therefore it is multiplied by 1/2:

$$S_\mathrm{e} = 2\pi R_\mathrm{g}^2 \left(1 + \frac{L_\mathrm{e}^2}{e R_\mathrm{g}^2} \cdot \mathrm{arctanh}(e)\right) \cdot \frac{1}{2} \tag{3.29}$$

The TPS mass in the elliptical top then becomes:

$$M_\mathrm{TPS,t} = t_\mathrm{TPS,t} \cdot S_\mathrm{e} \cdot \rho_\mathrm{TPS} \tag{3.30}$$

The TPS thickness at the nozzle side of the cylindrical part of the case is determined with the thickness at the top part and the burn time of the propellant in the cylindrical section multiplied by the TPS regression rate. The propellant in the cylindrical section in this equation is assumed to be the total cylindrical volume, in reality a small volume will be taken by the TPS material near the wall. Therefore, this will be a slight overestimation of the total TPS thickness and mass. The thickness near the nozzle is given by:

$$t_\mathrm{TPS,n} = t_\mathrm{TPS,t} + r_\mathrm{TPS} \cdot \frac{\pi R_\mathrm{g}^2 L_\mathrm{c} \cdot \rho_\mathrm{p}}{\dot{m}} \tag{3.31}$$

Also the elliptical section that connects the nozzle to the cylindrical section will have this TPS thickness on the inner wall, as it is exposed to the flow during the entire burn. When the thicknesses are known, the real propellant mass in the cylindrical section can be determined. The thickness decreases linearly from the nozzle to the top and thus can the volume be determined using the relations for a cone frustum. The volume of a cone frustum is:

$$V_\mathrm{f} = \frac{\pi h}{3}\left(R^2 + Rr + r^2\right) \tag{3.32}$$

In which R is the radius of the larger base, which in this case equals R_g, r is equal to $R_\mathrm{g} - t_\mathrm{TPS,n}$ and h is L_c. The propellant volume in the cylindrical part is calculated with:

$$V_\mathrm{p,cyl} = \frac{\pi L_\mathrm{c}}{3}\left(R_\mathrm{g}^2 + R_\mathrm{g}(R_\mathrm{g} - (t_\mathrm{TPS,n} - t_\mathrm{TPS,t})) + (R_\mathrm{g} - (t_\mathrm{TPS,n} - t_\mathrm{TPS,t}))^2\right) \tag{3.33}$$

The propellant in the cylindrical top is determined with the formula for the volume of an oblate spheroid, multiplied by 1/2:

$$V_\mathrm{p,t} = \frac{4}{3}\pi R_\mathrm{g}^2 L_\mathrm{e} \cdot \frac{1}{2} \tag{3.34}$$

Adding the propellant from the cylindrical section and the elliptical top, the total propellant mass is obtained:

$$M_\mathrm{p} = (V_\mathrm{p,t} + V_\mathrm{p,cyl}) \cdot \rho_\mathrm{p} \tag{3.35}$$

A volumetric loading fraction of 1 is used in the MDO, which is common for end-burning grains [5]. A small part of the propellant will be left as sliver after the burn. Modern rocket motors usually have slivers below 1% of propellant mass [23, 45], but here 1% is used. To model this, 1% is taken from the propellant mass and added to the inert mass. The mass of the TPS material in the cylindrical section is determined by subtracting the propellant volume from the total cylinder volume and multiplying with the TPS density:

$$M_\mathrm{TPS,cyl} = (\pi \cdot (R_\mathrm{g} + t_\mathrm{TPS,t})^2 L_\mathrm{c} - V_\mathrm{p,cyl}) \cdot \rho_\mathrm{TPS} \tag{3.36}$$

During the burn the ablative material regresses and mass reduces. The exposed area of the ablative material increases with the burn time and hence also the mass release of the ablator. At the start of the burn only the elliptical top at the nozzle side ($S_\mathrm{e,n}$) is exposed and at the end the entire inner case surface (S_c) is exposed. $S_\mathrm{e,n}$ is also determined with Equation 3.28 and Equation 3.29 with the difference that a small area is subtracted through which the nozzle protrudes. The mass regression from the ablator at any time during the burn is then given by:

$$\dot{m}_\mathrm{TPS} = r_\mathrm{TPS} \cdot \left(S_\mathrm{e,n} + (S_\mathrm{c} - S_\mathrm{e,n}) \cdot \frac{t}{t_\mathrm{b}}\right) \tag{3.37}$$

Testing has shown that this method works well. The results of this test can be seen in Appendix D in Figure D.3. Around 5-7% of insulator mass is left at the end of the burn, which is deemed acceptable as the TPS mass was slightly overestimated.

Motor Case

The motor case functions as a pressure vessel. It contains the propellant and TPS material and must be able to withstand the maximum operating pressure (MEOP) occuring during the burn. In this case with constant pressure, the MEOP is equal to p_c. A safety factor f is included to decrease the probability of failure. The safety factor is a combination of a design burst pressure safety factor and a design safety factor [5]. The value for the safety factor will be determined in section 3.3. For the cylindrical section the wall thickness is then calculated with [5]:

$$t_{\text{cyl}} = \frac{p_c \cdot R_c}{\sigma} \cdot f \tag{3.38}$$

R_c is the case radius, which comes from:

$$R_c = R_g + t_{\text{TPS,t}} \tag{3.39}$$

The case material is Titanium (Ti6Al-4V), which is often used in upper stage motors [46]. σ is taken from its yield strength, which is 1100 N/mm^2 and it has a density of 4428 kg/m^3. The wall thickness in the elliptical sections are obtained differently:

$$t_e = \frac{p_c \cdot R_c \cdot K}{\sigma} \cdot f \tag{3.40}$$

in which K is a factor that takes into account the radius to length ratio:

$$K = \frac{1}{6}\left(2 + \left(\frac{R_c}{(L_e + t_{\text{TPS,t}})}\right)^2\right) \tag{3.41}$$

The masses are then calculated by multiplying the thicknesses with the surface area of the corresponding sections and the density of the case material. The surface area for the cylindrical section is:

$$S_{\text{cyl}} = 2\pi R_c \cdot L\text{c} \tag{3.42}$$

The length of the elliptical section at the nozzle side only affects the inert mass of the motor as it is modelled here. Therefore, it is set constant at 0.1 m. This is not an optimized value, but a reasonable estimate for the range of radii that can occur during optimization. A circular section is subtracted from the surface of the elliptical part at the nozzle side. The size of this circular section corresponds with the radius that a conical nozzle would have at that location.

Nozzle and Igniter

Multiple methods have been encountered to determine the nozzle mass. It is encountered to be determined with the surface area of the nozzle and a kind of density based on the expansion ratio [23]. Also regression data has been used to relate the nozzle mass to the vacuum thrust [14]. However, scale of the nozzles in this research is much smaller than the methods can accurately handle. Therefore, a new regression analysis is performed with smaller nozzles from the STAR series motors. Most STAR motors have a slightly submerged nozzle with a carbon-carbon throat and a carbon-phenolic exit cone. Usually, the nozzle mass given for these motors includes the igniter mass, excluding igniter propellant. The motor will feature thrust vector control (TVC), but because very little data points are available on motors of this scale featuring TVC, the nozzle mass is first estimated without TVC and then a factor is applied to account for TVC system mass. The results of the regression data is shown in Figure 3.5. The motors used from the STAR series are shown in Appendix B. The nozzle mass is linearly related to the average vacuum thrust:

$$M_n = 0.5814 \cdot T_{\text{vac}} \tag{3.43}$$

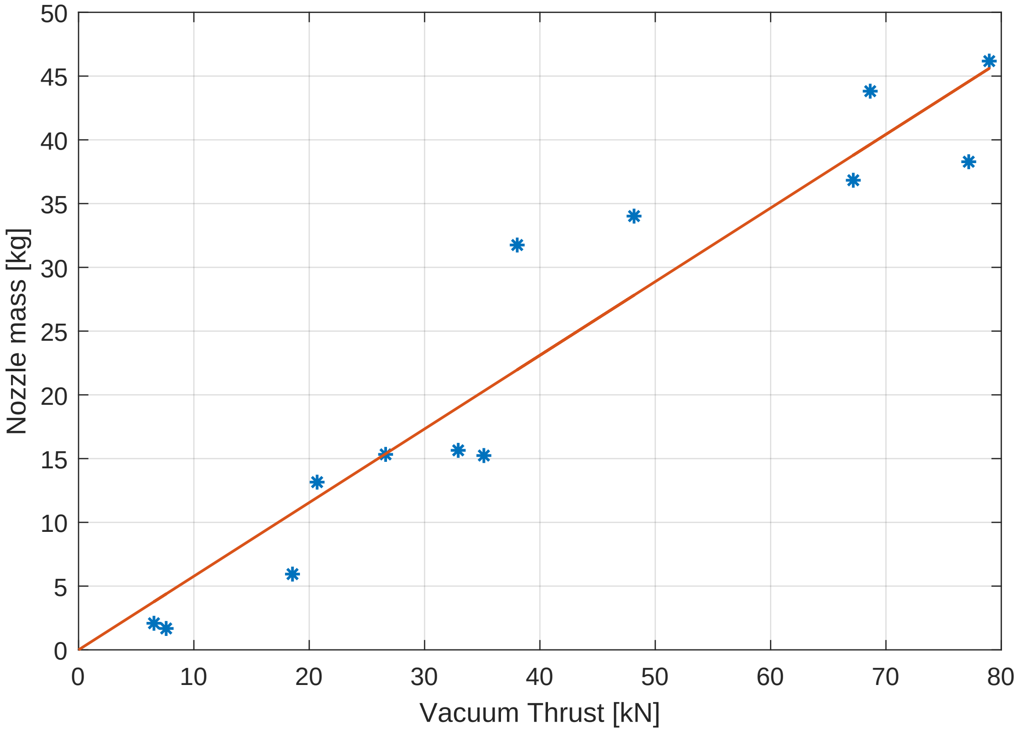

Figure 3.5: Regression analysis of the nozzle masses of STAR series motors

The vacuum thrust occurring in this research will be on the left end, being under 10 kN. In this area, the nozzle mass of the only data point is overestimated by 45%. The absolute mean error is 17.7%. This is deemed acceptable, as the error will have a limited effect on increasing the total inert mass for small vacuum thrusts. To include TVC, the nozzle mass must be multiplied by a correction factor. In earlier studies it was found that for engines with vacuum thrust below 200 kN, adding TVC almost doubles the total nozzle mass [14]. However, filling in the corresponding relation for 10 kN, yields in an increase from TVC of around 36%. Also, evaluating the STAR 48B (Long Nozzle) and the STAR 48BV (which have the exact same parameters, but the only difference is a ± 4 degree movable nozzle), it can be found that the TVC adds only 20% of mass to the nozzle assembly. The TVC factor will therefore be taken in the middle of the three methods, at 50% mass increase (multiplying by 1.5).

The igniter mass is often around 1 - 2% of the total inert mass [23]. The igniter hardware is already included with the nozzle estimation, but the igniter propellant is estimated at 2% of the inert mass.

Looking at cross-sections from many solid rocket motors upper stages, it can be seen that the convergent length of the nozzle is very small [45, 51]. From the STAR30C, STAR30E and STAR37FM, it can be determined that the opening of the convergent section has a radius of approximately 1.6 - 1.8 times the throat radius and a convergent half angle (β_{con}) of approximately 30 degrees [51]. The nozzle convergent length is calculated with:

$$L_{\text{con}} = \frac{(R_{\text{t}} \cdot 1.8) - R_{\text{t}}}{\tan \beta_{\text{con}}} \tag{3.44}$$

The nozzle divergent half angle (β_{div}) usually falls in the range of 12-18 degrees. The nozzle is modeled as a bell nozzle. A bell nozzle has a length of 80% of the length of a comparable conical nozzle with the same area ratio and a nozzle divergent half angle of 15 degrees [45]. Therefore, a bell nozzle factor of 0.8 will be multiplied to the length of a conical nozzle with a 15 degree divergent half angle to model the nozzle length. The conical nozzle has a circular part after the throat until it reaches the divergence of the divergent half angle. The nozzle divergent length is determined with [5]:

$$L_{\text{div}} = 0.8 \cdot \left(R_{\text{u}} \sin \beta_{\text{div}} + \frac{R_{\text{e}} - R_{\text{t}} - (R_{\text{u}} - R_{\text{u}} \cos \beta_{\text{div}})}{\tan \beta_{\text{div}}} \right) \tag{3.45}$$

Here, R_{u} is the longitudinal radius of the throat which is defined as [5]:

$$R_{\text{u}} = 0.382 \cdot R_{\text{t}} \tag{3.46}$$

The exit radius R_{e} can be determined from the exit area A_{e}. The exit radius has the constraint that it cannot be larger than the radius of the case. The model does not include throat erosion and therefore the throat radius will be constant.

A schematic drawing is made of the cross-section of the SRM model used for the upper stage. It can be seen in Figure 3.6.

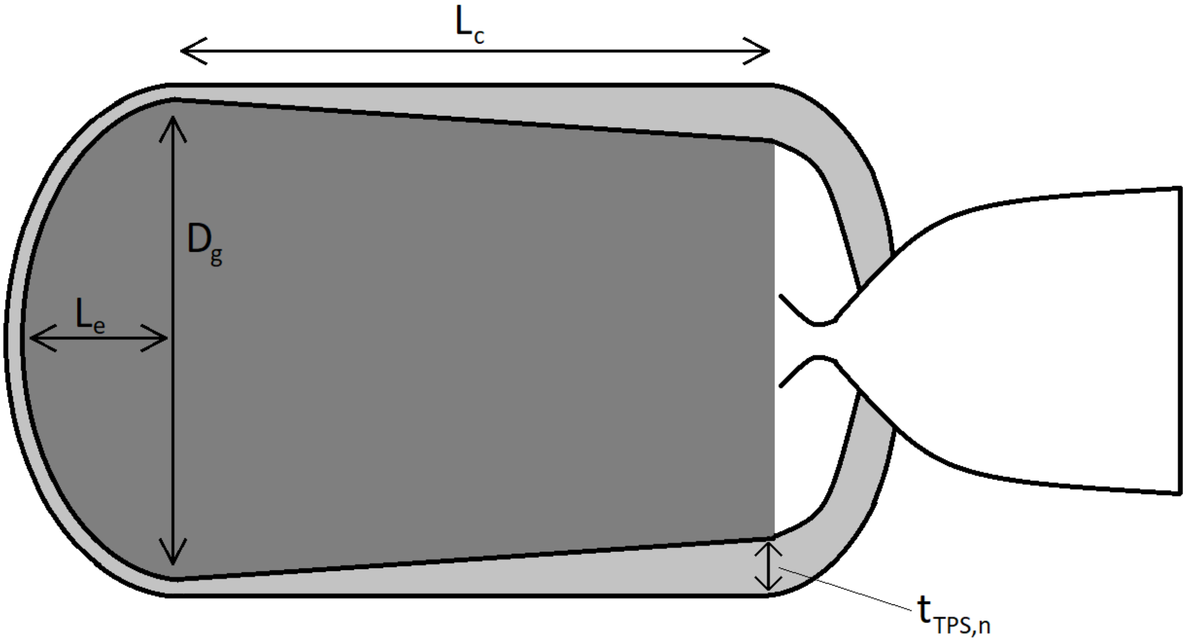

Figure 3.6: Schematic drawing of the cross-section of the SRM model (Not to scale)

3.3. Validation of Propulsion Model

A validation must be performed to evaluate how accurately the model represent reality. For this a database is created with 14 solid rocket motors with similar characteristics as the motors in the MDO. The motors all use TPH-3340 as propellant and the motors with Titanium as case material are used to validate the case mass.

First of all, the main performance parameters of the propulsion system are validated, the thrust and the effective specific impulse. It can be expected that using the ideal rocket equations from earlier sections the performance will be overestimated, as no correction factors for real losses have been implemented. The database only gives the initial throat diameter, which does not correspond with the average and maximum thrust and pressures that are given. Therefore it was necessary to read the data from the thrust- and pressure profiles over the burn time to obtain values that correspond with each other. The thrust and pressures are taken at the earliest in the burn where a relatively steady state occurs, because there the throat diameter is closest to the initial throat diameter. The results of the validation are shown in Figure 3.7 and Figure 3.8.

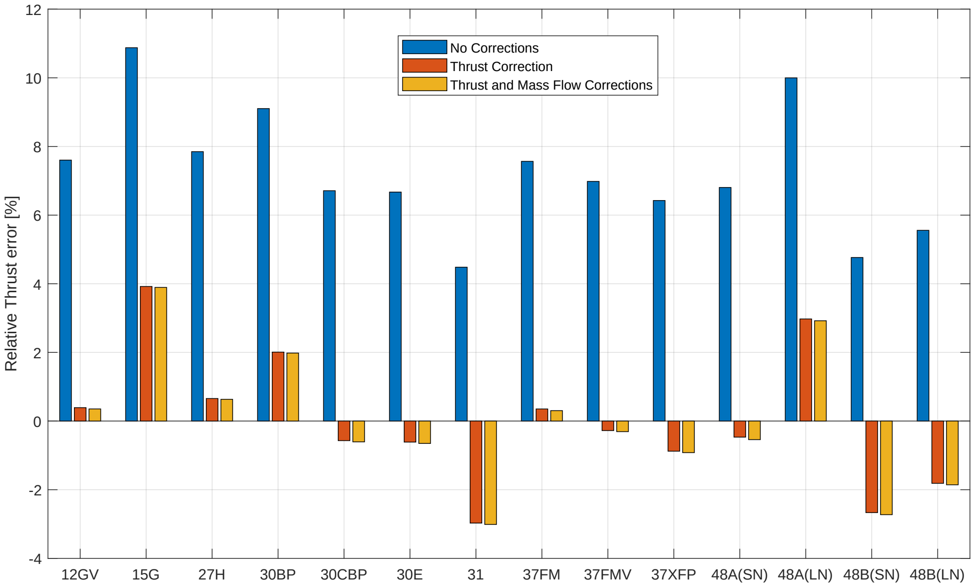

Figure 3.7: Validation of vacuum thrust for certain STAR motors

It can be seen that over the whole range of motors, the thrust and specific impulse are largely overestimated as expected. A solution that was considered, was to correct the thrust so that the average error would become 0. For that, the vacuum thrust was multiplied with a factor of 0.9276. However, in Figure 3.8 it can be seen that the specific impulse is then still overestimated for all motors. So then, to also account for throat erosion, a correction factor of 1.038 was applied to the mass flow and 0.895 to the vacuum thrust. It can be seen that this barely affects the thrust estimations, but does improve the estimation of the specific impulse. The correction factor is not to compensate for a miscalculation in mass flow, but for a small increase in throat area by throat erosion. Therefore, in the real model, where the throat area is constant, no correction on the mass flow is applied, but the correction factor

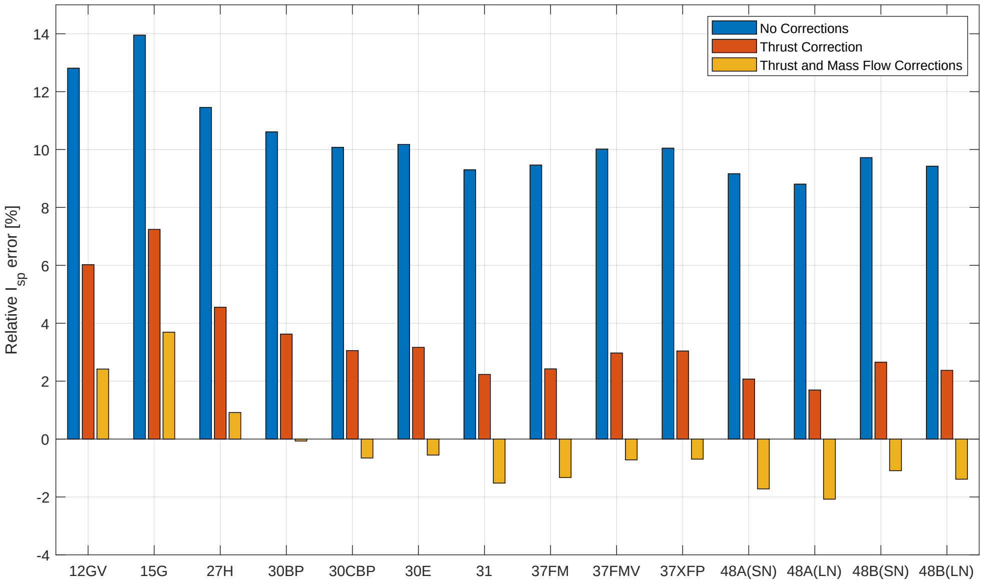

Figure 3.8: Validation of effective specific impulse for certain STAR motors

for the thrust is still 0.895.

The validation of the inert mass is less straightforward. The end-burning configuration used in the MDO is very different from the internal-burning configuration from the STAR motors. That means that especially the TPS mass will differ, as not as much of the inner wall is exposed for an internal-burning grain. This makes it difficult to validate. The main contributors of the total inert mass are the nozzle, case mass and TPS mass. The nozzle has been determined with regression data, which is thus already linked with real data and the TPS mass will be difficult to validate due to differences in configuration. It is therefore chosen to only validate the motor case mass. To validate the motor case mass, from the Northrop Grumman Propulsion Products Catalog, the diameters and total lengths of the motors are given [46]. The cases are often spherical or cylindrical with spherical tops. The length of the cylindrical section can be estimated from the images in the Catalog. Using the case mass equations from previous section, the case masses are determined. Only motors with a Titanium case are considered and the safety factor is taken as 2. The results for the different STAR motors are shown in Figure 3.9. It can be seen that the motor case mass for half the motors is underestimated and the other half is overestimated. The biggest error occurs with the STAR13B, which is the smallest motor with a reported case mass of only 2.54 kg. In reality, the motor also features a metal ring near the top of the case. This could explain the underestimation, as such masses are not taken into account and for such a small motor case even small masses can cause a large relative error. The mean error is 0.04% and no clear trend is observed. It is therefore chosen not to apply a correction factor on the case mass. Consequently, in the MDO a safety factor of 2 will be used.

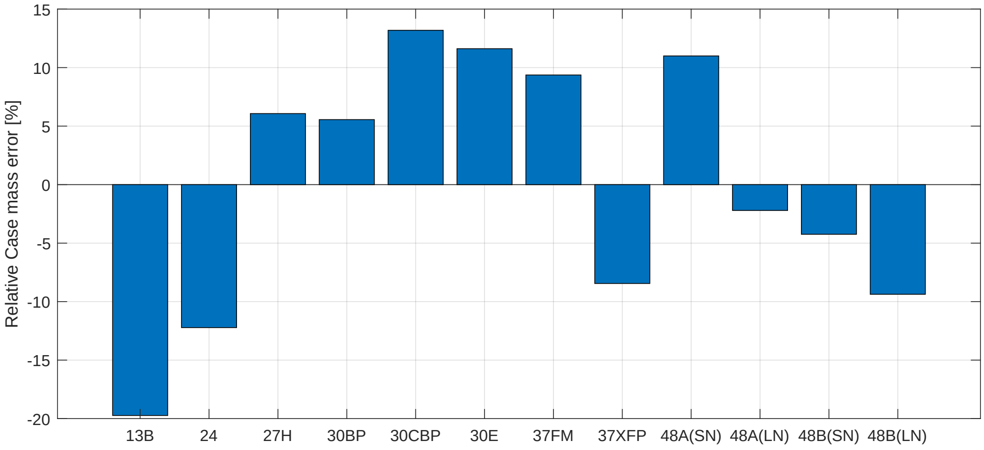

Figure 3.9: Validation of motor case mass for certain STAR motors

4

Launch Vehicle Model

In this chapter the launch vehicle modeling will be discussed. With the propulsion system modeled, the complete geometry of the vehicle can be determined. The geometry influences the aerodynamic forces acting on the vehicle, which are important when evaluating the dynamics. First, the modeling of payload fairing, payload adapter and avionics is discussed. Then, it is shown how the aerodynamic coefficients are determined. Lastly, it is discussed how the SM-3 Block IIA is modeled as accurately as possible.

4.1. Payload Fairing

The function of the payload fairing is to protect the payload from the incoming flow and, ideally, give the vehicle an aerodynamically shaped geometry. Many different nose cone shapes can be used. Choosing the optimal shape is a difficult task. Aerodynamically, the shapes differ in performance for different Mach numbers and there is no clear winner in this department [56, 57]. Moreover, shapes that do not particularly excel aerodynamically, can perform well structurally [58]. Additionally, performance may also change for different fineness ratios. It is therefore considered too time-consuming to do a detailed trade-off between nose cone shapes, especially since the effect of the exact shape on the total system performance is limited [23].

Therefore, the top of the fairing in the MDO will be modeled with a tangent ogive shape, which is the default in the software Missile DATCOM and has been used in MDOs before [14, 26]. Below the ogive shape, a cylindrical section with the length of the elliptical top length of the upper stage motor case will connect the fairing to the upper stage motor. The length of the tangent ogive nose cone L_{og} and the length of the cylindrical section $L_{\mathrm{f,cyl}}$ added together give the total fairing length L_{f}. A visual representation of the shape of a tangent ogive is given in Figure 4.1. The grey area is a two-dimensional cross section of half the nose cone, where the line with length L is the axis of symmetry. The payload fairings generated in the MDO will be very small compared to ones encountered on 'normal' sized launch vehicles. General fairing mass estimations relationships therefore do not cover such small fairing sizes [59]. It is therefore chosen to estimate the payload fairing mass by scaling it down from another relatively small launch vehicle, Electron. Electron has a fairing with a length of 2.5 meter and a diameter of 1.2 meter with a mass of 44 kg. The fairing mass will

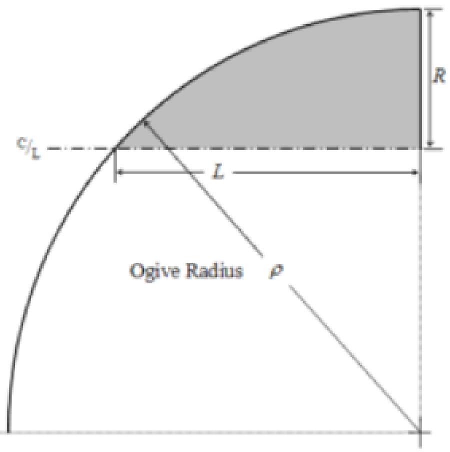

Figure 4.1: Tangent ogive nose cone geometry [6]

be calculated with the length and diameter of the fairing, L_f and D_f:

$$M_\mathrm{f} = 44 \cdot \frac{L_\mathrm{f}}{2.5} \cdot \left(\frac{D_\mathrm{f}}{1.2}\right)^2 \tag{4.1}$$

Of course, the payload fairing must comprise enough space to house the payload. The exact dimensions of the payload are not known. It is therefore chosen to constrain the minimum fairing volume with a set volumetric density of the payload. The volumetric density is based on the density of a cubesat. A 1-unit (1U) cubesat has dimension of 10x10x10 centimeters. It generally has a mass between 1 and 1.33 kg [60], and thus a density of 1000 to 1330 kg/m^3. The contours of the payload fairing will not follow the payload perfectly and therefore the required volume is multiplied by a factor of 1.5:

$$V_\mathrm{f,req} = \frac{M_\mathrm{pl}}{1330} \cdot 1.5 \tag{4.2}$$

The factor of 1.5 is a rough estimate and the effect of a larger or smaller value will be investigated in a sensitivity analysis. The payload mass M_pl is a design variable. To calculate the available volume under the tangent ogive nose cone, an extensive formula is used:

$$\begin{aligned} V_\mathrm{f} = \pi \cdot \Bigg(& -(L_\mathrm{og} \cdot \rho_\mathrm{og} - L_\mathrm{og} \cdot R_\mathrm{og}) \cdot \sqrt{\rho_\mathrm{og}^2 - L_\mathrm{og}^2} \\ & - \arcsin\left(\frac{L_\mathrm{og}}{\rho_\mathrm{og}}\right) \cdot \rho_\mathrm{og}^3 \\ & + \frac{6 \cdot L_\mathrm{og} \cdot \rho_\mathrm{og}^2 - 6 \cdot L_\mathrm{og} \cdot R_\mathrm{og} \cdot \rho_\mathrm{og} + 3 \cdot L_\mathrm{og} \cdot R_\mathrm{og}^2 - L_\mathrm{og}^3}{3} \\ & + R_\mathrm{og} \cdot \arcsin\left(\frac{L_\mathrm{og}}{\rho_\mathrm{og}}\right) \cdot \rho_\mathrm{og}^2 \Bigg) \end{aligned} \tag{4.3}$$

Here, R_og is the radius at the base of the tangent ogive nose cone, which equals the diameter of the motor case. ρ_og is defined as:

$$\rho_\mathrm{og} = \frac{L_\mathrm{og}^2 + R_\mathrm{og}^2}{2 \cdot R_\mathrm{og}} \tag{4.4}$$

The derivation and verification of Equation 4.3 is shown in Appendix C.

4.2. Payload Adapter and Avionics

The payload adapter and avionics both contribute to the total inert mass of the upper stage. Estimating their masses is quite difficult. No data can be found on masses of such systems of the sizes occurring in the MDO. Different types adapters exist, but their masses can range from 0.35 to 2 kg [61–63]. It is also imaginable that for the unusual dimensions of the fairings in the MDO, a dedicated adapter for this system must be developed for optimal performance. It is therefore chosen to not model the payload adapter mass separately, but to include it in the payload mass.

The same is done for the avionics mass. The trend of smaller and lighter electronics being implemented in small satellites can also occur in the launch vehicle market, enabling very significant potential for nano-launch vehicles [64]. The exact masses of the avionics subsystems is, unfortunately, not easily estimated. So, the determined maximum payload mass will also include the avionics mass of the upper stage.

4.3. Aerodynamics

When the shape of the launch vehicle is determined, the aerodynamic coefficients can be determined. The aerodynamic coefficients are necessary to calculate the magnitude of the aerodynamic forces acting on the vehicle in the atmosphere. The main forces are the lift and drag forces. The equations for lift and drag are:

$$L = C_{\mathrm{L}}\frac{1}{2}\rho V^2 S \tag{4.5}$$

$$D = C_{\mathrm{D}}\frac{1}{2}\rho V^2 S \tag{4.6}$$

In these equations, ρ is the atmospheric density, S is the aerodynamic reference area and C_{L} and C_{D} are the lift and drag coefficient, respectively. For launch vehicles and missiles it is common practice to take the frontal cross-sectional area as the aerodynamic reference area. To determine the aerodynamic coefficients, the software Missile DATCOM is used. Missile DATCOM is a semi-empirical aerodynamic prediction code developed by the US Air Force that calculates aerodynamic coefficients as a function of angle of attack and Mach number for a variety of axisymmetric and non-axisymmetric missile geometries [65]. Older versions were subjected to International Traffic in Arms Regulations (ITAR), but the 1997 version has been publicly available. It has been used in many studies before [14, 23, 26, 27, 66–68]. Missile DATCOM can generate the coefficients of a vehicle for 20 different angles of attack and Mach numbers [65]. The geometry of the launch vehicle is input in an input file and for each set of angle of attack and Mach number, the aerodynamic coefficients are determined. By means of bi-linear interpolation the coefficients can be determined during simulation for every angle of attack and Mach number. The range in Mach number is 0.3 to 5.0 and angles of attack range from -30 to 30 degrees. If during simulation a parameter exceeds its boundaries, the boundary values are taken. There is a possibility to implement the Missile DATCOM code directly in the MDO. However, that creates an enormous computational load. It is therefore chosen to create a database of geometries and during each simulation choose the values from the database that the vehicle in the MDO has closest resemblance with. The parameters influencing the vehicle shape are the length of the ogive nose cone and the diameter of the upper stage. The coefficients have been determined for each set of these parameters over the whole range of possible values they can

become, with steps of 0.005 m in both the diameter and the nose cone length. Differences between using the direct code and a database have been shown to be very small [69].
The software does have its limitations. It has been observed to have problems with calculating the axial force coefficient in the transonic regime [67, 68]. Also, beyond angles of attack of 30 (or -30) degrees the coefficients are calculated with a less accurate empirical method. It is not expected that angles of attack exceeding 30 degrees will occur often in the dense parts of the atmosphere with a maximum bending load as a path constraint. More details on this are in the Trajectory chapter. The code has been shown to accurately predict the normal coefficients for a body-alone configuration after validation with wind-tunnel results [70]. A body-alone configuration will be used in the MDO, assuming the small wings on the lower part of the second stage of the SM-3 block IIA have limited effect on aerodynamic coefficients. No data on the axial coefficient is shown for the body-alone configuration, but other configuration show that errors of around 12% can occur. These coefficients are therefore good candidates for a sensitivity analysis.

4.4. Modeling the Standard Missile-3

As the total launch vehicle will consist for the largest part of rocket stages from the Standard Missile 3, it is very important to model them as accurate as possible. Though, guaranteeing high accuracy is difficult for this system. Little information is publicly available, which is expected considering the secrecy usually surrounding information on military systems, especially relatively modern ones. In this section the approach will be shown that was used to model the SM-3 Block IIA as accurately as possible.
The SM-3 missiles have the primary purpose of intercepting short and intermediate range ballistic missiles. To do so, the missile is launched towards the threat, with an Lightweight Exo-Atmospheric Projectile (LEAP) kinetic kill vehicle (or kinetic warhead (KW)) as payload. The kinetic warhead destroys the ballistic missile re-entry vehicles by physically colliding with them. To create a powerful impact, the kill vehicle, which weighs 23.0 kg [71] in the Block IB, needs to be accelerated to a high velocity. This gives the system a promising delta V value.
The SM-3 Block IIA is a relatively new system with first flight tests performed in 2015. Successful intercept tests have been conducted in early 2017 [72]. Additionally, the system is scheduled to be tested against an ICBM target for the first time at the end of 2020 [73]. Not much data is available on the Block IIA, especially on the second and third stage, which are manufactured by Mitsubishi Heavy Industries [74]. Therefore, it is chosen to model the SM-3 Block IIA with available data on the Block IB, on which more information is available, and estimations made by experts in the field of Ballistic Missile Defense (BMD) [8, 9].
The Block IB has a total length of 6.55 meter. The booster diameter is 21 inch (0.533 m) and the other stages have a diameter of 13.5 inch (0.343 m). A breakdown of the subsystems in the SM-3 Block IB is given in Figure 4.2. The motors have the following characteristics:

- First stage: Mk 72 booster. The booster is produced by Aerojet. It has a length of 1.70 m with a diameter of 0.53 m. It holds 468 kg of an HTPB-AP propellant and has a total mass of 712 kg. It features four nozzles with thrust-vector control. The burn time is 6 seconds after which it is jettisoned [71].

- Second stage: Mk104 Dual Thrust Rocket Motor (DTRM). The second stage is also produced by Aerojet. The length of the Mk 104 motor is 2.88 m, the diameter is 0.343

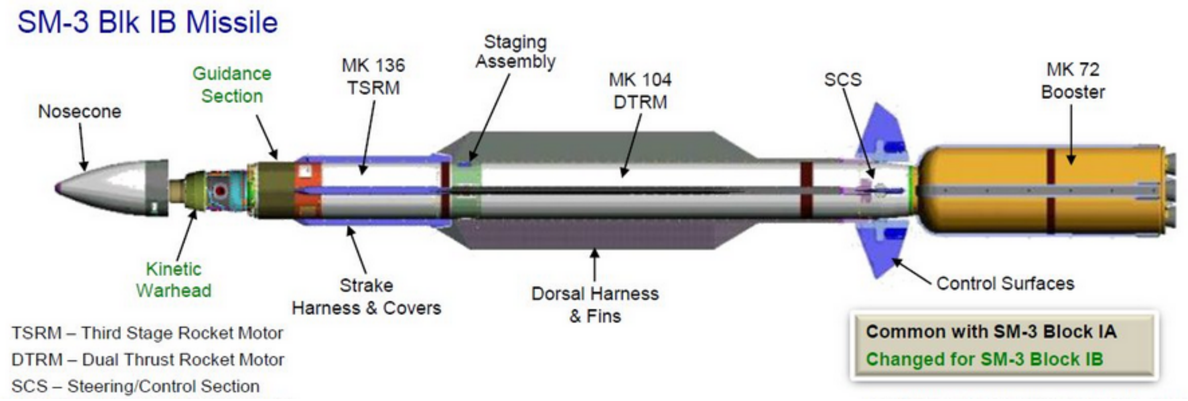

Figure 4.2: Breakdown of the subsystems in the SM-3 Block IB [7]

m, it holds 360 kg of TP-H1205/6 propellant and has a total mass of 488 kg [71]. It is reported to have a specific impulse between 260 and 265 and the motor casing is made of Type 300M (Tricent) Steel [75].

- Third stage: Mk 136 Third Stage Rocket Motor (TSRM). It is developed by ATK (now Northrop Grumman). No specific information on this motor can be found. However, in the Propulsion Products Catalog of the Northrop Grumman Corporation a high-performance upper-stage motor derived from the Mk 136 is found, called the Advanced Solid Axial Stage (ASAS) 13-30V [46]. It has the same diameter of 13.5 inch. This motor will therefore be taken as reference for the Mk 136 TSRM. It has a length of 1.0 meter, burn time of 14.3 seconds, holds 89 kg of TPH-3340A propellant and has an inert mass of 25 kg. It also features a 5 degree TVC system.

The Block IIA shares the same first stage booster with the Block IB. The second and third stage have a 21 inch diameter in the Block IIA and have a different manufacturer than the second and third stages of the Block IB. The differences in the two missiles is shown in Figure 4.3. The second and third stages of the Block IIA are more modern than the ones in the Block IB and can therefore have better performance. An expert estimates that the motors of the Block IIA have an effective specific impulses of 220, 280 and 289 for the first, second and third stages, respectively [8]. These values will be used for the model of the Block IIA. The total mass of the system has also increased from a reported 1505 kg for the IB to approximately 2313 kg (5100 lbs) for the IIA. The larger kinetic warhead of the Block IIA is estimated to weigh 60 kg, around 2.5 times more than the 23 kg of the Block IB [8, 71]. The larger motors of the Block IIA give it a burn-out velocity of 4.5 km/s, whereas the Block IB has a burn-out velocity of 3.0 km/s [9, 19].
To model the second and third stage of the Block IIA, firstly the propellant masses are scaled with the diameter increase from the IB. The lengths are assumed to remain unchanged. So, to estimate the propellant of the 21 inch stages of the IIA:

$$M_{\mathrm{p,IIA}} = \left(\frac{21}{13.5}\right)^2 \cdot M_{\mathrm{p,IB}} \tag{4.7}$$

At this point, the burn times and total inert masses of the stages remain unknown. It is assumed that both burn times and inert masses will increase considering the larger size and propellant mass of the stages. The values for these parameters will be determined with

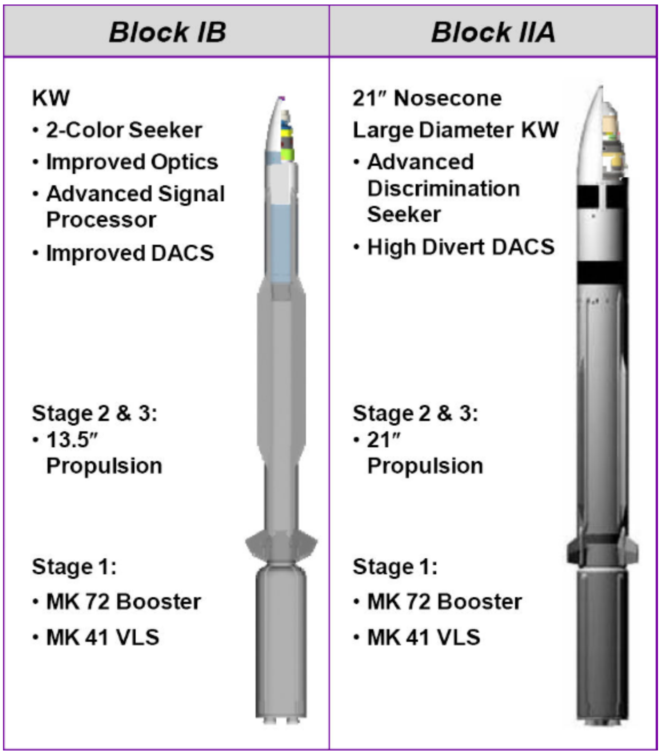

Figure 4.3: SM-3 Block IB and Block IIA comparison [8]

a performance estimation by another expert on Missile Defence [9]. It shows the performance difference of the Block IB and Block IIA in terms of altitude reached and surface distance covered. The graph is shown in Figure 4.4.

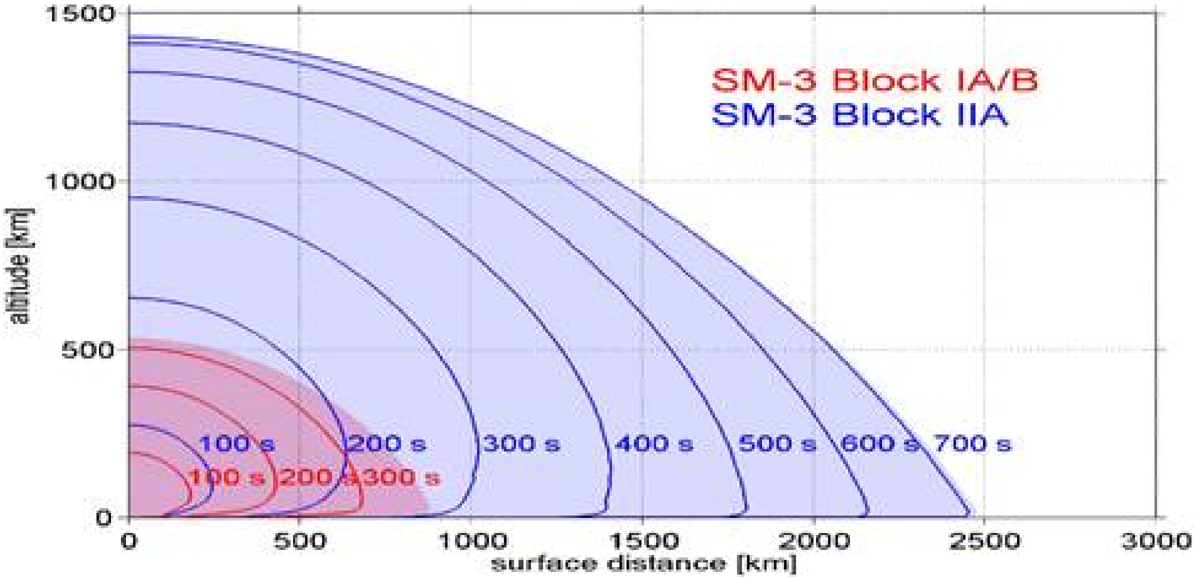

Figure 4.4: SM-3 Block IB and Block IIA altitude vs surface distance performance comparison [9]

The data used to create this image is not known exactly. But the performance is said to be determined from missile trajectory calculations using open source data. Figure 4.4 clearly shows a large range increase for the Block IIA compared to the IB. The altitudes of a vertical flight (surface distance 0) at the marked times will be used to determine the masses and burn times of the stages. From the image the altitudes were estimated. They are shown in Table 4.1.

Table 4.1: Altitudes of a vertical flight at marked times from Figure 4.4

Flight time [s]	**Altitude [km]**
100	271
200	651
300	953
400	1176
500	1325
600	1413
700	1428

An optimization is performed to find values for the masses and burn times that generate an altitude profile that resembles the altitudes at the times from Table 4.1 best. The launch environment used in the MDO is also used here. Also the same numerical integration method is used. More information on the environment and numerical integration can be found in section 5.2 and section 5.6, respectively. Also, a constant thrust model is used.

The MOEAD optimization method is used with as objectives the sum of the absolute altitude error at each time point and the error in total mass. The reported mass of 2313 kg is used and all total masses within 0.5% of that value are considered acceptable [8]. The design variables are the inert masses and the burn times of the two stages.

Missile DATCOM is used to determine the aerodynamic coefficients. From the Block IIA image from Figure 4.3 can be determined that the nose cone reaches maximum diameter at approximately 0.85 m from the top. The total nosecone has a length of around 0.97 m, which exactly corresponds with the available length when the total length of the motors (5.58 m) is subtracted from the total vehicle length (6.55 m). 0.97 m will therefore be used as available length for the upper stage motor and payload (fairing) in the MDO.

As it is a vertical flight the pitch profile will be:

$$\theta = \frac{\pi}{2} \tag{4.8}$$

The coasting times are set at 1 second after the burn-out of the first and second stages. The best solution has a total error sum of 15 km over all marked times and it results in a vehicle with the characteristics shown in Table 4.2.

Table 4.2: Characteristics of the SM-3 Block IIA model used in the MDO

	Stage 1	**Stage 2**	**Stage 3**	**Total Vehicle**
GTOW [kg]	712	1254	282.7	2312
Propellant Mass [kg]	468	869.3	214.9	1552.2
Inert Mass [kg]	244	384.7	67.8	696.5
Vacuum Thrust [kN]	168.3	86.0	18.6	-
Specific Impulse [s]	220	280	289	-
Action Time [s]	6	27.77	32.75	68.51
Length [m]	1.7	2.88	1.0	6.55

The burn-out velocity of the vehicle is 4509 m/s, which is in correspondance with the reported 4.5 km/s. The inert masses in Table 4.2 are the total inert masses of the stages, including subsystems such as steering controls, avionics and interstages.

5

Trajectory

In this chapter methods for trajectory optimization will be discussed. The trajectory is one of the discipines in the MDO. In trajectory optimization a certain measure of performance, or multiple, is to be minimized or maximized while a set of constraints is not violated. First, it is discussed how flight mechanics and numerical integrators are used to evaluate the trajectory. The environment model used to accurately represent a realistic launch environment is shown. Then, optimization of an ascent trajectory is discussed which is followed up by a part on the guidance of the vehicle and methods that have been encountered that are used to optimize the guidance.

5.1. Flight Mechanics

In this section the dynamic system used for calculating the motion of the launch vehicle is explained. First the state variables will be discussed. Then reference frames that can be used will be explained. Finally, the equations of motion of the launch vehicle will be dealt with. All these things are necessary to understand how the motion of the launch vehicle is simulated.

5.1.1. State Variables

State variables are used to express the position and velocity of a body in a certain reference frame. The state variables can be described in different ways. The ways relevant to this research are discussed here.

Cartesian State

The Cartesian state is expressed in the coordinates of the commonly used Cartesian coordinate system. The integration of the equations of motion in the Cartesian coordinate system is relatively straightforward. An advantage is that no singularities can occur in this coordinate system. The components of the Cartesian state are:

- x, y and z for the position
- $\dot{x}$, $\dot{y}$ and $\dot{z}$ for the velocity

Spherical State

The state can also be represented by spherical components. Again three components for the position and three for the velocity are used:

- distance r, longitude τ and latitude δ for the position
- ground speed V_G, flight path angle γ and heading angle χ for the velocity

The distance r is the distance from the centre of mass of the central body to the centre of mass of the vehicle. Then the longitude is positive to the east from 0 to 360 degrees. The latitude is measured along a predetermined meridian starting at the equator and is positive from 0 to 90 degrees on the northern hemisphere and negative on the southern hemisphere[10]. The ground speed V_G is the modulus of the velocity vector. γ is the angle between the velocity vector and the local horizontal plane and χ is the projection of the velocity vector in the local horizontal plane relative to the local north. The definitions of the spherical components are shown in Figure 5.1.

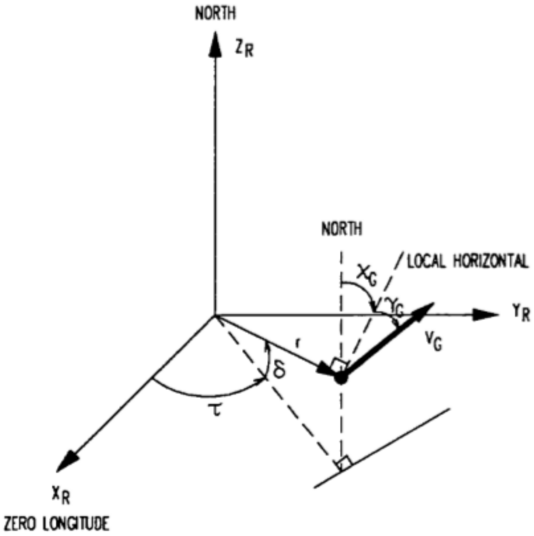

Figure 5.1: Definition of the six spherical components[10]

Orbital Elements

Another way of describing the state is the use of orbital elements. Orbital elements are particularly convenient when expressing the motion of a body around a central body in an inertial reference frame. Six orbital elements are used [10]:

- a is the semi-major axis (a > Re)
- e is the eccentricity ($0 \leq e <$ -1)
- i is the inclination (0 deg ≤ i < 180 deg)
- ω is the argument of pericenter (0 deg ≤ ω < 360 deg)
- Ω is the longitude of the ascending node (0 deg ≤ Ω < 360 deg)
- M is the mean anomaly (0 deg ≤ M < 360 deg)

Figure 5.2 and Figure 5.3 show the definitions of the orbital elements graphically.

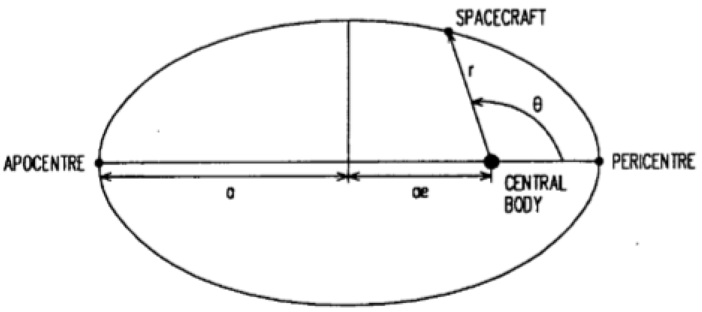

Figure 5.2: Definition of the semi-major axis and eccentricity. The body is moving at distance r and has a true anomaly of θ [10]

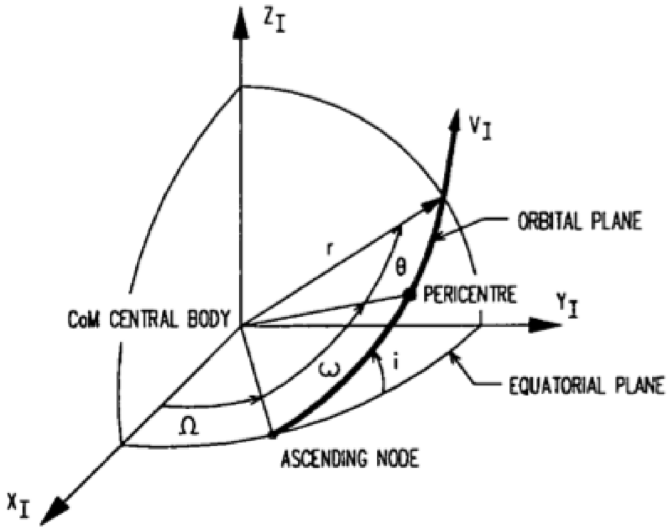

Figure 5.3: Definition of the orbital parameters ω, Ω and i [10]

The orbital elements are important as a target orbit for the launcher to inject a payload into is often defined in these elements.

5.1.2. Reference Frames

All motion is relative. Therefore to represent the motion of a launch vehicle, it must be referenced. To this end, reference frames are used. Multiple types of reference frames exist and can be used in propagating a trajectory. Using multiple reference frames has the advantage that certain equations of motion are easier to work with in a particular type of reference frame and can then transformed into another using a frame transformation. A few important reference frames will be discussed below.

- Earth-centered inertial reference frame ($OX_I Y_I Z_I$)
  As defined by [28]: "An inertial reference frame is a reference frame with respect to which a particle remains at rest or in uniform rectilinear motion if no resultant force acts upon that particle. All reference frames that perform a uniform rectilinear translational (non-rotating) motion w.r.t. an inertial reference frame and in which the time differs only by a constant from the time in the inertial reference frame are inertial." As one might expect, the origin of the Earth-centered inertial reference frame lies in the centre of the Earth. It is a pseudo inertial reference frame that can be considered as inertial when the movement of the Earth around the Sun has only a very small effect on the vehicle trajectory. The Z_I-axis has a direction north along the Earth's rotation axis. The X_I-axis intersects the equator at the line where also the ecliptic and the equator intersect. It has a direction toward the vernal equinox. The final axis, the Y_I-axis, is perpendicular to the other axes and is oriented corresponding to a right-handed frame.

- Earth-centered, Earth-fixed reference frame ($OX_C Y_C Z_C$)
  The Earth-centered, Earth-fixed reference frame is similar to the Earth centered inertial reference frame as they share the same origin and also the Z-axes are defined identically. The difference lies in the X-axes. In the Earth-centered, Earth-fixed reference frame the X-axis is defined to intersect the Greenwich meridian, which means it rotates along with the Earth. The Y_C-axis is again defined perpendicularly to the other axes. A representation of the axis in this frame are given in Figure 5.4.

- Body-fixed reference frame ($OX_B Y_B Z_B$)
  This reference uses a point on the vehicle as its origin and is fixed to the vehicle. Often for the origin the centre of mass at the initial time is chosen. The X_B-axis lies in the plane of symmetry of the body and is directed positively towards the front of the vehicle. The Z_B-axis lies also in the symmetrical plane and, of course, perpendicular to the X_B-axis. The Y_B-axis finishes the right-handed system.

- Vehicle fixed horizontal reference frame ($OX_V Y_V Z_V$)
  This frame describes the orientation of the vehicle and its velocity relative to the surface of the Earth. The origin lies in the centre of mass of the vehicle. The $X_V Y_V$-plane is the local horizontal plane. The X_V-axis points positively to the north, the Y_V-axis to the east. The Z_V-axis is in positive direction from the vehicle centre of mass to the Earth's centre.

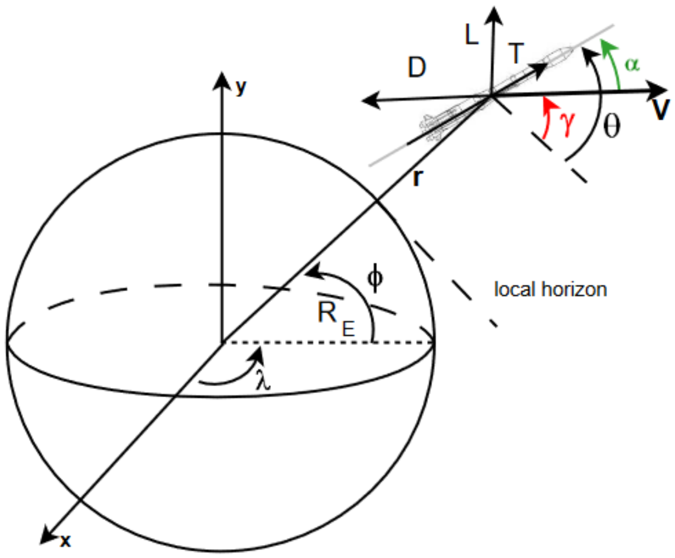

Figure 5.4: Representation of the Earth-centered, Earth-fixed reference frame [11]

- Air-path reference frame ($OX_AY_AZ_A$)
  The air-path (aerodynamic) reference frame is defined in reference to the aerodynamic velocity, which is the velocity of the centre of mass of the vehicle with respect to the ambient air. The X_A-axis is defined as positive in the direction of the velocity, the Z_A-axis lies in the symmetry plane of the vehicle in opposite direction to the lift and the Y_A-axis again completes the right-handed system.

To go from one reference frame to another a frame transformation is needed. To this end, frame transformation matrices are used. For several frame transformations the transformation matrices are given [76]. The transformation matrix is to be multiplied with the unit vectors for the three axes that are used to define the state of the vehicle.
First of all, the transformation from the Earth-centered inertial reference frame (E_I) to the Earth-centered, Earth-fixed reference frame (E_C):

$$A_{IC} = \begin{bmatrix} \cos H_G & \sin H_G & 0 \\ -\sin H_G & \cos H_G & 0 \\ 0 & 0 & 1 \end{bmatrix} \tag{5.1}$$

Here, H_G is called the Greenwich hour angle of the vernal equinox. It is defined as:

$$H_G = \omega_e (t - t_0) \tag{5.2}$$

where ω_e is the angular velocity of the Earth. The reference frames coincide when $t = t_0$. A_{IC} must be multiplied with the unit vectors of E_I to acquire the state in E_C.
The Earth-centered, Earth-fixed reference frame transforms to the Vehicle fixed horizontal reference frame (E_V) with the transformation matrix:

$$A_{CV} = \begin{bmatrix} -\sin\Phi\cos\Lambda & -\sin\Phi\sin\Lambda & \cos\Phi \\ -\sin\Lambda & \cos\Lambda & 0 \\ -\cos\Phi\cos\Lambda & -\cos\Phi\sin\Lambda & -\sin\Phi \end{bmatrix} \tag{5.3}$$

Λ is the geographic longitude and Φ is the vehicle's geocentric latitude.
The transformation from the Vehicle fixed horizontal reference frame to the Body-fixed reference frame ($\mathrm{E_B}$) is done with the use of the Euler angles. The matrix is given by:

$$A_{VB} = \begin{bmatrix} \cos\theta\cos\psi & \cos\theta\sin\psi & -\sin\theta \\ -\cos\phi\sin\psi + \sin\phi\sin\theta\cos\psi & \cos\phi\cos\psi + \sin\phi\sin\theta\sin\psi & \sin\phi\cos\theta \\ \sin\phi\sin\psi + \cos\phi\sin\theta\cos\psi & -\sin\phi\cos\psi + \cos\phi\sin\theta\sin\psi & \cos\phi\cos\theta \end{bmatrix} \tag{5.4}$$

The pitch angle is represented by θ, the yaw angle by ψ and ϕ is the bank angle.
With the above given frame transformations, now also the transformation can be made from the Earth-centered inertial reference frame to the Body-fixed reference frame:

$$A_{IB} = A_{VB} A_{CV} A_{\mathrm{IC}} \tag{5.5}$$

The software library Tudat contains the frame transformation matrices for the most commonly used reference frames.

5.2. Environment Model

In reality, a launch vehicle is subject to many different forces during ascent. Many of these forces come from the environment around the vehicle. Therefore, to be able to accurately simulate the ascent, accurate models must be implemented for the environment. The trade-off is to be made between accuracy and computational effort. Some environmental factors can be easily simplified while others are difficult to model accurately. In this section various models are discussed for the environment.

5.2.1. Gravitational Model

Gravity is one of the main forces acting on the launch vehicle. Therefore, it is readily clear that an inaccurate implementation of gravity will give inaccurate results. In his book *Principia* Newton formulated his law of gravitation, which is the basis for most gravity models. It states that two particles attract each other with a force proportional to their masses and inversely proportional to the square of the distance between them and is mathematically expressed as [28]:

$$F = G\frac{m_1 m_2}{r^2} \tag{5.6}$$

In which F is the magnitude of the gravitational force. To give direction to the force, the equation can also be written in vector form:

$$\overline{F}_2 = -G\frac{m_1 m_2}{r_2^3}\overline{r}_2 \tag{5.7}$$

Here $\overline{F}_2$ is the forces acting on m_2 exerted by m_1 and $\overline{r}_2$ is the position vector from m_1 to m_2. Equation 5.7 can be used to model the gravitational force. Subscript 1 will then represent the Earth and subscript 2 will be the rocket. The Earth's mass will be considered a point mass in this model. This is called the central gravity model.
In reality, however, the Earth is not a point mass and its irregular shape and mass distribution make that the point mass simplification is not always satisfactory. The so-called spherical harmonic gravitation model takes these irregularities into account. This model

Table 5.1: Final position error between different degrees/orders of spherical harmonic gravity fields for a reference trajectory

D/O compared	Error [m]
2/0 to 0/0 (central gravity)	283003.3
2/2 to 2/0	1512.9
3/2 to 2/2	16.3

therefore gives a more accurate estimation of the gravitational forces acting on the launch vehicle. The spherical harmonic gravitational potential is given by [77]:

$$U_{\mathrm{B}}(\mathbf{r}_{\mathrm{A}}) = \frac{\mu}{r}\sum_{l=0}^{\infty}\sum_{m=0}^{l}\left(\frac{R}{r}\right)^{l} P_{lm}(\sin\phi)\left(C_{lm}\cos m\theta + S_{lm}\sin m\theta\right) \tag{5.8}$$

So, the potential is defined by the gravitational parameter μ, a reference radius R, Legendre polynomials P_{lm} and C_{lm} and S_{lm}, which are tesseral harmonic coefficients for $n \neq m$ and sectoral harmonic coefficients for $n = m$[78]. The harmonic coefficients can also be implemented in normalized form $\overline{C}_{lm}$ and $\overline{S}_{lm}$. The Tudat environment always uses the normalized coefficients.

To determine which degree and order of the spherical harmonic gravity field are relevant for this research, a reference trajectory is run with different degree/orders (D/O) of the gravity field and compared. The reference trajectory used is explained in more detail in subsection 5.6.3. The final position error is given between the different gravity fields. The results of the comparison are shown in Table 5.1. Table 5.1 shows that adding the J_2-term (D/O 2/0) has a big influence on the final position compared to the central gravity model. This was expected as J_2 has the largest effect and is used in many other studies [23, 26, 43, 66]. In many models J_2 is the only term added to the gravity field. However, D/O 2/2 shows a position difference of 1512.9 meter compared to just 2/0. Adding J_3 on top of D/O 2/2 shows only a limited error of 16.3 meter. Therefore, it is chosen to use D/O 2/2 in the MDO. Gravitational accelerations exerted on the vehicle by other celestial bodies, such as the Moon or Sun, will not be included in the environment model.

5.2.2. Atmosphere Model

Another main force acting on the launch vehicle is the aerodynamic force. The aerodynamic forces come from the vehicle's interaction with the atmosphere. Especially during the initial phase of the ascent, the atmosphere plays a large role in choosing the trajectory. Therefore, to obtain accurate results, the atmosphere must be adequately modelled. The main characteristics of the atmosphere are pressure, density and temperature. These parameters differ with altitude and also are variable with time due to many effects, for example solar activity. The atmosphere is a difficult environment to model and many different models exist. They vary from simpler models to complicated models that are therefore also computationally intensive to evaluate. A few different models are available in Tudat.

First of all, it features the exponential atmosphere model, which is the simplest model. This model is greatly simplified and for that reason also available for analytical analysis. It assumes a constant temperature with altitude (isothermal atmosphere) and a constant composition with constant thermodynamic properties[77]. It considers the atmosphere to behave as a perfect gas following the ideal gas law [78]. Secondly, a more accurate model

Table 5.2: Values for several parameters for the different layers of US Standard Atmosphere 1976 [14]

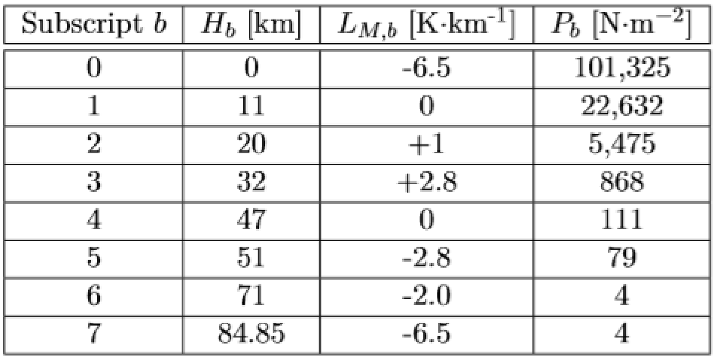

Subscript b	H_b [km]	$L_{M,b}$ [K·km^{-1}]	P_b [N·m^{-2}]
0	0	-6.5	101,325
1	11	0	22,632
2	20	+1	5,475
3	32	+2.8	868
4	47	0	111
5	51	-2.8	79
6	71	-2.0	4
7	84.85	-6.5	4

is available with the US Standard Atmosphere 1976 (US1976). It divided the atmosphere in multiple layers and determines the ranges of atmospheric parameters for the specific layers. Thirdly, there is the most accurate model: the NLRMSISE-00 model. The NRLMSISE-00 atmosphere model is an empirical model of the atmosphere. This model takes into account temporal variations, geomagnetic activity and solar activity and is therefore a more realistic model. However, because of its complexity it would take a lot of computational effort to perform simulations using this model. Also, the time-varying aspects of this model are not relevant in the MDO. Therefore, it is probably not the best option for the problem in this thesis research.

It is chosen to use the US1976 model in the MDO, which will therefore be explained further. This atmosphere model has been used in many other studies for ascent trajectories [14, 23, 26, 43, 68].

US Standard Atmosphere 1976

The US Standard Atmosphere 1976 model presents values for parameters up to an altitude of 1000 km at a latitude of 45 degrees North. This model assumes linear rates for the lower atmosphere and composition variations at higher altitudes. It is not time- or location-dependent. The US 1976 uses both the geometric altitude [m] and the geopotential altitude [m'], which here are denoted as Z and H respectively. The lower atmosphere, which reaches an altitude of 86 km, is divided in 8 layers. The temperature in each layer is then given by:

$$T_{\mathrm{M}} = T_{\mathrm{M},b} + L_{\mathrm{M},b} \cdot (H - H_b) \tag{5.9}$$

where T_{M} is the molecular scale temperature and b is the subscript for the atmospheric layers ranging from 0 to 7. $T_{\mathrm{M},b}$ is the molecular scale temperature of layer b at the lowest altitude. $L_{\mathrm{M},b}$ is the molecular scale temperature gradient and $(H - H_b)$ is the difference in geopotential height at the evaluated altitude and the lowest altitude of layer b. The values for these parameters are given in Table 5.2. For higher altitudes than 86 km, Equation 5.9 is not applicable anymore. From 86 km, the next 5 km of altitude is considered isothermal at 186.87 K [78]. From 91 km to 110 km the temperature is calculated with the following equation:

$$T = T_{\mathrm{c}} + A \cdot \left(1 - \left(\frac{Z - Z_8}{b}\right)^2\right)^{0.5} \tag{5.10}$$

The values in this equation are 263.19 K for T_{c}, -76.3232 K for A, 19.9429 km for b and 91 km for Z_8. For altitudes between 110 km and 120 km the following equation is used for the temperature:

$$T = T_9 + L_9 \cdot (Z - Z_9) \tag{5.11}$$

Where T_9 is 240 K, L_9 is 12 K/km and Z_9 is 110 km. Finally, for altitudes from 120 km up to 1,000 km [79]:

$$T = T_\infty - (T_\infty - T_{10}) \cdot \exp(-\lambda\xi) \tag{5.12}$$

with

$$\lambda = 12/\,(T_\infty - T_{10}) \tag{5.13}$$

$$\xi = \frac{(Z - Z_{10}) \cdot (r_0 + Z_{10})}{(r_0 + Z)} \tag{5.14}$$

T_∞ is the exo-atmospheric reference temperature of 1000 K, T_{10} is 360 K, Z_{10} is 120 km and r_0 is 6356.76 km.
With the temperatures, the pressure in the atmosphere can be calculated. For altitudes up to 86 km that is done with[79]:

$$P = P_b \left(\frac{T_{M,b}}{T_{\mathrm{M},b} + L_{\mathrm{M},b}\,(H - H_b)} \right)^{\left(\frac{g_0 - M_0}{R^* \cdot L_{\mathrm{M},b}} \right)} \tag{5.15}$$

Or for the isothermal layers below 86 km ($L_{M,b} = 0$):

$$P = P_b \cdot \exp\left(\frac{-g_0 \cdot M \cdot (H - H_b)}{R^* \cdot T_{\mathrm{M},b}} \right) \tag{5.16}$$

For altitudes larger than 86 km, the pressure is calculated using an alternative version of the ideal gas law[78]:

$$P = \frac{N \cdot R^* \cdot T}{N_\mathrm{A}} \tag{5.17}$$

Where N is the total density number and N_A is Avogadro's constant. The total density number is calculated using a table from [79] and interpolating linearly. Direct computation of the densities of the individual gas species would need complex formulas and be very time-consuming.
Finally, the density is calculated with the normal form of the ideal gas law:

$$\rho = \frac{p \cdot M}{R^* \cdot T} \tag{5.18}$$

5.3. Ascent Trajectory Optimization Problem

An ascent trajectory optimization problem is a nonlinear optimization problem. It can be described by differential equations. It starts with the state equation [34]:

$$\dot{\overline{x}} = \overline{f}[\overline{x}(t), \overline{u}(t), t] \tag{5.19}$$

where $\overline{x}(t)$ is the vector of the state variables and $\overline{u}(t)$ are the control variables. Just as for the general optimization problem, the ascent trajectory problem can be constrained. State variables and control variables can both be constrained. These so-called path constraints are written as:

$$\overline{g}(\overline{x}, \overline{u}, t) \geq 0 \tag{5.20}$$

When no control constraints are violated, the control history is called an admissible control. Similarly for the trajectory, the state history is called an admissible trajectory if the state constraints are satisfied. Also certain conditions concerning the initial and final state can be imposed and are called boundary conditions. They are written as:

$$\psi_0\left(\overline{x}_0, t_0\right) \geq 0 \tag{5.21}$$

$$\psi_f\left(\overline{x}_f, t_f\right) \geq 0 \tag{5.22}$$

The objective function is then defined as [34]:

$$J = \phi\left[\overline{x}\left(t_f\right), t_f\right] + \int_{t_0}^{t_f} L[\overline{x}(t), \overline{u}(t), t] \tag{5.23}$$

in which ϕ and L are scalar functions.
So, starting from the initial conditions a control $\overline{u}(t)$ can be applied that effectuates a certain trajectory $\overline{x}(t)$ which corresponds to a certain value for the objective function J. It is therefore the goal to find the control function that effectuates a trajectory that minimizes J, satisfying all constraints. The control function that minimizes J is called the optimal control and, again similarly, the optimal state history is called the optimal trajectory.

5.4. Guidance

To guide the vehicle through a certain trajectory, a guidance law is needed. To convert a trajectory optimization problem into a parameter optimization problem transcription methods are used. Two of the most common methods for transcribing a continuous trajectory optimization problem into a form with a finite number of variables are shooting methods and collocation. Both those methods can be implemented as a direct or indirect method. The difference between direct and indirect transcription methods is that indirect transcription methods have an extra layer of equations for finding the optimal controls.
However, in literature where heuristic algorithms are used for trajectory optimization, information on the transcription methods is completely left out. Usually, design or guidance variables are determined for which then the simulation is performed and checked if the set of variables does not lead to a violation of the constraints.

Multiple methods are found in literature. One method is encountered where pitch angles at fixed points during the burn are taken as design variables and then interpolated linearly for the whole ascent [14, 26]. Another method models the pitch profile as a certain order polynomial function and then optimizes the coefficients. Thirdly, a method is found where the ascent is divided in different segments [12, 66, 68, 80, 81]. Each segment has its own set of design variables that can be optimized. After some preliminary testing, it was concluded that a slightly altered version of the last method works best for a launch vehicle with short burn times such as the SM-3. The guidance model will only optimize the pitch profile.

5.4.1. Trajectory Optimization Method

The method divides the ascent in four segments. The different segments are:

- Vertical lift-off

- Pitch turnover
- Pitch angle optimization
- Bi-linear tangent law

For these phases, a set of guidance variables can be defined that are used to optimize the pitch profile. The different segments are explained below.

Vertical Segment

After launch, the vehicle is assumed to travel vertically from the Mk41 VLS to an altitude of 50 m. No guidance variables are determined for this phase. The pitch angle has a value of:

$$\theta = \frac{\pi}{2} \tag{5.24}$$

Pitch Turnover

Secondly, we have the pitch turnover phase. During this phase first, a linear pitch angle decrease occurs, followed by a exponential decay of the pitch angle. The linear decrease moves the pitch angle away from the 90 degrees from the vertical flight. Then the exponential decay moves the pitch angle towards the flight path angle. This is needed to have a continuous pitch profile. A graphical representation is given in Figure 5.5.

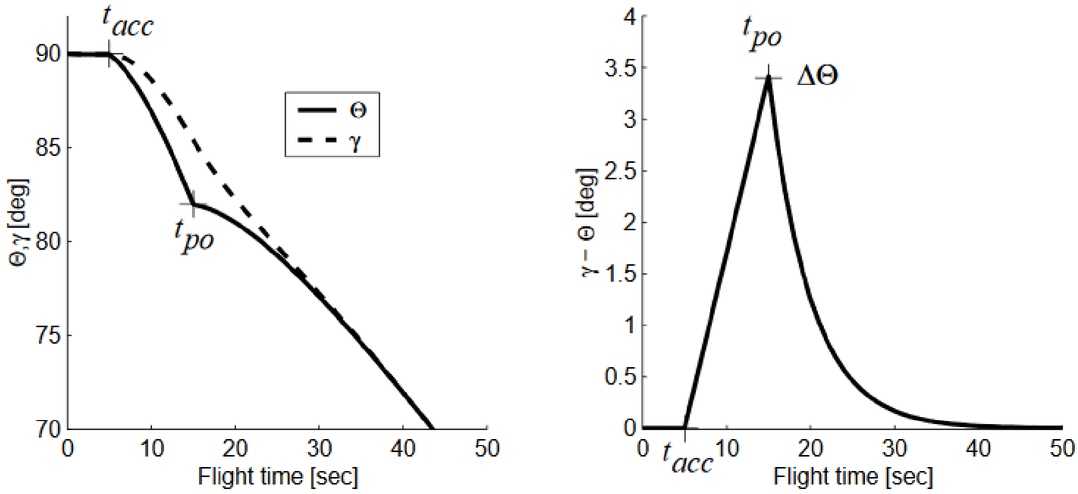

Figure 5.5: Pitch over maneuver and comparison to flight-path angle [12]

Mathematically, the pitch angle is defined as:

$$\begin{cases} \theta = \gamma - \frac{t - t_{\text{acc}}}{t_{\text{po}} - t_{\text{acc}}} \Delta\theta_{\text{po}} & \text{for } t_{\text{acc}} < t < t_{\text{acc}} + \Delta t_{\text{po}} \\ \theta = \gamma - \Delta\theta_{\text{po}} \exp\left(\frac{-(t - t_{\text{po}})}{t_c}\right) & \text{for } t_{\text{acc}} + \Delta t_{\text{po}} < t < t_{\text{F2}} \end{cases} \tag{5.25}$$

where t_{acc} is the start of the pitch over maneuver, t_{po} is the end time of the linear decrease and t_c is a time constant which is a parameter of the rotational dynamics of the launcher. Only one source can be found for a value of the time constant, however only for larger launch vehicles [68]. Therefore, the same value is used here, which is 3 seconds. This segments has two optimization variables: the time difference $t_{\mathrm{po}} - t_{\mathrm{acc}} = \Delta t_{\mathrm{po}}$ and $\Delta\theta_{\mathrm{po}}$. t_{acc} is defined as the first time step that the altitude is higher than 50 m. The end time of this segment t_{F2} is reached when the difference between the pitch angle and flight path angle is small, here taken as smaller than 0.005 radians. Mathematically this can be expressed as:

$$t_{\mathrm{F2}} = t_{\mathrm{acc}} + \Delta t_{\mathrm{po}} - t_{\mathrm{c}} \cdot \log\left(\frac{0.005}{\Delta\theta_{\mathrm{po}}}\right) \tag{5.26}$$

Pitch Angle Optimization

Often, after the pitch over, a gravity turn segment begins. During the gravity turn the pitch angle is equal to the flight path angle, reducing the angle of attack to zero:

$$\theta = \gamma \tag{5.27}$$

Not having an angle of attack reduces the aerodynamic load on the vehicle, but produces more gravity losses. Testing has indicated that a gravity turn is not the best option for this segment for the launch vehicle. Initially, the guidance of this segment was designed to have a optimizable period of time of gravity turn, after which some pitch angles at certain nodes were optimized. It turned out that the period of time for the gravity turn always reduced to zero seconds for the best solutions. This can be explained by the fact that the first three stages of the launch vehicle have very short burn times and therefore, to gain the horizontal velocity for the orbit, more pitch angle reduction is needed earlier in the flight. For that reason, this segment will only include optimizable pitch angles occurring at predetermined nodes. The pitch profile consisting of pitch angles at five nodes, of which four as guidance variables, will be made continuous by linear interpolation. The first pitch angle is equal to the flight path angle at t_{F2}, this pitch angle is denoted as θ_0. Of the next four optimizable pitch angle, three will be distributed uniformly over time from t_{F2} to the burn-out of the third stage, after which a long coasting phase starts. The length of the coasting period is also a design variable. The fourth angle will be pitch angle at the end of the coasting phase. The optimization of the pitch angle during the coasting phase is not very important, as the thrust is zero and the aerodynamic forces are very small at the altitudes during the phase. However, the last pitch angle is one of the parameters of the next segment, but as it is interpolated with the other pitch angles in this segment, it has been added here. The design variables for the pitch angles are actually pitch angle changes at each node, denoted as $\Delta\theta_i$, where i is the number of the node. The pitch angle at node i, θ_i, will be determined with:

$$\theta_i = \theta_{i-1} + \Delta\theta_i \tag{5.28}$$

Bi-linear Tangent Law

In the fourth phase the pitch angle is modeled according to the bi-linear tangent law. [12] shows that the bi-linear tangent law works well for upper stages. The bi-linear tangent law has just three design variables, making it an efficient method. Also, [82] states that for a

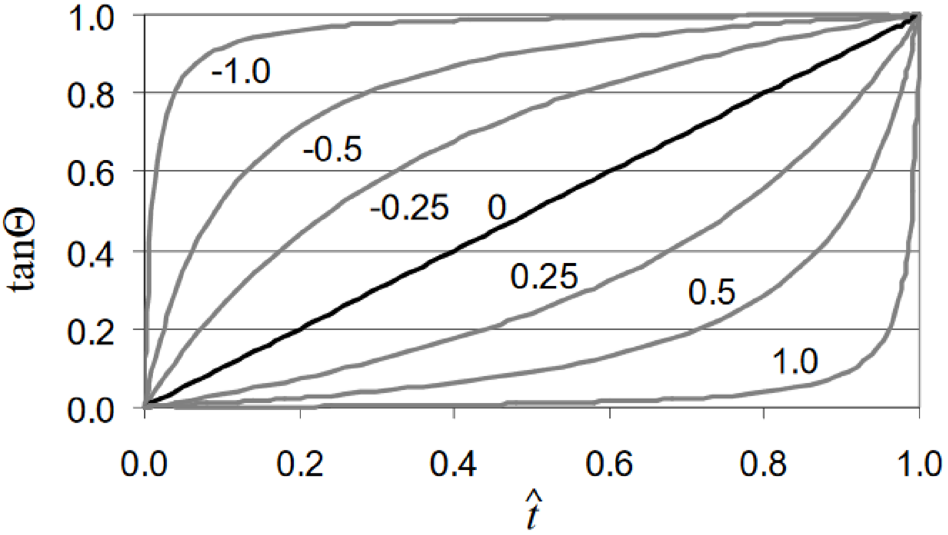

Figure 5.6: Effect of the curvature parameter ξ for a=100. The end values are $\tan\theta_0 = 0$, and $\tan\theta_f = 1$, respectively. [12]

spherical Earth the bi-linear tangent law is recognized as the optimal steering control.
The bi-linear tangent law is the solution of a very simple control problem, called the “maximum velocity transfer to a rectilinear path” [83]. The problem is stated as:
"Consider a particle of mass m, acted upon by a force of magnitude ma. We assume planar motion and use an inertial coordinate system x, y to locate the particle; the velocity components of the particle are u, v. The thrust-direction angle $\beta(t)$ is the control variable of the system. ... We wish to transfer the particle to a path parallel to the x-axis, a distance h away, in a given time T with the maximum value of $u(t)$.”
The bi-linear tangent law is only valid for specific conditions, but it generates adequate results also for the trajectory of launch vehicles [84]. When the pitch angle is substituted for the control angle β, mathematically the bi-linear tangent law can be written as [12]:

$$\tan\theta = \frac{c\tan\theta_0 + (\tan\theta_\mathrm{f} - c\tan\theta_0)\,\hat{t}}{c + (1-c)\hat{t}} \text{ with } \hat{t} = \frac{(t - t_0)}{\left(t_f - t_0\right)} \tag{5.29}$$

where θ_0 is the pitch angle at the beginning of the phase, which is the last optimized pitch angle of the previous segment, θ_f is the pitch angle at the end of the phase and c is a measure of curvature. In order to make the expression symmetric, an exponent is added:

$$\tan\theta = \frac{a^\xi\tan\theta_0 + \left(\tan\theta_\mathrm{f} - a^\xi\tan\theta_0\right)\hat{t}}{a^\xi + \left(1 - a^\xi\right)\hat{t}} \tag{5.30}$$

where a is an arbitrary constant bigger than 1 and ξ lies in the domain [-1,1]. A graphical representation of the law is given in Figure 5.6. The description in Equation 5.30 is used in the MDO. a is set constant at 100, so that leaves θ_f and ξ as guidance variables.

5.5. Path constraints

The trajectory is restricted by path constraints. During the ascent forces will be exerted on the launch vehicle that could jeopardize its integrity or the integrity of the payload. It is therefore necessary to avoid such forces. Safety issues concerning the launch site location or launch direction can be taken as constraints, but will not be considered here. The main path constraints will be shortly discussed below. If any of the constraints are violated, a large value will be given to the fitness function as a penalty.

5.5.1. Dynamic Pressure and Heat Flux

The dynamic pressure is defined as:

$$q = \frac{1}{2}\rho V^2 \tag{5.31}$$

It is an indicator for the aerodynamic forces acting on the launch vehicle. It can be seen that when the rocket accelerates, the aerodynamic forces on the rocket increase. The atmospheric density decreases with altitude and thus, combining the effect of the velocity increase and atmospheric density decrease, during ascent a moment will occur where the dynamic pressure reaches a maximum. This moment is often called 'maximum q'. During this phase the aerodynamic forces are largest and therefore the risk to the structural integrity of the rocket is also largest. Therefore, the maximum allowable dynamic pressure is often taken as a constraint. However, the dynamic pressures occurring in the MDO are not expected to be larger than the dynamic pressures occurring during a regular launch of the SM-3. It can consequently be expected that the structure can handle those dynamic pressures. Moreover, it will be used indirectly in the constraint for the bending load, which will be explained below. A constraint for the maximum dynamic pressure is for those reasons not set in the MDO.

The same holds for the heat flux during ascent. When a launch vehicle travels through the atmosphere with a high velocity, the atmosphere will start heating the vehicle. It must be avoided that the materials are heated to temperatures that cause damage. As a constraint often the stagnation point heat flux is taken. At the stagnation point the heat flux is usually largest and gives a good indication of the total heat flux. This heat flux is mostly the convective heat flux. Radiative heat flux has very little effect during an ascent trajectory, because the velocities are too low [85]. The convective heat flux at the stagnation point can be calculated with [86]:

$$\dot{Q}_c = C\left(\frac{\rho}{\rho_0}\right)^n \left(\frac{V}{V_{circ}}\right)^m \frac{1}{\sqrt{R_\mathrm{N}}} \tag{5.32}$$

where R_N is the nose radius of the rocket and for the free stream $C = 1.1097 \cdot 10^8\ \mathrm{W/m^{3/2}}$, $n = 0.5$, $m = 3.0$, $V_{circ} = 7905\ \mathrm{m/s}$ and $\rho_0 = 1.225\ \mathrm{kg/m^3}$. Besides the fact that the heat flux is not expected to exceed values occurring during regular SM-3 launches, also more blunt nosecones will be found in the MDO. These more blunt nosecones will increase the nose radius R_N, causing the heat flux to decrease according to Equation 5.32. No heat flux constraint will therefore be implemented in the MDO.

5.5.2. Axial Acceleration

Thrust from the rocket engines accelerate the launch vehicle axially. With a high thrust-to-weight ratio, the acceleration can be considerable. This puts a large stress on the structure. The axial acceleration is expressed in g's as [12]:

$$a_\mathrm{x} = \frac{T - m \cdot \cos\theta - D \cdot \cos\alpha + L \cdot \sin\alpha}{m g_0} \tag{5.33}$$

m indicates the launch vehicle mass at the moment that the value is determined. As the ascent progresses, fuel will be consumed and thus the mass of the vehicle reduces. This in turn causes the acceleration to increase continuously during flight if no regressive burn configuration is used. The rocket structure and the payload must be able to cope with the accelerations. The value for the constraint is based on two sources. Firstly, the SS520-5 launch vehicle launched a 3.2 kg payload. Its upper stage motor had a gross take-off weight of 86.27 kg, excluding the nozzle [18]. The maximum vacuum thrust of the stage was 12.76 kN. Using the nozzle mass estimation relationship from Equation 3.2.4 (without TVC, as upper stage of the SS520-5 does not have that) and estimating the payload adapter to have a mass of 2 kg as seen in section 4.2 results in a total mass of the upper rocket section of roughly 99 kg. The SS520-5 upper stage does not have avionics. It can then be calculated that during the upper stage burn an axial acceleration of at least roughly 13 g must have occurred. The launch was successful, therefore clearly the launch vehicle and payload were able to handle the forces. Secondly, the ISIS ISIPOD 1-Unit CubeSat deployer is reported to be able withstand a 15 g quasi static load [61]. Therefore, in the MDO the constraint is set at 15 g.

5.5.3. Bending Load

Bending loads are very important to constrain as they are very capable of causing serious damages to launch vehicles. The bending load can be defined as the product of the dynamic pressure and the total angle of attack. Mathematically this is written as:

$$n_\mathrm{b} = q \cdot \alpha_\mathrm{t} \tag{5.34}$$

The total angle of attack be be calculated with the formula [87]:

$$\alpha_\mathrm{t} = \arccos(\cos\alpha \cdot \cos\beta) \tag{5.35}$$

in which α is the angle of attack and β is the angle of sideslip. The angle of sideslip is set to 0 during the ascent which yields:

$$\alpha_\mathrm{t} = \alpha \tag{5.36}$$

The value for the bending load constraints is based on the Pegasus XL, which is an air-launched launch vehicle. Its user's guide states that the maximum dynamic pressure occurs at around 30 seconds after ignition [88]. The value of the maximum dynamic pressure is reported to be 1200 pounds per square foot or $5.75 \cdot 10^4$ Pa. Combining this value with an angle of attack of approximately 10 degrees occurring at 30 seconds [89], this gives a bending load of 10,000 Pa·rad. So, 10,000 Pa·rad will be set as the limit for the bending load. Moreover, it can be noted that the launch vehicle in the MDO is smaller and has a smaller slenderness ratio than the Pegasus XL with 12.4 and 13.3, respectively. This suggests that the bending load limit for the SM-3 could be larger [14]. The effect of a larger limit will be investigated in a sensitivity analysis.

5.5.4. Final Conditions

The goal is to insert a payload into a predetermined orbit. Therefore it is necessary that the final conditions correspond to the parameters of the target orbit. The exact orbital parameters are unlikely to be achieved, but inequality constraints can be used to make sure that only trajectories with final conditions very close to the target orbit are permitted.

As mentioned before, the optimization objectives are payload mass and perigee altitude of the orbit. It is expected that the eccentricities of the optimal orbits will reduce to close to 0, as for a certain perigee altitude a circular orbit requires the least energy and thus has the highest payload potential. To help the optimization converge to circular orbits quickly a penalty function P is defined that is added to the objective function when the final eccentricity e is bigger than 0.02:

$$P = e \cdot 10000 + 1000 \tag{5.37}$$

Only orbits that have a perigee altitude between 200 km and 700 km are considered. The perigee altitude h_{p} is calculated with:

$$h_{\mathrm{p}} = a \cdot (1 - e) - R_{\mathrm{E}} \tag{5.38}$$

where a is the semi-major axis and R_{E} the average radius of the Earth. If h_{p} is below 180 km or above 715 km, the penalty function will have the form of:

$$P = 100000 \tag{5.39}$$

It must be noted that the boundaries for the penalty function are taken a bit more relaxed to allow a better optimization near the real boundaries. If no orbital constraints are violated at the final time-step, the penalty function will be 0.

5.6. Numerical Integration

In astrodynamics, the equations of motion often come in a form that is not solvable analytically. Only for very specific situations or assumptions it may be possible to get an analytical solution. Most problems do not come in those specific situations and many assumptions will cause the solution to be far from reality. Therefore, it is often necessary to make use of numerical integration to obtain a solution. A numerical integrator will calculate the value of the state variables for the next step in time. The solution for this next step in time will have an error, which is also important to quantify.

All these methods start at the same points where a differential equation needs to be solved of the form:

$$\dot{y}(t) = f(y, t) \tag{5.40}$$

and has an initial value of

$$y(t_0) = y_0 \tag{5.41}$$

In literature on the optimization of a launch vehicle and/or the ascent trajectory, Runge-Kutta methods are often used [11, 14, 23, 25, 26, 43, 66]. Different methods are used, from a fixed-step Runge-Kutta 4 (RK4) method to a variable step 7-8th order Runge-Kutta-Fehlberg (RKF) method. Research suggests that variable step methods perform better than fixed-step methods in most linear and non-linear problems [90]. First, the theory behind the Runge-Kutta methods will be explained. Then different integrators will be compared and the best one for this MDO will be chosen.

5.6.1. Runge-Kutta methods

In Euler's method, the slope of the tangent is used to approximate the next value, while actually the approximate increment should actually approach the slope of the secant. The

mathematicians Carl Runge and Wilhelm Kutta found a solution to this problem. It is based on the gradients of multiple points within the integration step. The basics of the Runge-Kutta methods are explained here [91]:
The general Runge-Kutta formula for s stages uses s function evaluations

$$\begin{aligned} k_1 &= f\left(t_0 + c_1 h, y_0\right) \\ k_i &= f\left(t_0 + c_i h, y_0 + h\sum_{j=1}^{i-1} a_{ij} k_j\right) \quad (i = 2 \dots s) \end{aligned} \tag{5.42}$$

to form the increment function:

$$\Phi = \sum_{i=1}^{s} b_i k_i \tag{5.43}$$

The method uses the coefficients

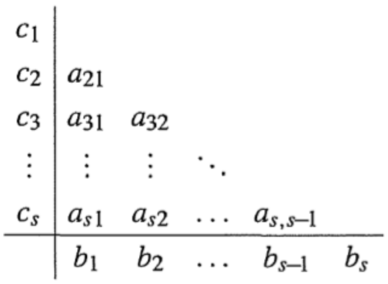

$$\begin{array}{c|ccccc} c_1 & & & & & \\ c_2 & a_{21} & & & & \\ c_3 & a_{31} & a_{32} & & & \\ \vdots & \vdots & \vdots & \ddots & & \\ c_s & a_{s1} & a_{s2} & \dots & a_{s,s-1} & \\ \hline & b_1 & b_2 & \dots & b_{s-1} & b_s \end{array} \tag{5.44}$$

where the coefficients follow the relations

$$\sum_{i=1}^{s} b_i = 1, \quad c_1 = 0 \quad , \quad c_i = \sum_{j=1}^{i-1} a_{ij} \quad (i > 1) \tag{5.45}$$

To show how this is put into practice, the working of the classical Runge-Kutta 4th-order method is shown. The method uses four slopes between the current point and the next integration step:

$$\begin{aligned} k_1 &= f\left(t_0, y_0\right) \\ k_2 &= f\left(t_0 + h/2, y_0 + hk_1/2\right) \\ k_3 &= f\left(t_0 + h/2, y_0 + hk_2/2\right) \\ k_4 &= f\left(t_0 + h, y_0 + hk_3\right) \end{aligned} \tag{5.46}$$

With these slopes the increment function becomes:

$$\Phi_{\mathrm{RK4}} = \frac{1}{6}\left(k_1 + 2k_2 + 2k_3 + k_4\right) \tag{5.47}$$

In the following figure a visual representation is given for the RK4 method and the four slopes.

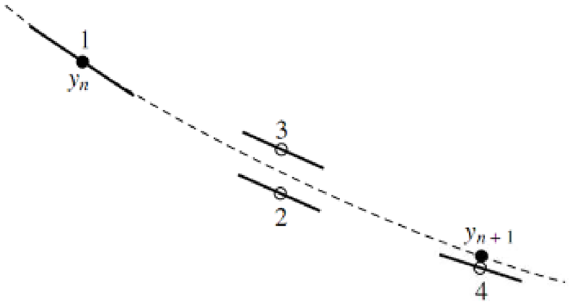

Figure 5.7: Visual representation of the four slopes of the RK4 integrator [13]

The local truncation error with order p is expressed as:

$$e = \left| y(t_0 + h) - \eta(t_0 + h) \right| \leq C \cdot h^p \tag{5.48}$$

The local truncation error of the RK4 method is of the order p = 5.
The accuracy of the RK4 method is similar to that of the 4th-order Taylor polynomial method. However, the RK4 method does not need to calculate the higher order derivatives, which can be quite extensive, and thus only uses function evaluations of f to calculate the value in the next time step.
Several Runge-Kutta methods can be found with the same number of stages due to the fact that the coefficients are not determined uniquely. To approximate the local truncation error methods of neighbouring order can be used that are based on the same set of function evaluations. Such methods are called embedded Runge-Kutta methods. A simple local truncation error approximation is a necessary condition for efficient step size control. The error approximation starts with the two independent approximation of the next step:

$$\begin{aligned} \eta(t_0 + h) &= \boldsymbol{y}_0 + h \sum_{i=1}^{s} b_i \boldsymbol{k}_i \\ \hat{\eta}(t_0 + h) &= \boldsymbol{y}_0 + h \sum_{i=1}^{s} \hat{b}_i k_i \end{aligned} \tag{5.49}$$

The methods used with order p and p+1 both have local truncation errors with in the form of

$$\begin{aligned} e &= \left| y(t_0 + h) - \eta(t_0 + h) \right| \leq c h^{p+1} \\ \hat{e} &= \left| y(t_0 + h) - \hat{\eta}(t_0 + h) \right| \leq \hat{c} h^{p+2} \end{aligned} \tag{5.50}$$

$\hat{e}$ is smaller than e by the order of h. Then the local truncation error can be approximated:

$$e = |y - \eta| \approx |\hat{\eta} - \eta| \tag{5.51}$$

5.6.2. Stepsize control

Stepsize control is an important part of an integrator. On one hand, a smaller stepsize usually gives a greater accuracy. However, small stepsizes can cause very high computation times. Therefore, a trade-off must be made between accuracy and computational effort.
The error estimate from embedded methods form the basis for step size control for Runge-Kutta methods. It starts with an estimation of the local truncation error for a single integration step:

$$e(h) \approx |\hat{\eta} - \eta| \tag{5.52}$$

If the value for this error is greater than a certain tolerance ε, a smaller stepsize h^* must be chosen and the step must be repeated. With the knowledge that e(h) is proportional to h^{p+1}, the local truncation error for the new stepsize then becomes:

$$e\left(h^*\right) = e(h)\left(\frac{h^*}{h}\right)^{p+1} \approx |\hat{\eta}-\eta|\left(\frac{h^*}{h}\right)^{p+1} \tag{5.53}$$

The requirement that the error must be smaller than the tolerance gives the maximum stepsize:

$$h^* = \sqrt[p+1]{\frac{\varepsilon}{e(h)}} \cdot h \approx p+1\sqrt{\frac{\varepsilon}{|\hat{\eta}-\eta|}} \cdot h \tag{5.54}$$

Often, this maximum stepsize is multiplied with a factor of 0.9 to ensure that another unsuccessful step is avoided. This is also standard procedure within Tudat.

5.6.3. Integrator Selection

Tudat contains multiple Runge-Kutta methods. It contains a RK4 integrator, but also RKF methods. RKF methods are embedded methods and can be used as variable stepsize integrators in Tudat. Tudat features a Runge-Kutta-Fehlberg method of order 4-5 (RKF45), RKF56 and RKF78. The RKF45 method proposed by Fehlberg in 1969 is a fourth-order method with a fifth-order error estimator [92]. Tudat also features a Runge-Kutta87Dormand-Prince method (RK87DP). All these methods will be compared for a reference trajectory.

For the reference trajectory a vehicle is used that has the design variables of one of the Pareto individuals found during testing. To make sure that only the integrator error is evaluated, errors from a differing pitch profile are avoided by selecting a pitch profile without discrete events and without parts of the pitch profile depending on values occurring during the trajectory. For this reference pitch profile, the pitch angle reduces during the action time (t_a) of the launch vehicle. With some trial and error a pitch profile was found for a reasonable orbit with the following equation:

$$\theta = \pi - \pi \cdot \left(\frac{t}{t_\text{a} - 100}\right)^{0.3} \tag{5.55}$$

The same environment model is used as in the MDO.

To select an integration method, firstly, the final position error is evaluated. The error is plotted against the number of function evaluations performed by the integrator in Figure 5.8. A position error under 100 m is estimated to be acceptable. It will be tested if a much more accurate method generates different results in the Results chapter.

A RK87DP method with relative and absolute tolerance of 10^{-14} is used as benchmark. Other methods with very small tolerances (RKF56 and RKF45) show errors of only a few millimeters with this method, which makes it a good choice for the benchmark.

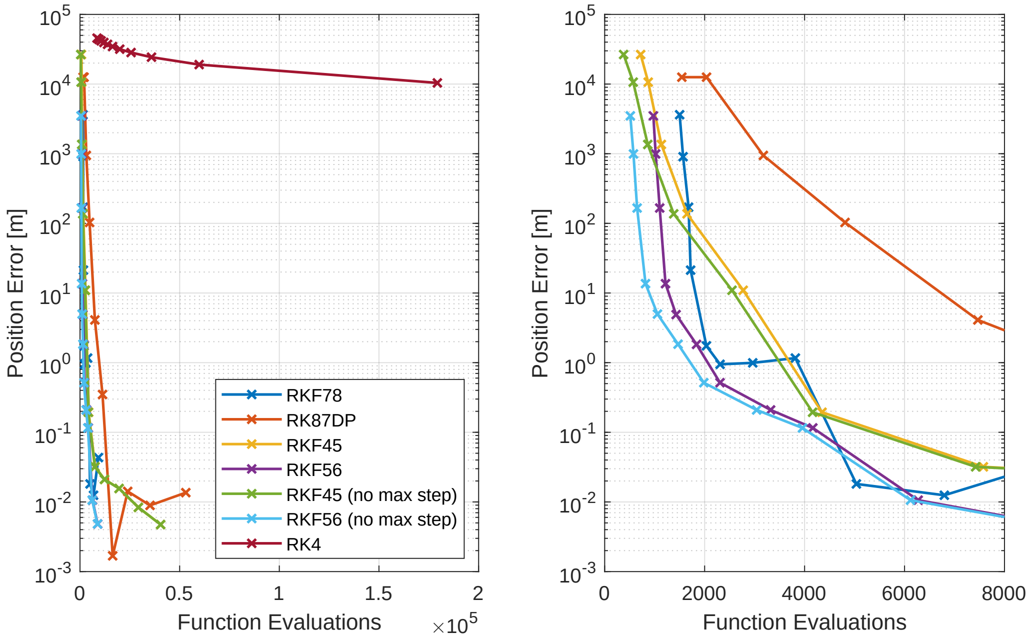

Figure 5.8: Final position error for different numerical integration methods with varying tolerances for all results (left) and a zoom-in on left section (right)

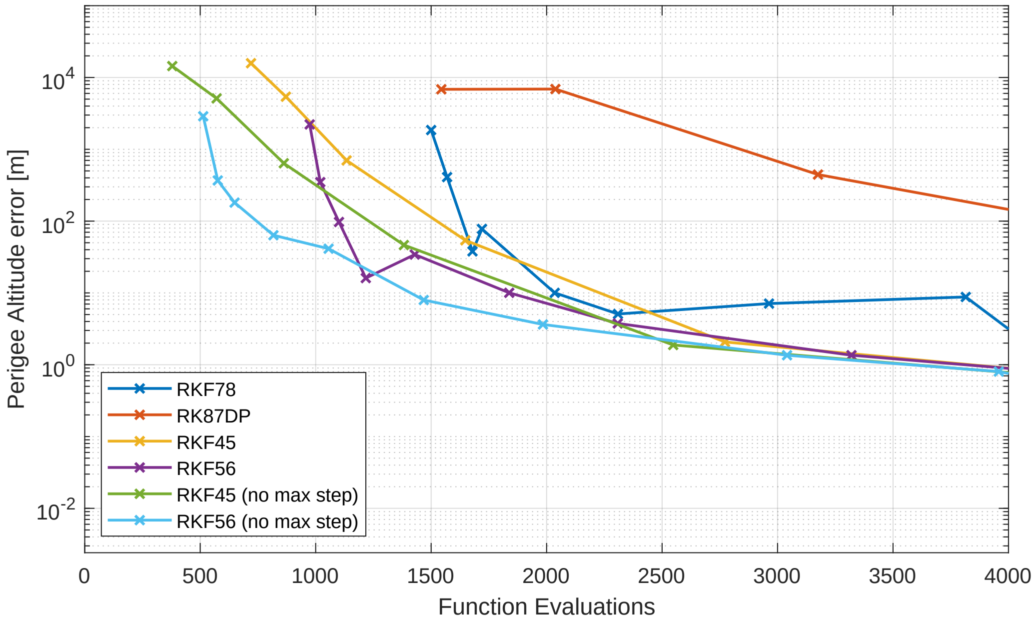

Figure 5.9: Perigee altitude error for different numerical integration methods with varying tolerances

The left graph of Figure 5.8 shows the full range of errors and function evaluations of all methods. The right graph shows a more detailed view of the most relevant part of the graph. The variable step integrators have been evaluated from a relative and absolute tolerance of 10^{-4} to 10^{-14}. The data points are marked with a small x. The most left data points of each method, which have the smallest number of function evaluations, are results from

a tolerance of 10^{-4}. Every next cross to the right is a data point with a tolerance 10 times smaller. The variable step methods have a maximum step size of 5 seconds unless stated otherwise. For the RK4 method applies that the most right data point has a step size of 0.01 seconds, increase with 0.02 seconds for every data point to the left. It is clear from the left graph from Figure 5.8 that the RK4 method is outperformed by every other method in terms of accuracy and computational effort and therefore it is omitted from consideration. The fact that variable step size integrators perform much better is probably due to the fact that the launch vehicles in the MDO will have relatively large coasting times during which relatively large time steps can be taken without increasing the error much. The right graph shows that restricting the maximum step size increases the number of function evaluations, but does barely anything for the accuracy. The best method seems to the the RK56 with no maximum step size with tolerances of 10^{-7}. It has a final position error of just over 13.7 m with 817 function evaluations. It is roughly 10 times more accurate than RK56 with 10 times larger tolerances, but with only a small increase in function evaluations.
To confirm that the RKF56 method with tolerances of 10^{-7} is good enough for the MDO, also the error in perigee altitude is evaluated. The perigee altitude is one of the optimization objectives and as shown in Equation 5.38 it encompasses the eccentricity and semi-major axis. The reference trajectory leads to a benchmark orbit with an semi-major axis of 6713210.8 meter and 0.01427 eccentricity. This gives a perigee altitude of 245.332 km. The perigee altitude error can be seen in Figure 5.9. The RKF56 method with tolerances of 10^{-7} has a perigee altitude error of 63.6 meter. This is not expected to cause any difference in results from higher accuracy methods. Therefore, RKF56 with tolerances of 10^{-7} is chosen as the integrator for the MDO.

5.7. Trajectory Model Validation

To see how well the trajectory model can represent reality, it is validated. For the validation use is made of the VEGA launch vehicle. The VEGA is a 4-stage launch vehicle of which the first 3 stages have solid propellant and the upper stage has liquid propellant. Information from the VEGA launch vehicle will be taken from its User's Manual and official ESA sources [93, 94].
VEGA has four rocket motors, the P80, Z23, Z9 and the MEA, a liquid propellant stage which is an evolution of the RD-869. The characteristics is these motors used to model the VEGA are shown below:

Table 5.3: Characteristics of the VEGA model used for trajectory validation

	Stage 1 : P80	**Stage 2: Z23**	**Stage 3: Z9**	**Stage 4: MEA**
Propellant Mass [kg]	87710	23814	10567	577
Inert Mass [kg]	8533	2486	1433	688
Specific Impulse (Vac) [s]	280	287.5	295.9	314.6
Burn Time [s]	109.9	77.1	119.6	612.5
Length [m]	11.2	8.39	4.12	2.04
Chamber Pressure [bar]	95	95	67	-

The thrust will be modeled as constant as in the MDO. The values are valid for performance in a vacuum. Therefore, for the lower stages they must be corrected for flight in

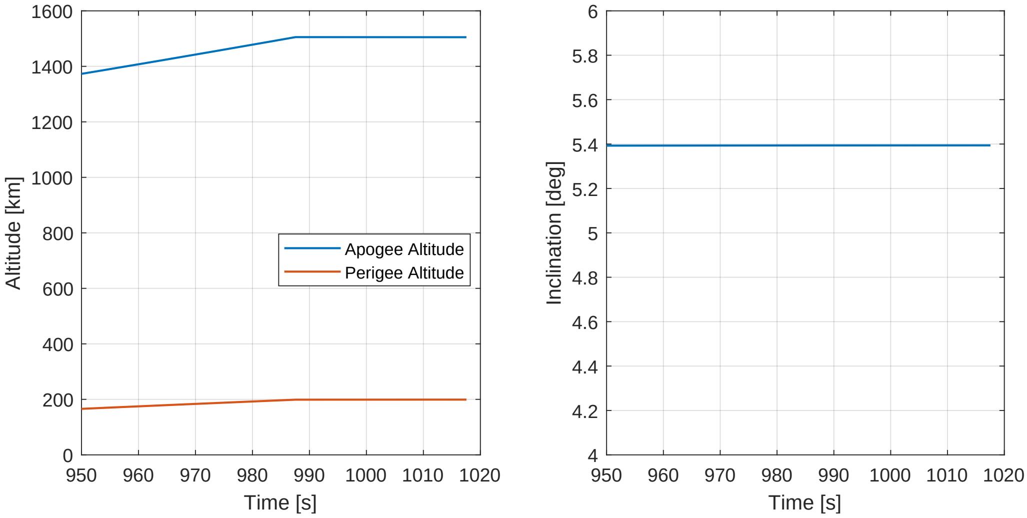

Figure 5.10: Apogee altitude, perigee altitude and inclination at the final times of the ascent of validation run

the lower atmosphere. To calculate the thrust with Equation 3.1, the nozzle exit area is required. The nozzle exit area can be easily determined with the expansion ratio and throat area with Equation 3.5. The expansion ratios of the motors are 16, 25 and 56 for the P80, Z23 and Z9, respectively. In the same order they have throat areas of 0.193, 0.068 and 0.021 m^2 [94]. This results in nozzle exit areas of 3.092, 1.697 and 1.183 m^2. The burn time of the liquid propelled upper stage is reported to be up to 612.5 s. In this model the full 612.5 seconds are used as burn time.

VEGA has a payload fairing mass of 540 kg, which is jettisoned around 231 seconds into the flight. It has a diameter of 2.6 m and a length of 7.88 m. The fairing jettison is included in the simulation. It can feature two different payload adapters, with masses of 77 and 78 kg. It is chosen to use the 78 kg adapter for validation.

The model of the VEGA will be used to simulate a typical elliptical orbit mission. For the typical elliptical orbit mission the launch vehicle will transport a payload of 1963 kg, including the payload adapter, to an elliptical orbit with an apogee altitude of 1500 km, perigee altitude of 200 km and an inclination of 5.4 degrees [93]. The launch site is the Guyana Space Centre. This location has a latitude angle of 5.236 degrees and a longitude angle of -52.775 degrees.

An optimization is run with only the guidance variables as optimization variables. The MOEAD algorithm is used. Orbits are accepted when the error in apogee altitude is smaller than 5 km and the error in perigee altitude is smaller than 2 km. The population consists of 100 individuals which run for 100 generations.

The results are shown in Figure 5.10 and Figure 5.11. Already at generation 16 good orbits were found. Figure 5.10 shows that the apogee and perigee altitudes are equal to the reported values. Also the inclination has the correct value. To be exact the apogee altitude is at 1504 km, perigee altitude at 199 km and the inclination is 5.394 degrees. In Figure 5.11 can be seen that the airspeed in the model approaches the airspeed of the real vehicle well. The real data has been retrieved from a figure in the User's Manual [93]. In reality the vehicle accelerates more quickly, which is caused by the fact that the P80 motor has a grain configuration of a Monolithic Finoxil aft star, which has a regressive thrust profile [94, 95].

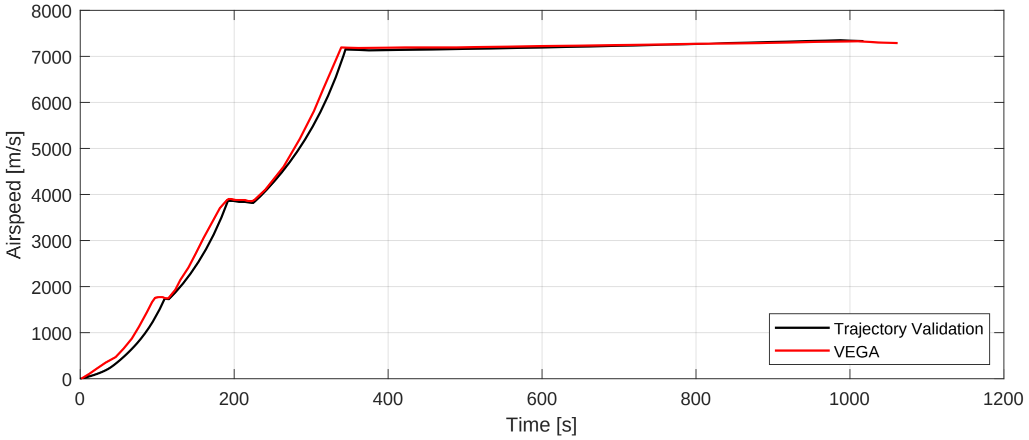

Figure 5.11: Airspeed of model and VEGA data for typical elliptical orbit mission

That means that in reality a higher thrust occurs at the beginning of the burn than calculated with the constant thrust model. It can be seen, though, that the total acceleration of each stage comes very close to the real values. The VEGA action time is slightly longer. The reason for this is that the upper stage of the VEGA for the elliptical orbit mission burned approximately 640 seconds, even though the maximum burn time is stated to be 612.5 seconds.

In conclusion, the model is able to successfully bring the model of the VEGA to the required orbit. Therefore, the model is deemed adequate to use in the MDO.

6

Results

In this chapter the results of the MDO will be shown and discussed. First, the design space and other relevant settings are explained. Then the results of the MDO will be discussed for different situations.

6.1. Design Space and Settings

If all design variables from the disciplines are added, the total number of design variables is 15. For each design variable the search boundaries must be defined. Boundaries are chosen based on limitations in the model or preliminary testing. Where possible, the design space was reduced to facilitate faster optimization. Below, the design variables are given with their design space. Where applicable, it will be explained per design variable how the design space was determined. If no further explanation is given, it means that it was determined by estimation and testing.

1. Length of cylindrical motor case section (L_c). Design space: 0.2 to 0.5 m.
2. Maximum radius of the grain (R_g). Design space: 0.13 to 0.265 m. The upper boundary is based on the diameter of the SM-3 stages.
3. Length of the elliptical case top (L_e). Design space: 0.06 to 0.20 m.
4. Chamber pressure (p_c). Design space: 30 to 50 bar. The lower boundary is based on the deflagration limit of ammonium-perchlorate in the propellant and the STAR motors. First of all, the deflagration limit occurs around 20 bar [48, 96, 97]. However, the lowest average pressures in the STAR motors using TPH-3340 as propellant are around 35 bar. Therefore, it is chosen to not approach the deflagration limit too closely and use 30 bar as a minimum.
5. Exit pressure (p_e). Design space: 0.02 to 0.15 bar.
6. Payload mass (M_u). Design space: 6.0 to 20.0 kg. This can vary slightly to accommodate specific situations. For the reference equatorial orbit, however, this design space is used.
7. Linear pitch angle decrease ($\Delta\theta_\mathrm{po}$). Design space: 10.0 to 25.0 degrees.

8. Linear pitch angle decrease time (t_{po}). Design space: 1.0 to 5.0 seconds. Testing showed that the time often converged to the minimum value. Lowering the lower boundary more could generate unrealistically high pitch rates. A rocket from Copenhagen Suborbitals with a length of 9.38 meters was found to reach a pitch rate of over 20 degrees/s quickly after clearing its launch tower [98]. With a maximum boundary of 25 degrees of $\Delta\theta_{\text{po}}$, the minimum boundary for t_{po} is set at 1 second.
9. Coasting time after third stage burn-out (t_{coast}). Design space: 50.0 to 450.0 seconds.
10. Pitch angle change 1 ($\Delta\theta_1$). Design space: -30.0 to -5.0 degrees.
11. Pitch angle change 2 ($\Delta\theta_2$). Design space: -30.0 to -5.0 degrees.
12. Pitch angle change 3 ($\Delta\theta_3$). Design space: -20.0 to 5.0 degrees.
13. Pitch angle change 4 ($\Delta\theta_4$). Design space: -15.0 to 10.0 degrees.
14. Final pitch angle after bi-linear tangent law (θ_{f}). Design space: -10.0 to 10.0 degrees.
15. Bi-linear tangent law exponent (ξ). Design space: -1.0 to 1.0.

If during the generations of the results it is found that a design variable converges to its boundaries, it will be evaluated if the boundary can be expanded. If expansion is possible, the optimization will be rerun.

Also, a population size and number of generations must be determined. Not much is found on optimal population sizes for global optimization. In most cases, a population size 10 times the amount of design variables is recommended [99]. Therefore, in this case 150 individuals are generated for the population. The individuals will evolve over 1000 generations. Each simulation is run with three different seeds.

Lastly, a flow chart is made of the architecture of the MDO tool that is used to generate the results. It can be seen in Figure 6.1. It is a top-level summary of the workings of the MDO tool that were explained in more detail in the earlier chapters.

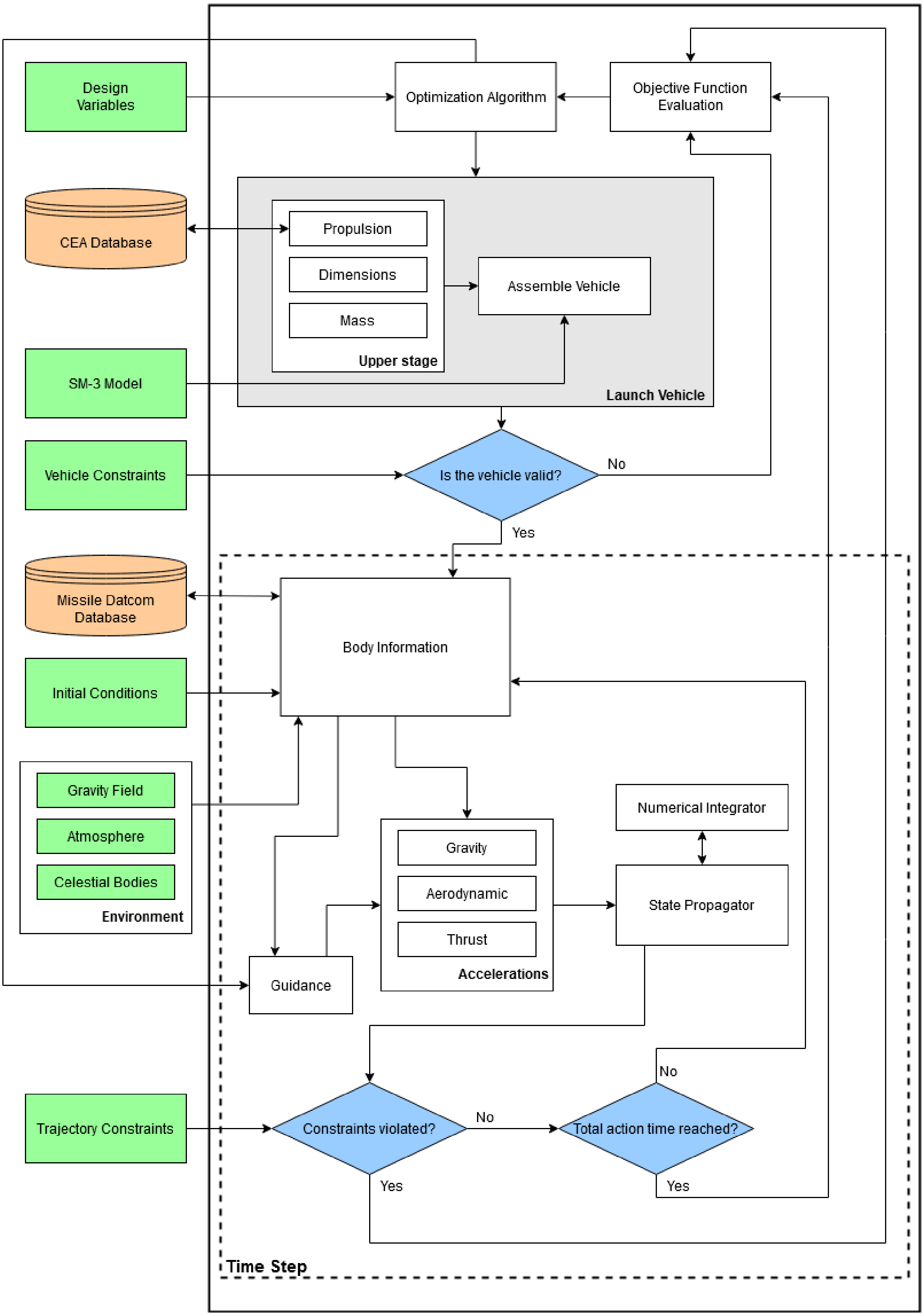

Figure 6.1: Flow chart of the MDO tool

6.2. Maximum Payload

It is not known in advance which exact orbits the launch vehicle will launch to. So firstly, an equatorial orbit is analysed. When launching from the Earth's surface, launching from the equator to an equatorial orbit requires the least amount energy and therefore the maximum payload mass per perigee altitude will be found here. The results of the simulations for all seeds is given in Figure 6.2.

To confirm that the chosen integrator is adequate, also the Pareto front of the combined solutions of all seeds of the nominal case is compared with the Pareto front of all seeds of a case with a more accurate numerical integrator. For the more accurate method a RKF56 with tolerances of 10^{-10} is used. The final position error of this integrator is around 20 times smaller than the nominal RKF56 with tolerances of 10^{-7} as can be seen in Figure 5.8.

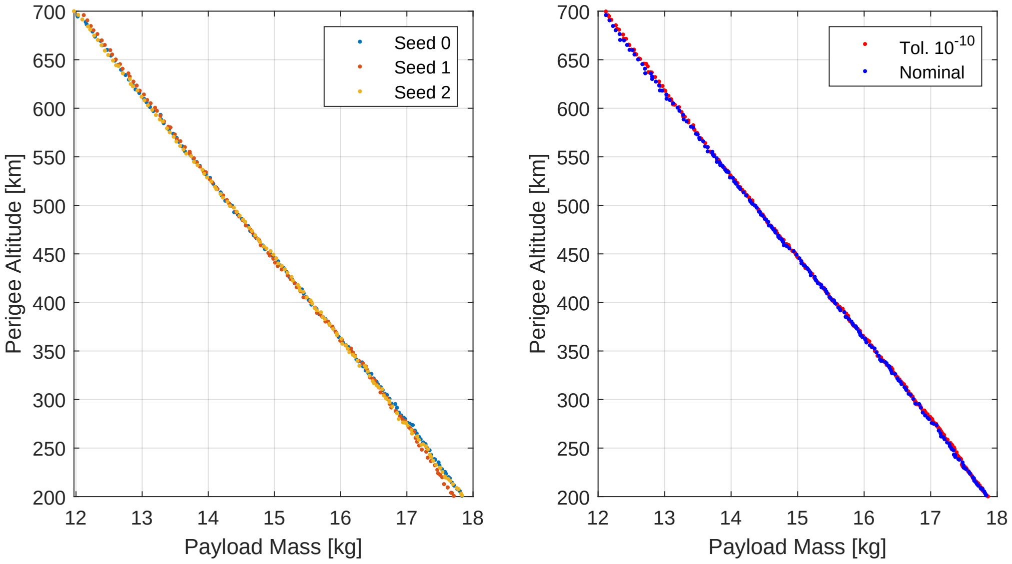

Figure 6.2: Perigee altitude vs payload mass for equatorial orbit for all seeds

It can be seen in Figure 6.2 that each seeds produced similar optimal results with only seed 2 giving slightly worse results for the lower orbital altitudes. This provides confidence that the solutions found are likely close to the real optimum. The fact that the Pareto front of the runs with a more accurate integrator has no significant differences with the Pareto front of the nominal case suggests that using the RKF56 integrator with tolerances of 10^{-7} works well. The graphs show a seemingly linear relation between maximum payload mass and perigee altitude, which is also seen in other launch vehicles for similar orbital altitudes such as Electron and Pegasus XL [88, 100]. The payload capacity decreases with ~32% from 200 km to 700 km perigee altitude from 17.8 kg to 12.1 kg.

The Pareto front from the combined solutions of all seeds consists of 225 individuals. In Figure 6.3 it can be seen how well the orbits have been optimized for maximum payload capacity. It shows the eccentricity and inclination of the orbit at the end of the burn vs the perigee altitude for each Pareto individual. Figure 6.3 shows that the orbits are virtually on the equatorial plane. The orbits are also almost circular, which was expected to optimize the payload capacity. It was easier for the optimization to reduce the eccentricity for lower orbital altitudes. A few individuals at the upper half section of the perigee altitudes have a

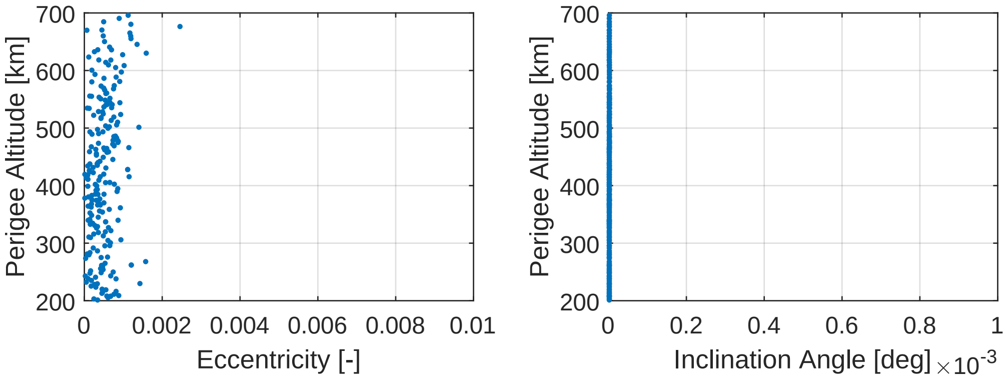

Figure 6.3: Perigee altitude vs orbital parameters of the Pareto front

slightly higher eccentricity. However, the highest value lies just above 0.002, which still is close to a circular orbit.

In Figure 6.4 the Pareto individual values of the design variables of the upper stage motor and the coasting time are given per perigee altitude. The cylindrical motor length is not widely distributed over the range of perigee altitudes. It fluctuates around 0.33 m for lower orbits and slightly decreases its average at higher orbital altitudes. The maximum grain radius shows a clear trend, but with discontinuities. This is caused by the fact that a database is used for the aerodynamic coefficients. The coefficients are taken from the database with the diameter that is closest to the the diameter of the individual. The database has steps of 0.5 cm in upper stage diameter, so 0.25 cm in radius. The optimization searches for the maximum diameter that does not invoke the next set of coefficients. For example, the diameter for a group of individuals will converge towards 33.25 cm, but not reach 33.25, increasing the propellant mass as much as possible while still using the coefficients of a diameter of 33 cm. A diameter of 33.25 would invoke the aerodynamic coefficients for a diameter of 33.5 cm, which would give a higher drag coefficient.

The chamber pressure converges to its lower boundary. This is caused by multiple mechanisms. First of all, a lower pressure means that the mass flow is smaller, which in turn requires a smaller throat area, according to Equation 3.3 and Equation 3.7, respectively. When the throat area is smaller, a higher expansion ratio can be realized without the need for a long nozzle. A high expansion ratio is beneficial for the performance of the propulsion system. Also, the shorter nozzle leaves more room for propellant, which combined with a smaller structural mass gives a higher propellant mass fraction. The low chamber pressures suggest that the performance might increase if the boundary was decreased to the deflagration limit. This will be investigated in a sensitivity analysis in section 7.6. Also a propellant with a lower burn rate exponent could increase performance, so the burn characteristics of the propellant will also be analysed in a sensitivity analysis.

The exit pressure decreases as the orbit altitude increases. This means that, with the chamber pressure being almost constant around 30 bar, for lower orbits the expansion ratio will be lower and therefore it is expected that also the specific impulse is lower. This can also be seen in Figure 6.5. The specific impulse has a similar trend to the exit pressure as expected. From Figure 6.5 it seems that for lower orbits, a higher vacuum thrust is beneficial. For a higher thrust a larger throat area is required and consequently no room is left for a nozzle that expands the flow as much as for higher orbits. The highest specific impulse value is

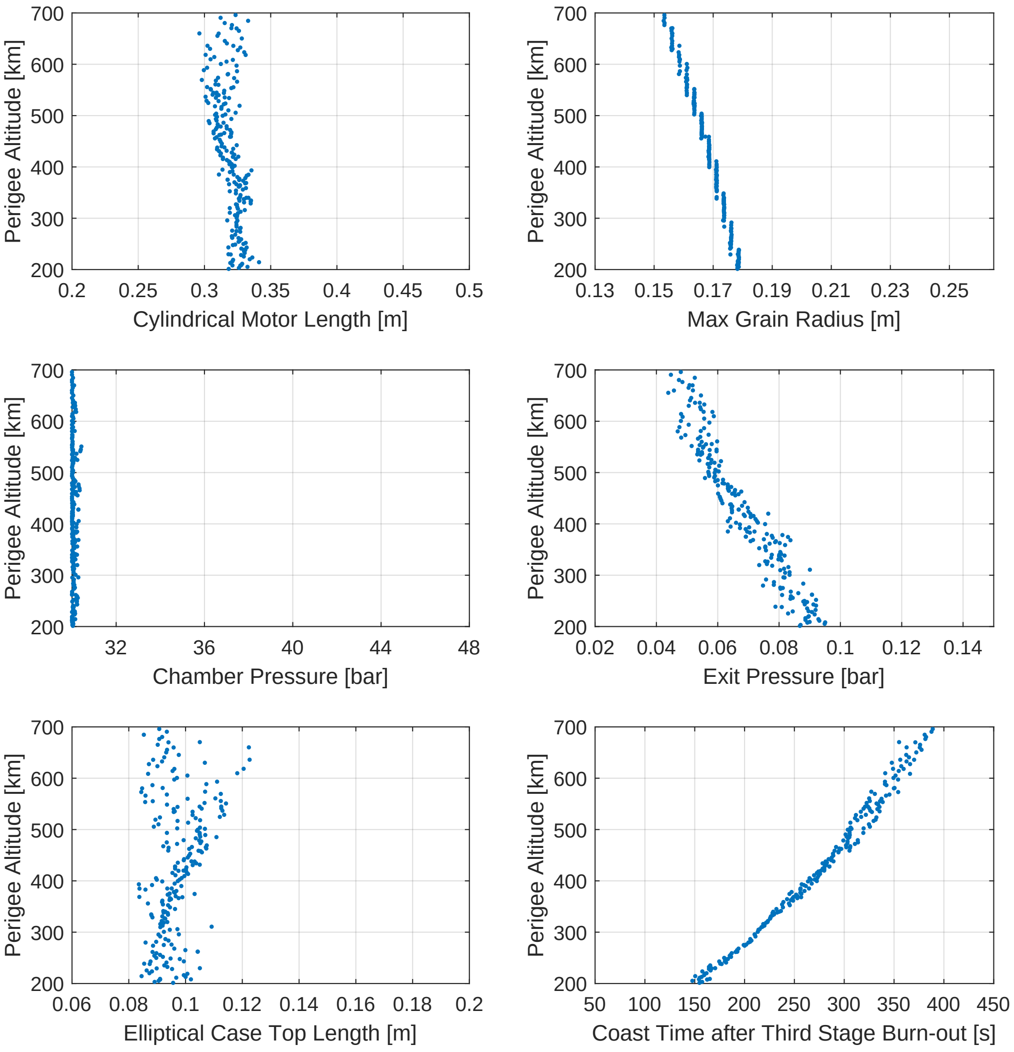

Figure 6.4: Perigee altitude vs SRM design variables and coasting time

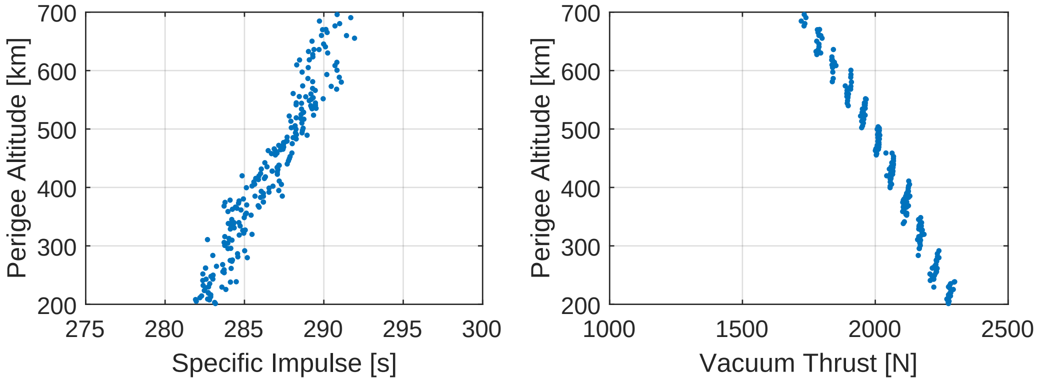

Figure 6.5: Perigee altitude vs SRM performance parameters

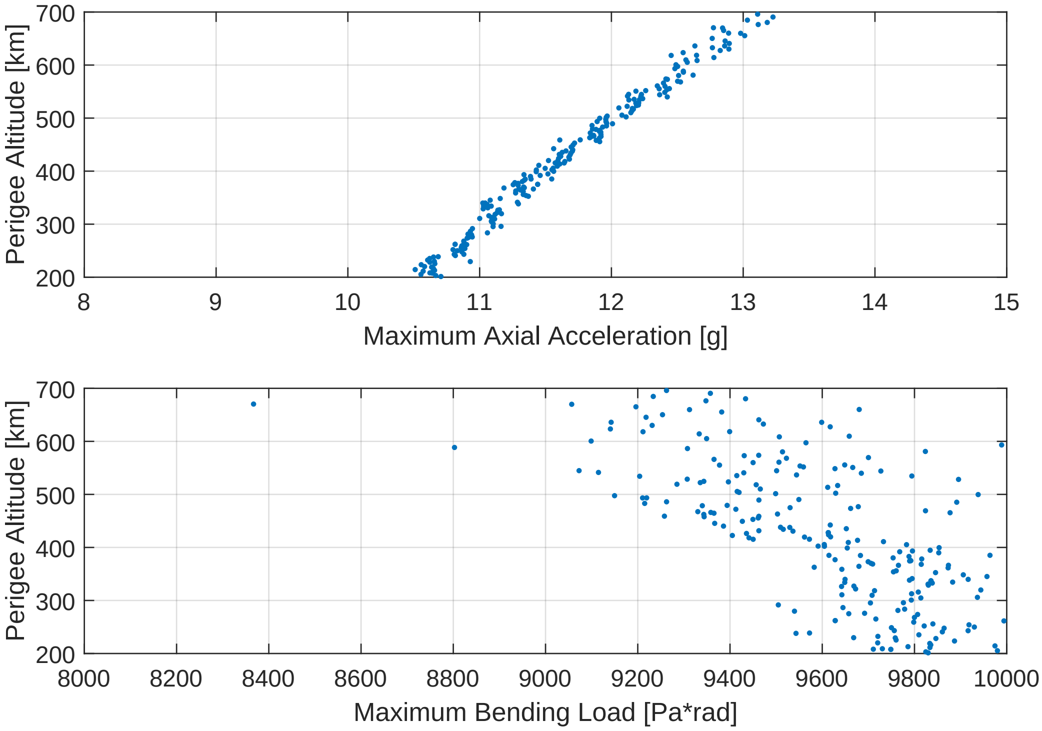

Figure 6.6: Path constraint values per perigee altitude for Pareto individuals

291.9 s at an expansion ratio of 69.5, which is close to the specific impulse values of STAR series motors with similar expansion ratios [46].

In Figure 6.4 also the trend of the elliptical case top length and the coasting times versus the perigee altitude can be seen. No clear relation between the case top length and the perigee altitude can be observed. The values are distributed between 0.08 and 0.12 m. Looking at the radii of the motor and the elliptical top lengths, it shows that an elliptical top is more optimal than a spherical top.

The trend in coasting time after the third stage burn-out is as expected, becoming larger with increasing orbital altitudes. With the constant and short burn time of the first three stages, more time is needed to reach higher altitudes.

The values of the path constraints are shown in Figure 6.6 for all Pareto individuals. The highest axial accelerations are 2 g's away from violating the constraint value of 15 g. The maximum accelerations in the graph do not occur during the upper stage burn, but at burn-out of the third stage. The maximum bending load approaches its boundary value of 10000 Pa·rad for lower orbits. For higher perigee altitudes the values are spread out more and on average have lower values. This makes sense, as to reach lower orbits the pitch angle reduces more quickly, causing larger absolute angles of attack to occur. For higher orbits the values are not as close to violating the constraint, but are still close for some individuals. Implementing a higher constraint value for the maximum bending load could increase performance and might be possible as discussed in subsection 5.5.3. This will be analyzed in a sensitivity analysis. However, the fact that most maximum bending load values do not approach the constraint value too closely even for lower orbits suggests that the solution is not sensitive to this parameter.

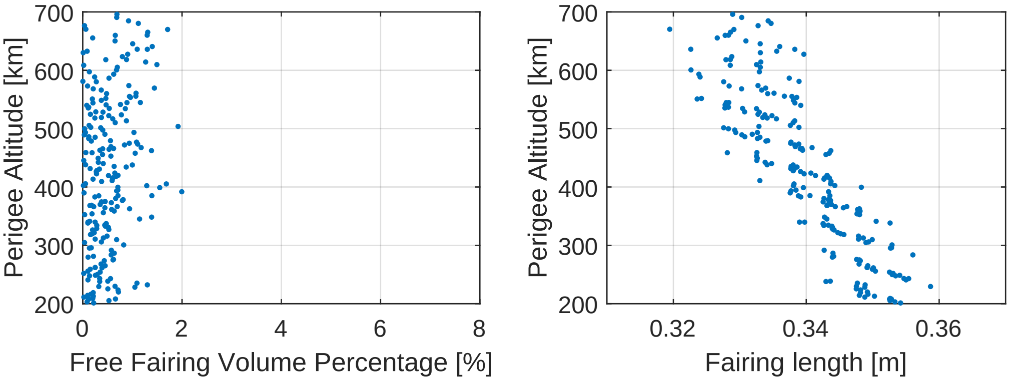

Figure 6.7: Free fairing volume per perigee altitude for Pareto individuals

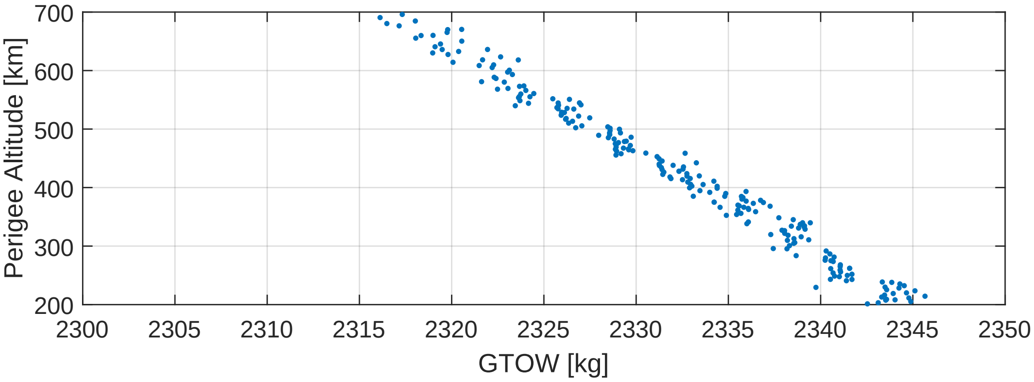

Figure 6.8: GTOW per perigee altitude for Pareto individuals

Another constraint was the volume of the fairing. The fairing must be at least as large as the required volume for the payload calculated with Equation 4.2. The required volume differs for each individual, so to visualize this constraint the free volume ratio is plotted for each Pareto individual. The free volume ratio is the fairing volume that is not occupied by the required volume divided by the total fairing volume. Figure 6.7 shows that over the whole range, the required volume for the payload is at least almost 98% of the total fairing volume. This suggests that the estimated factor of 1.5 from Equation 4.2 can be a limiting factor. Therefore, it is interesting to analyze this parameter in a sensitivity analysis.

The payload mass decreases more over the range of perigee altitudes than the square of the grain radius. The free fairing volume remaining small over the whole range suggests that the fairing length decreases as the perigee altitude increases. This is confirmed in Figure 6.7.

Also, it is interesting to see what the effect is on the total mass of the vehicle. A change in the total mass, while using the same boost motor can result in a different fly-out from the VLS. However, Figure 6.8 shows that values of the the gross takeoff weight is of similar magnitude than the values the SM-3 model that is used. For higher orbital altitudes the optimized vehicle is only a few kilograms heavier than de 2312 kg SM-3 reference model. Even for the lower orbital altitudes the difference is no larger than 1.5%.

Lastly, it is interesting to look at the trajectory of some of the individuals. The pitch profiles, flight path angles and altitude vs down range distance values of three individuals are plotted in Figure 6.9. To see the difference between different perigee altitudes, one individual is chosen from the top of the range of perigee altitudes, one from the bottom and one in the middle. Clearly, to reach lower perigee altitudes, the pitch angle decreases more earlier in the flight. The lower perigee altitudes are also reached earlier with a smaller downrange distance travelled.

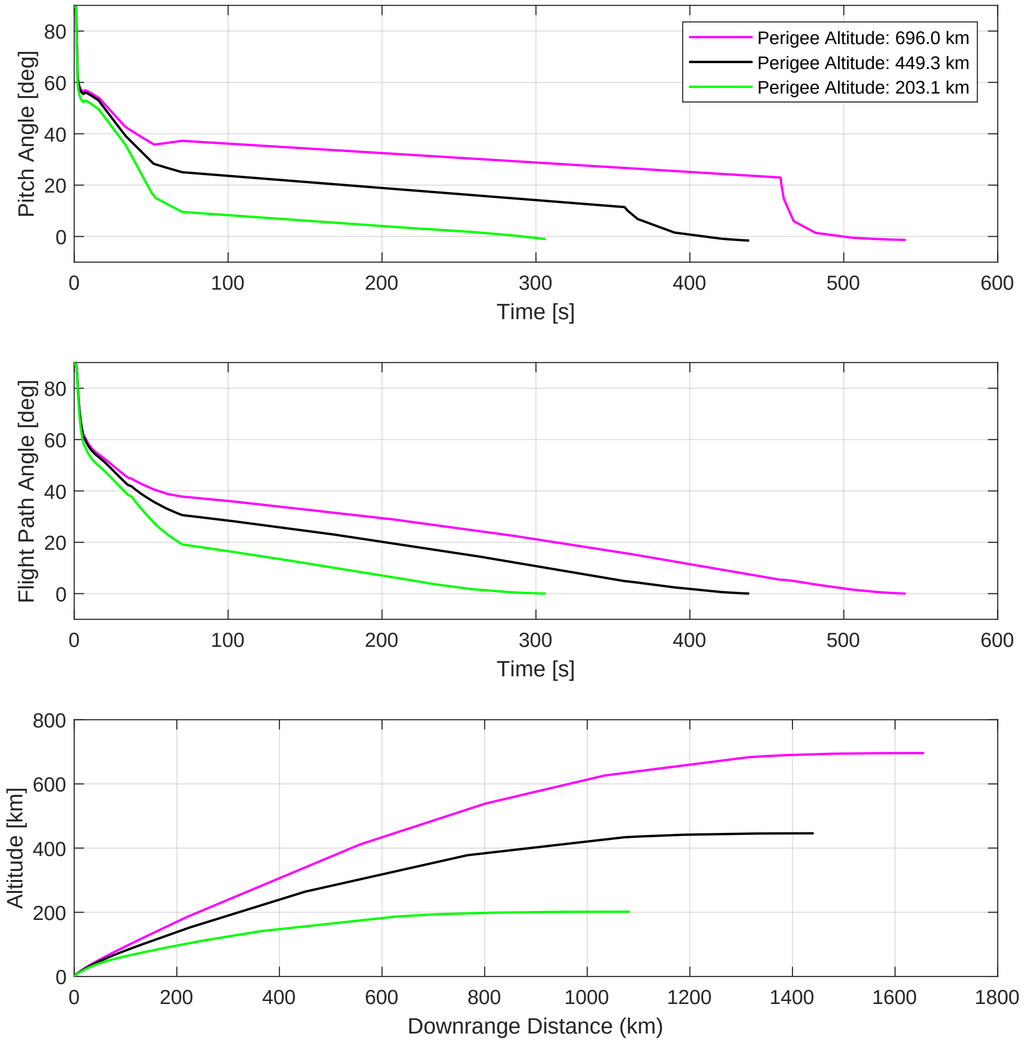

Figure 6.9: Pitch profiles, flight path angles and altitude vs down range distance values for three Pareto individuals

Comparing the relative velocity of the three individuals shows that the lower mass of the individual with the highest perigee altitude leads to a larger relative velocity at burn-out of the third stage as seen in Figure 6.10. Starting at roughly 464 m/s, which is the relative velocity the vehicle has at the equator in an Earth-centered inertial reference frame, the vehicle is accelerated to its orbital velocity. The required orbital velocity reduces slightly with increased perigee altitude, as expected. The coasting times start below an altitude of 100 km for all individuals. To be exact, at 95 km for the individual with the highest perigee

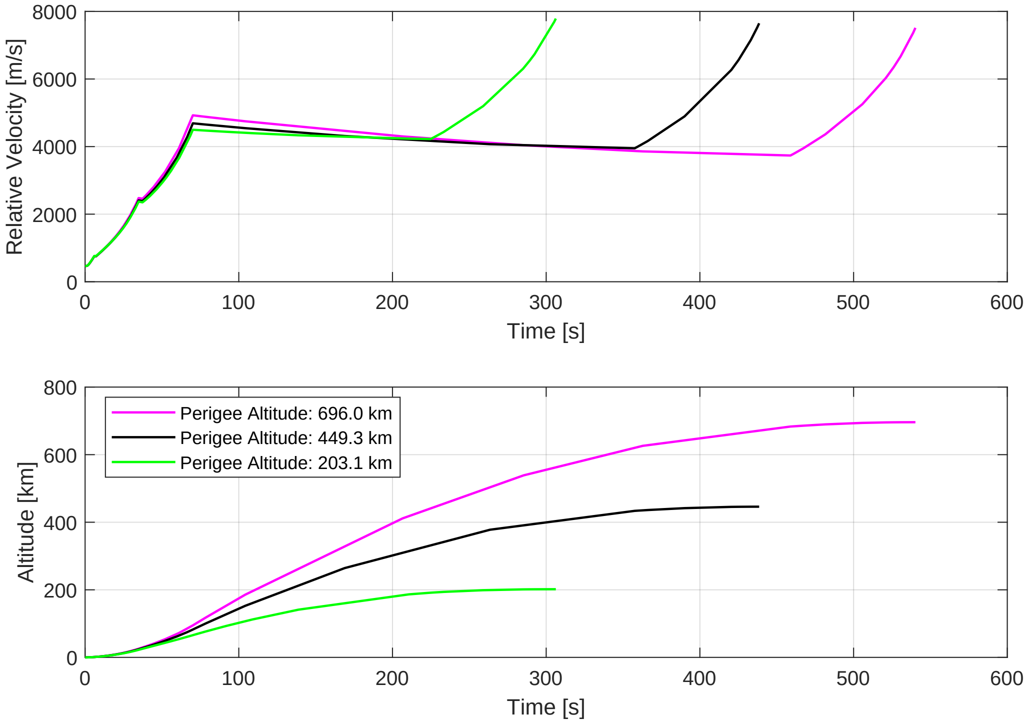

Figure 6.10: Relative velocity and altitude vs time for three Pareto individuals

altitude and at 66 km for the individual with the lowest perigee altitude.
From the results in this section can be seen that it is possible to launch a microsatellite to an equatorial orbit. The maximum payload is 17.8 kg at 200 km perigee altitude and still 12.1 kg can be launched to a perigee altitude of 700 km. It must be noted that the payload mass includes also the mass of the payload adapter and the avionics. So if the adapter and avionics mass can remain below 2.1 kg, for an equatorial orbit a microsatellite can be launched over the whole evaluated range of perigee altitudes. If not, then the range of perigee altitude to which a payload of at least 10 kg can be launched is smaller.

6.3. Different Launch Locations and Inclinations

As mentioned earlier, the orbits that the launch vehicle will be used to launch to are not known in advance. Therefore, it is important to see how it performs for other orbits than an equatorial one and how the optimal design changes. In this section two different target orbits will be evaluated.

First of all, the launch location is different. As the launch vehicle is launched from a ship, the launch site is flexible. For the sake of choosing a fixed location, the launch location will be the main base of the Royal Netherlands Navy in Den Helder. This location has a latitude angle of 52.958 degrees and a longitude angle of 4.786 degrees. Firstly, the launch vehicle will be launched with a heading angle of 90 degrees, which results in an orbit with 58 degrees inclination. Additionally, also the performance for a polar orbit will be evaluated.

The payload mass per perigee altitude Pareto fronts are given for both cases in Figure 6.11.

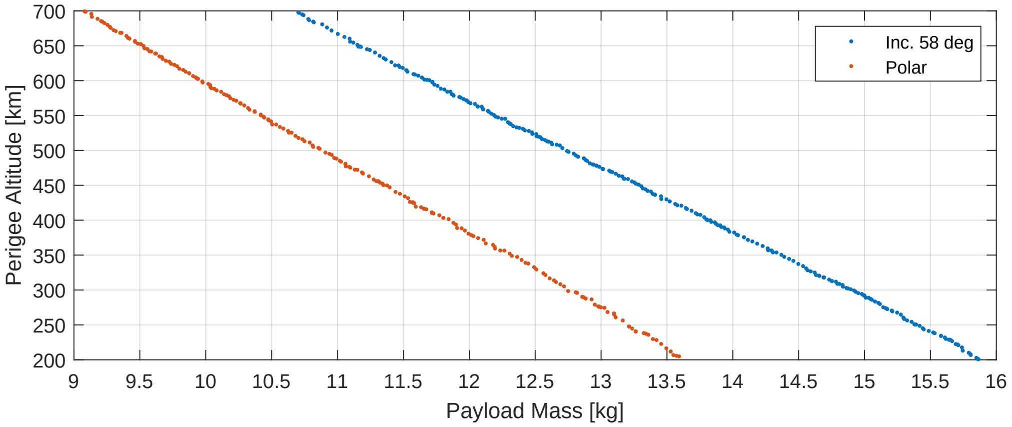

Figure 6.11: Perigee altitude vs payload mass Pareto fronts of launch from Den Helder for different orbits

For both cases the payload masses are lower than for the equatorial orbit at the same perigee altitudes, as expected. Again, a linear trend is observed. For higher orbital altitudes the payload capacity for a polar orbit is below 10 kg. That means that it is not possible to launch a microsatellite to higher orbital altitudes, also keeping in mind that the payload mass also contains the mass of the payload adapter and avionics.

In further graphs in this section, the same colouring is used to differentiate between the two different orbital inclinations, so red for the polar orbit and blue for the 58 degree inclination orbit. Figure 6.12 shows that the eccentricities of the orbits are close to 0 and shows the final inclination angles after burn-out of the last stage.

The design variables of the upper stage motor are analysed to evaluate differences with the equatorial orbits. The design variables are shown in Figure 6.13. The trends for the cylindrical motor length show that the values are slightly higher than for the equatorial orbit, with the polar orbit having the highest values. The radius of the grain, however, has decreased for both launches from Den Helder. The trend is the same for all orbits, decreasing in steps as the perigee altitude increases. Again, the chamber pressures values converge to the minimum value.

Exit pressures are lower than for the equatorial orbit and the values for the polar orbits are also lower than for the 58 degree inclination orbit. That means that for a certain perigee altitude, the expansion ratio of the upper stage motor is highest for the polar orbit. The

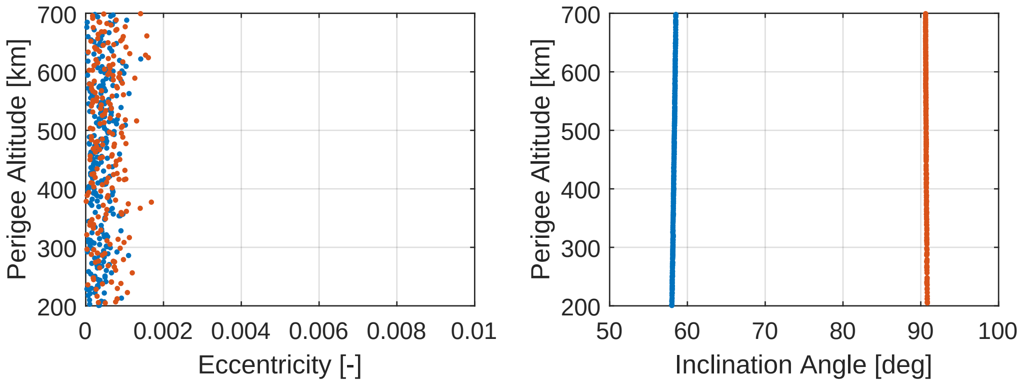

Figure 6.12: Perigee altitude vs orbital parameters of the Pareto fronts (colouring in accordance with Figure 6.11)

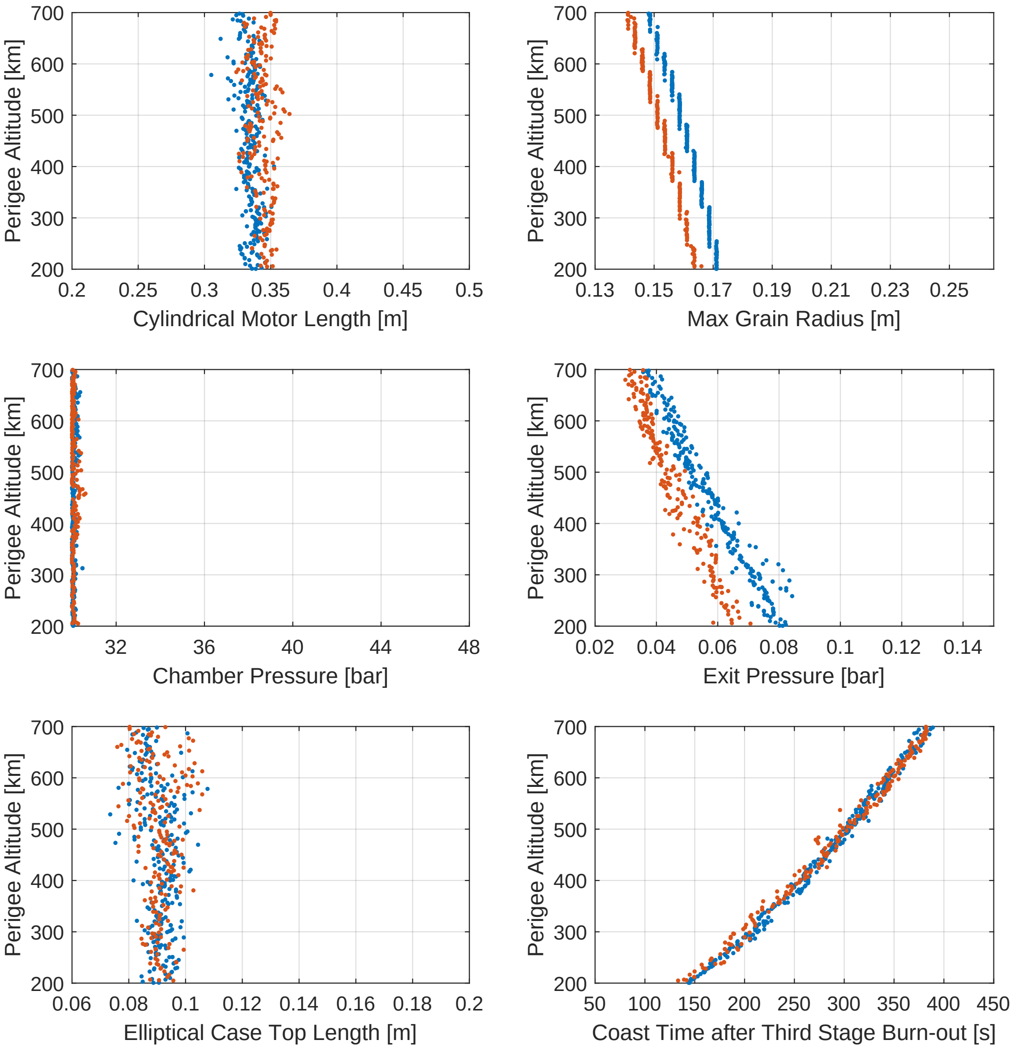

Figure 6.13: Perigee altitude vs SRM design variables and coasting time (colouring in accordance with Figure 6.11)

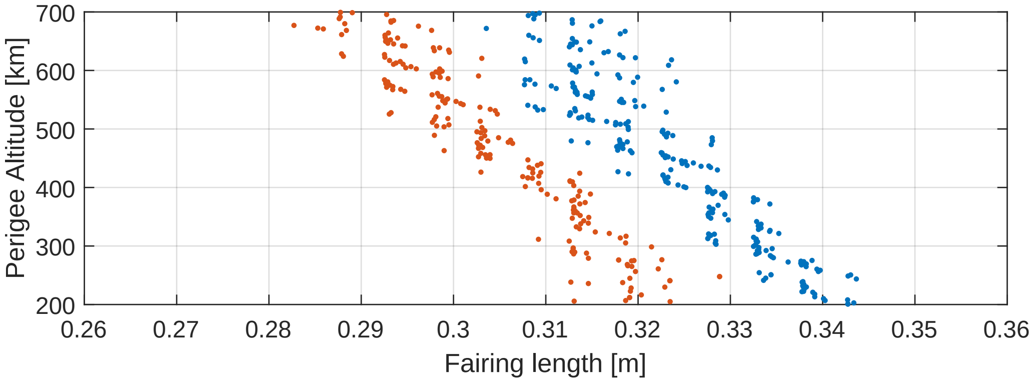

Figure 6.14: Fairing length per perigee altitude for Pareto individuals (colouring in accordance with Figure 6.11)

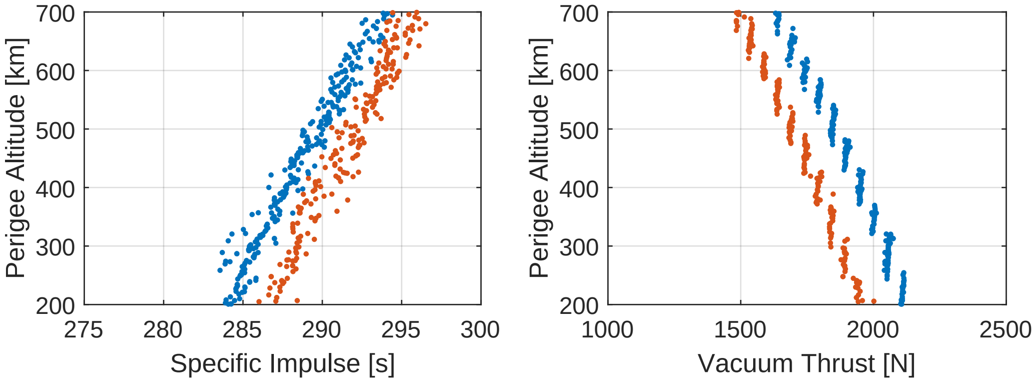

Figure 6.15: Perigee altitude vs SRM performance parameters (colouring in accordance with Figure 6.11)

reason for this can be explained with the vacuum thrust and the fairing length, radius and required volume. Especially for the polar orbits lower payload masses are achieved. A lower payload mass requires a smaller fairing volume. A lower volume means that the fairing radius and length can decrease. Figure 6.13 shows that the radius of the upper stage, which is the same as the radius for the fairing, decreases. Also, the fairing length decreases with the decrease of the payload. This is shown in Figure 6.14. A smaller grain radius at the same chamber pressure results in a smaller mass flow from the grain and therefore also a smaller thrust, as seen in Figure 6.15. The smaller mass flow means that the throat area is smaller as well. The extra length available because of the shorter fairing is canceled out by the larger cylindrical motor length. However, because of the smaller throat area it is possible to achieve a higher expansion ratio with a shorter nozzle length.

The payload mass is a significant part of the total mass of the upper rocket section. With the decrease of the payload mass, the axial acceleration therefore increases as can be seen in Figure 6.16. The highest axial acceleration values still occur at burn-out of the third stage. For the polar orbits with high orbital altitudes the values approach the constraint of 15 g the most. The maximum bending load values do not show a significant difference from the equatorial orbit.

The payload masses are lower at the same perigee altitudes compared to the equatorial orbit. The orbit with 58 degrees inclination can still launch payloads of over 10 kg over the

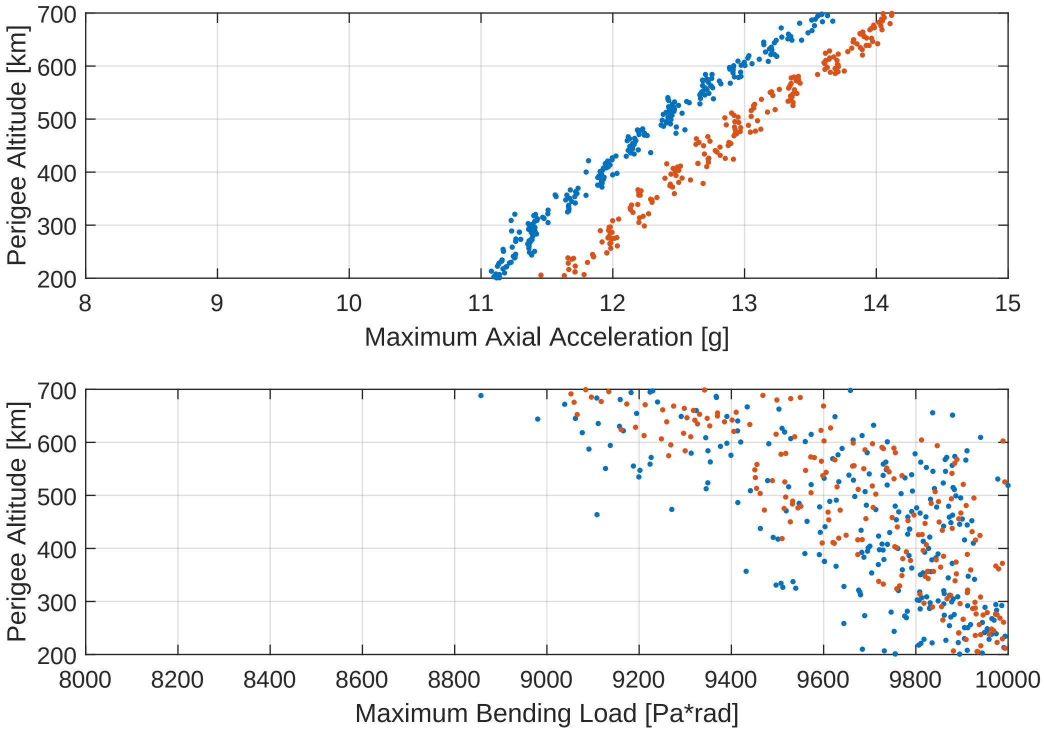

Figure 6.16: Path constraint values per perigee altitude for Pareto individuals (colouring in accordance with Figure 6.11)

whole range of evaluated perigee altitudes. For perigee altitudes above 600 km the payload mass is below 10 kg for the polar orbit. However, for both orbits must be kept in mind that the actual payload mass will be smaller, as the payload adapter and avionics are also included in the determined value.

7

Sensitivity Analysis

To analyze the robustness of the results, sensitivity analyses are performed for multiple parameters. A sensitivity analysis is the process of changing variables or parameters and observing what effect it has on the model or and solution. Eligible for sensitivity analysis are parameters or constraints that are known to have an uncertainty in the values used in the MDO. Also eligible are parameters for which a set design choice was made, but can be varied. For either type of parameters it is interesting what the effect is on the optimal design solution of the launch vehicle. It is not possible to perform a sensitivity analysis on every parameter that satisfy the description above. Therefore a selection is made of the most relevant parameters. For all sensitivity analyses the results for the equatorial orbit will be used as reference.

For sensitivity analysis here, the one-at-a-time method will be used. This method of sensitivity analysis has been encountered in several studies [14, 23, 26]. As the name suggests, one parameter at a time is changed while all others are kept constant. The parameter can be changed by a fixed percentage or a factor of its standard deviation. Ideally, a margin of uncertainty has been determined for each parameter. Unfortunately, this is not always the case.

7.1. Aerodynamic Coefficients

Firstly, the aerodynamic coefficients will be analyzed. As explained in section 4.3, to determine the aerodynamic coefficients, the software Missile DATCOM is used. However, the software has its limitations and it can not be expected that the aerodynamic coefficients are perfectly estimated. Fortunately, validation research has been performed in which Missile DATCOM estimations of the coefficients are compared with wind-tunnel data [70]. In the research the axial and normal coefficients are analyzed for different configurations and flow conditions. The geometry in the MDO has closest resemblance to the body-alone configuration that is used in the research. For this particular configuration no exact numbers are given on the uncertainty in the axial coefficient, but it is concluded that Missile DATCOM can have errors of around 12% for similar configurations. A margin of 12% will therefore be used in the sensitivity analysis of the axial force coefficient. The normal force coefficient is shown to be estimated quite well for the body-alone configuration. No value is given for the error, so here a margin of 3% will be used for the sensitivity analysis.

The results of the sensitivity analysis of the axial coefficient are shown in Figure 7.1. In Fig-

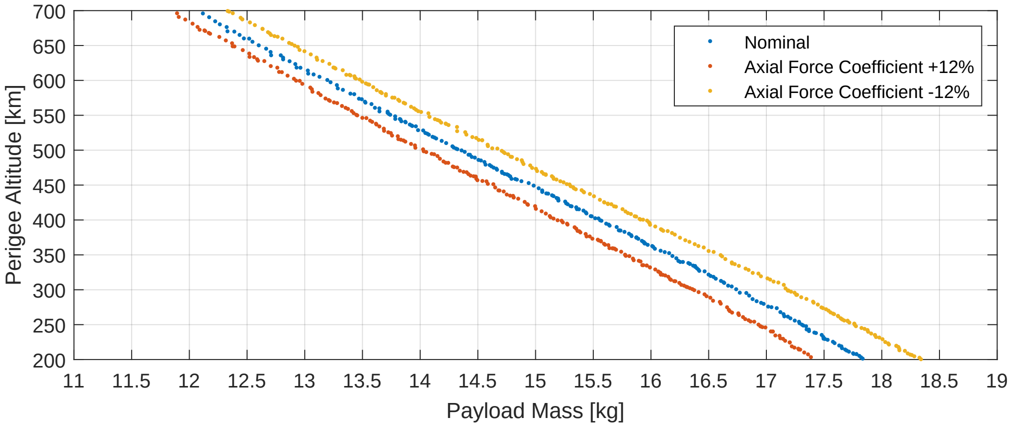

Figure 7.1: Perigee altitude vs payload mass of the Pareto fronts of the axial force coefficient sensitivity analysis and the nominal solution

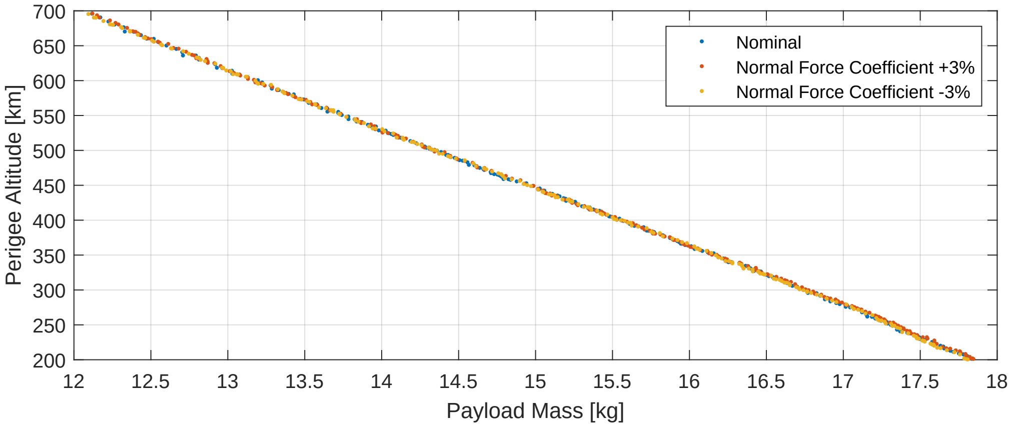

Figure 7.2: Perigee altitude vs payload mass of the Pareto fronts of the normal force coefficient sensitivity analysis and the nominal solution

ure 7.1, the Pareto fronts of the combined solutions of the 3 different seeds are put together. It can be seen that a reduction in the axial coefficient has a positive effect on the payload mass at the same perigee altitude compared to the nominal values. An increase in axial coefficient has the opposite effect. This was expected as the axial force is the main contributor for the drag force for small angles of attack. At the lowest orbits, the difference can be almost 0.5 kg. The difference becomes smaller for higher orbits.
The results for the normal force coefficients are given in Figure 7.2. Clearly, a 3% change in normal force coefficient has a negligible effect on the optimal performance of the launch vehicle.

7.2. Lengths of the Second and Third Stages

Besides the fact that they are manufactured by Mitsubishi Heavy Industries, not much is known about the second and third stage of the SM-3 Block IIA. Estimating their combined length with the values of the SM-3 Block IB motors gives an available length for the upper stage and fairing that closely corresponds with the SM-3 Block IIA kinetic kill vehicle length in Figure 4.3. However, measuring from the image is not perfectly accurate and it is also

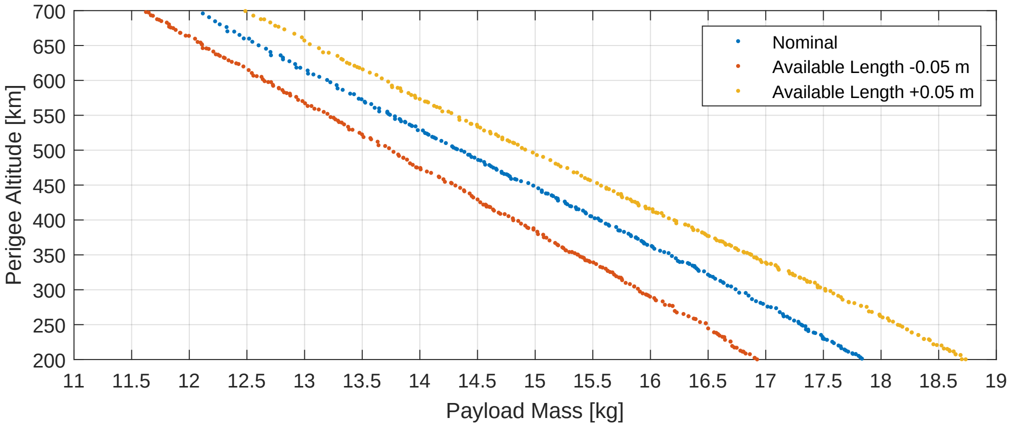

Figure 7.3: Perigee altitude vs payload mass of the Pareto fronts of the available length sensitivity analysis and the nominal solution

not confirmed that only the size of kinetic kill vehicle is a good estimation of the available length. Consequently, uncertainty exists in the value of the available length for the upper stage and fairing. In earlier results it has been observed that the length restriction has a clear effect on the performance of the upper stage. It is therefore expected that varying the available length will have a significant impact on the payload mass in orbit.

The margin or uncertainty is unclear for this parameter. For that reason, a margin of 0.05 m is estimated. The nominal case used an available length for the upper stage and fairing of 0.97 m. The results of the optimization with the different lengths are given in Figure 7.3.

Clearly, a change in available length has a significant effect on the performance of the launch vehicle. At an orbital altitude of 200 km, it makes a difference of approximately 1 kg payload mass compared to the nominal case.

7.3. Required Fairing Volume Factor

For the nominal case, the required fairing volume is determined with Equation 4.2. The factor 1.5 is a rough estimation. In the case of a custom designed payload and payload adapter, this factor might be brought down to approach 1. In another case, when a less favorably dimensioned payload is launched, it might increase. The nominal results show that the required fairing volume can be a restricting factor. For that reason, two optimizations are run, one with a factor of 1.0 and the other with a factor 2.0.

The results of the sensitivity analysis with the required fairing volume factor are shown in Figure 7.4.

As could be expected, the lower factor gives a better performance. Also, the performance reduction from the factor increase to 2.0 is larger than the performance addition from the factor decrease to 1.0.

For a required volume factor of 1.0, the discontinuous trend in the fairing volume suggests that the fairing does not adapt as quickly to a different payload mass and perigee altitude as for the other cases as can be seen in Figure 7.5. Also, the free fairing volume reaches larger values for the factor of 1.0, both in relative and absolute sense. In Figure 7.6 can be seen that the fact that a smaller fairing is required leads to a larger cylindrical motor length and smaller motor radius. Because of the smaller grain radius, a smaller thrust occurs, which

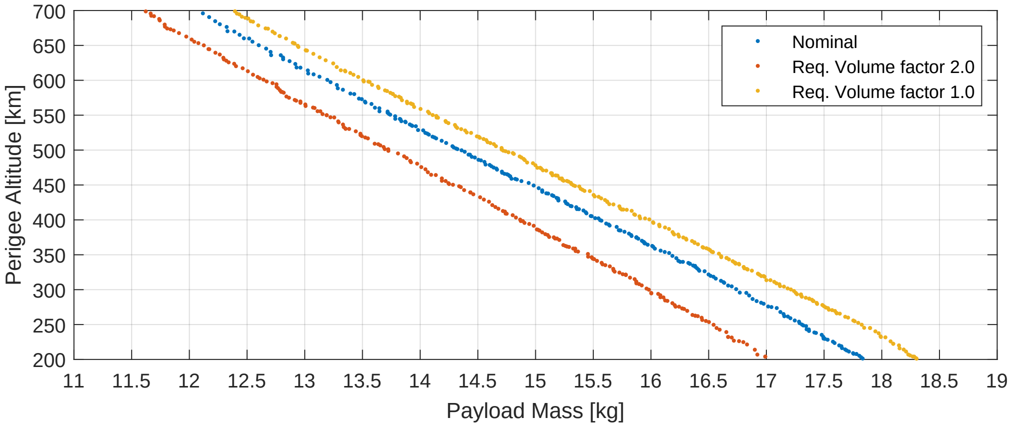

Figure 7.4: Perigee altitude vs payload mass of the Pareto fronts of the required fairing volume factor sensitivity analysis and the nominal solution

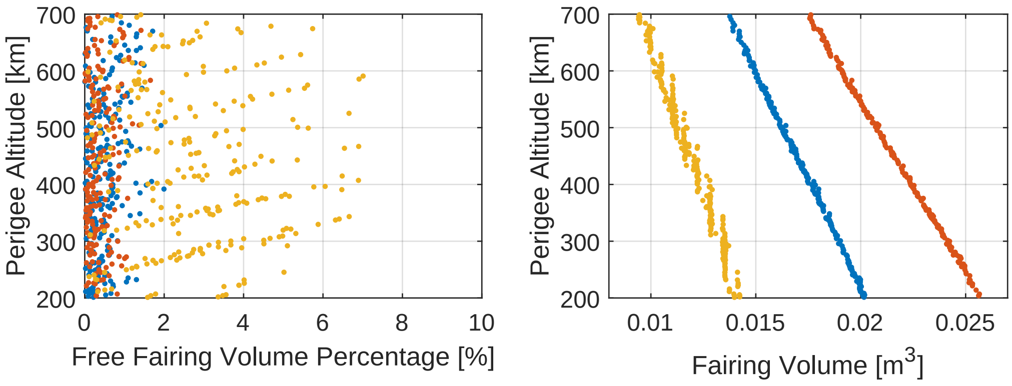

Figure 7.5: Perigee altitude vs free fairing volume and fairing volume of the Pareto fronts of the required fairing volume factor sensitivity analysis and the nominal solution (colouring in accordance with Figure 7.4)

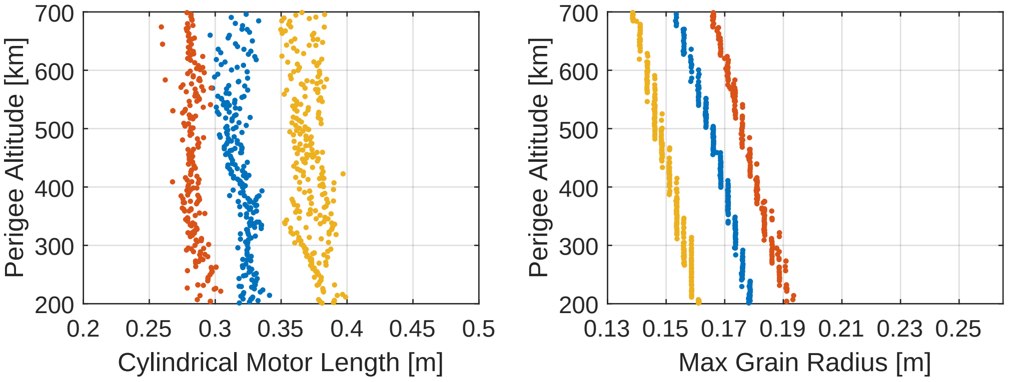

Figure 7.6: Perigee altitude vs cylindrical motor length and maximum grain radius of the Pareto fronts of the required fairing volume factor sensitivity analysis and the nominal solution (colouring in accordance with Figure 7.4)

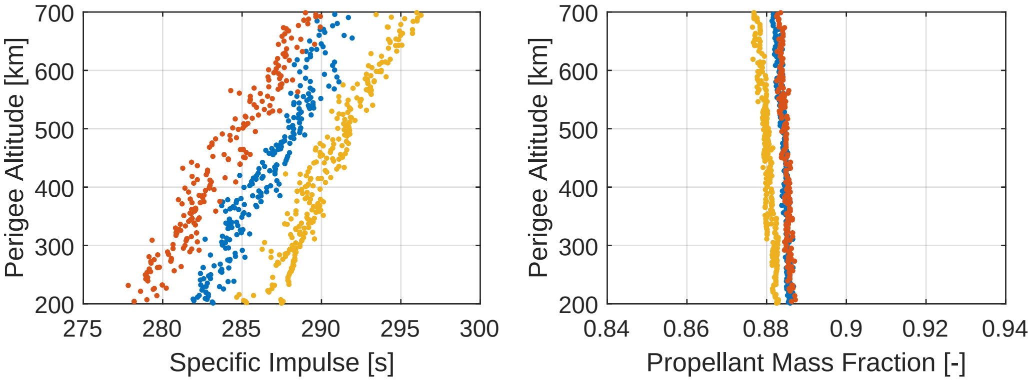

Figure 7.7: Perigee altitude vs specific impulse and propellant mass fraction of the Pareto fronts of the required fairing volume factor sensitivity analysis and the nominal solution

leads to a higher expansion ratio and consequently a higher specific impulse, as seen in Figure 7.7. However, the smaller grain radius also leads to a smaller propellant volume, which causes a smaller propellant mass fraction for the case with a factor of 1.0.

The case with a factor of 2.0 has a roughly equal or even slightly higher propellant mass fraction than the nominal case with a factor of 1.5. However, the performance is still worse due to factors such as a lower specific impulse and a larger fairing mass.

7.4. Bending Load Constraint Value

In the nominal case a maximum bending load constraint value was implemented of 10000 Pa·rad. This value is based on the maximum value that the Pegasus XL endures during launch. However, because the launch vehicle in the MDO has a lower slenderness ratio than the Pegasus XL, this value could be higher in the MDO. To analyse the effect of a higher maximum bending load constraint value an optimization is run with 11000 Pa·rad implemented instead of 10000.

Figure 7.8 shows the comparison of the nominal case and the case with a higher maximum bending load. The spread in the maximum bending load in the nominal results suggested that the solution was not very sensitive to the value of the maximum bending load. This is

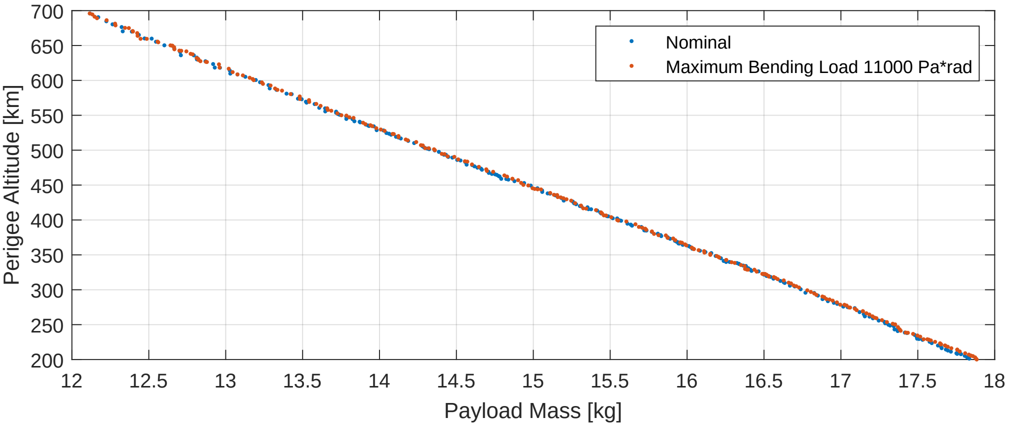

Figure 7.8: Perigee altitude vs payload mass of the Pareto fronts of the maximum bending load constraint sensitivity analysis and the nominal solution

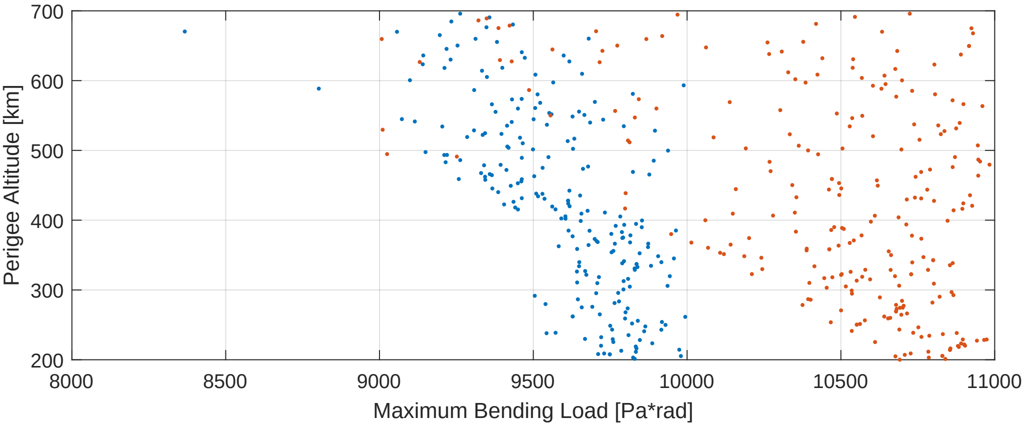

Figure 7.9: Perigee altitude vs maximum bending load of the Pareto fronts of the maximum bending load constraint sensitivity analysis and the nominal solution

confirmed by Figure 7.8. For the lower altitudes a very small payload increase is seen, while for higher altitudes it remains the same.

Figure 7.9 also shows that for lower altitudes the maximum bending load does increase compared to the nominal case, but that for higher altitudes most individual remain under 10000 Pa·rad.

7.5. Coefficient of Convective Heat Transfer

Using the Modified Reynolds Analogy can lead to errors of up to 40% in the determined Stanton number. The Stanton number is directly proportional to the coefficient of convective heat transfer in the used model. A different coefficient of convective heat transfer can lead to a different TPS mass and therefore impact performance. A sensitivity analysis is performed on the coefficient of convective heat transfer with a margin of 40%. The results are shown in Figure 7.10. It can be seen that the effect on the payload mass at a certain perigee altitude of a decrease in the value of the coefficient of convective heat transfer has roughly the same magnitude as an increase. As expected, a higher value leads to a lower performance. With a change of 40% at 200 km perigee altitude the payload mass changes

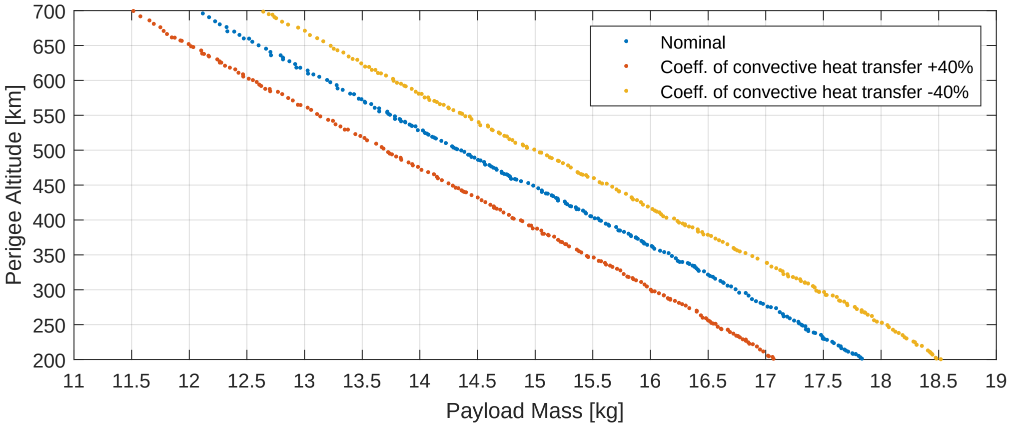

Figure 7.10: Perigee altitude vs payload mass of the Pareto fronts of the coefficient of convective heat transfer sensitivity analysis and the nominal solution

with 0.7 kg. At 700 km perigee altitude the change is 0.5 kg.

7.6. Chamber Pressure and Propellant Burn Characteristics

It was observed in the results for the nominal case that the chamber pressure converges to its lower boundary of 30 bar. This suggests that a lower value for the chamber pressure could increase the performance of the launch vehicle. Therefore, an optimization is performed with the lower boundary set to the deflagration limit of the propellant at 20 bar. The results of optimization with the lower chamber pressure boundary is compared with the nominal results in Figure 7.11.

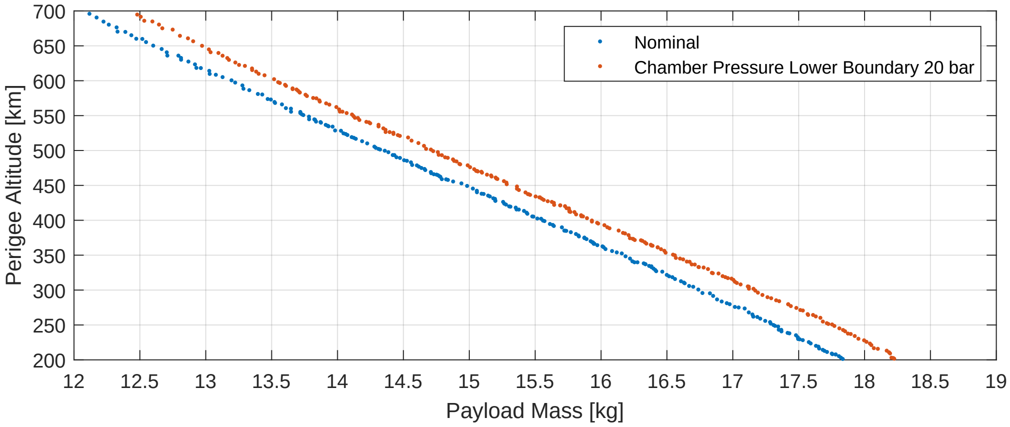

Figure 7.11: Perigee altitude vs payload mass of the Pareto fronts of the lower chamber pressure boundary sensitivity analysis and the nominal solution

The performance increases slightly compared to the nominal case. In this case the payload mass seems to increase with a constant value over the whole range of perigee altitudes, where in the cases of other parameters at lower orbital altitudes larger increases in payload mass were seen than for higher altitudes.

Figure 7.12 shows the values for the chamber and exit pressures of the Pareto fronts. It shows that the new chamber pressure value again converges to its lower boundary. The exit pressure also drops, but not with the same factor as the chamber pressure. That means that the expansion ratio will be lower and, thus, the specific impulse will also be lower. This is confirmed by Figure 7.13.

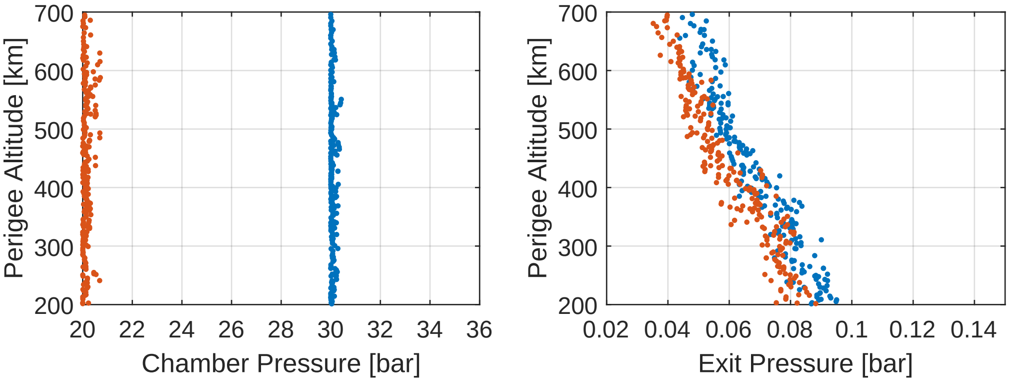

Figure 7.12: Perigee altitude vs pressure values of the Pareto fronts of the lower chamber pressure boundary sensitivity analysis and the nominal solution (colouring in accordance with Figure 7.11)

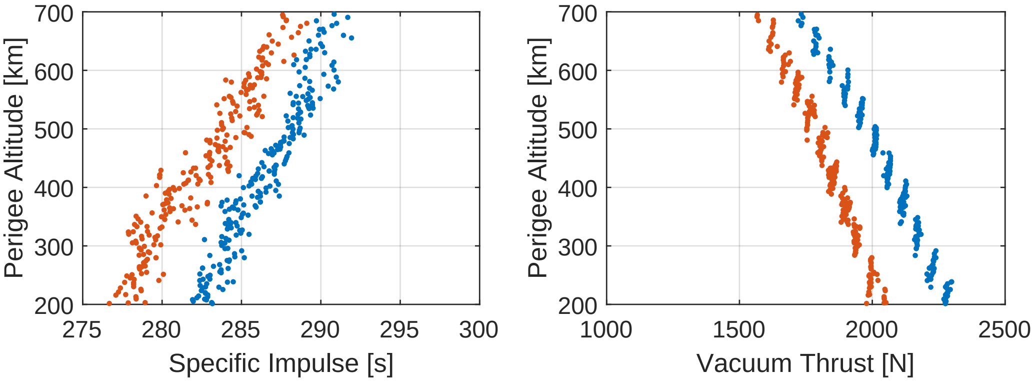

Figure 7.13: Perigee altitude vs motor performance values of the Pareto fronts of the lower chamber pressure boundary sensitivity analysis and the nominal solution (colouring in accordance with Figure 7.11)

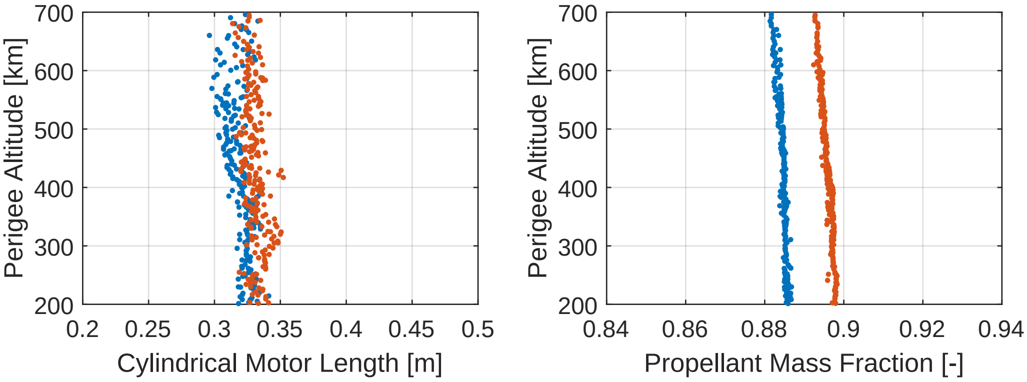

Figure 7.14: Perigee altitude vs cylindrical case length and propellant mass fraction values of the Pareto fronts of the lower chamber pressure boundary sensitivity analysis and the nominal solution (colouring in accordance with Figure 7.11)

How the performance has still increased can be explained with the propellant mass fraction, which has increased. The cylindrical case length has increased to increase the total propellant capacity. A higher propellant mass in combination with a lower structural mass due to the lower MEOP results in a higher propellant mass fraction as shown in Figure 7.14.

The tendency of the optimal solutions to converge to the lower chamber pressure boundary, and therefore a smaller mass flow from the grain, suggests that a propellant with a lower burn rate exponent could increase the performance. Therefore, a sensitivity analysis will be performed for this parameter. The nominal propellant has a burn rate exponent of 0.3. The burn rate exponents of HTPB/AP/Al propellants generally range from 0.3 to 0.4 [45]. Other AP/Al propellants can have burn rate exponents as low as 0.03. For this analysis a burn rate of 0.2 and 0.4 will be analysed. Even though a different burn rate exponent is used, the other values are still taken from the TPH-3340 propellant. The results are given in Figure 7.15.

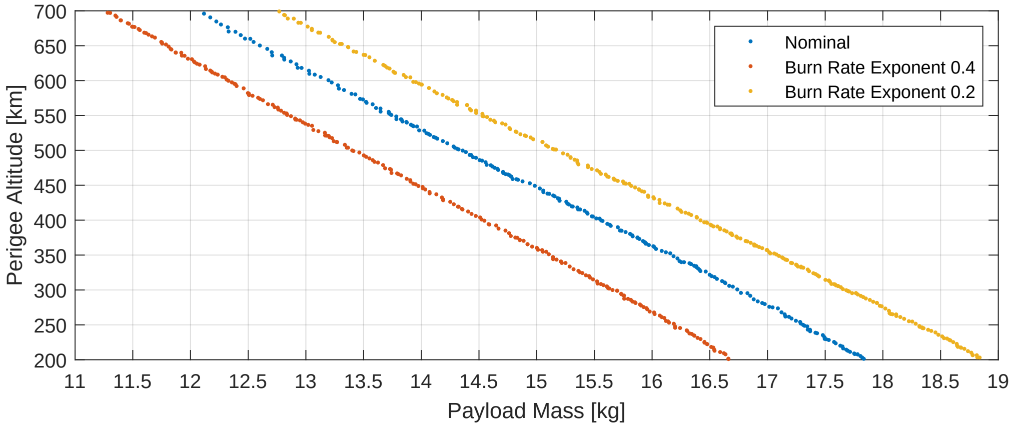

Figure 7.15: Perigee altitude vs payload mass of the Pareto fronts of the burn rate exponent sensitivity analysis and the nominal solution

Figure 7.15 shows a significant difference in payload mass for a different burn rate exponent. A burn rate exponent of 0.2 increases the payload mass at 200 km perigee altitude with 1 kg, while a burn rate exponent of 0.4 decreases it with 1.2 kg. At 700 km perigee altitude the payload mass decreases with 0.8 kg and increases with 0.7 kg for burn rate exponents of 0.4 and 0.2, respectively.

7.7. Combination of Uncertainties

After seeing what the effect is of each uncertainty separately, it is interesting to analyse what effect interactions between uncertain parameters have on the performance. Therefore, the uncertainties of the parameters that had a clear effect on the performance individually are combined to create best and worst case performances. The uncertain parameters used here are the axial force coefficient, available length, required volume factor and the coefficient of convective heat transfer.

The results are shown in Figure 7.16. Clearly, the effects add up to a greater performance decrease and increase. Still however, even for the worst case, the payload mass at 700 km

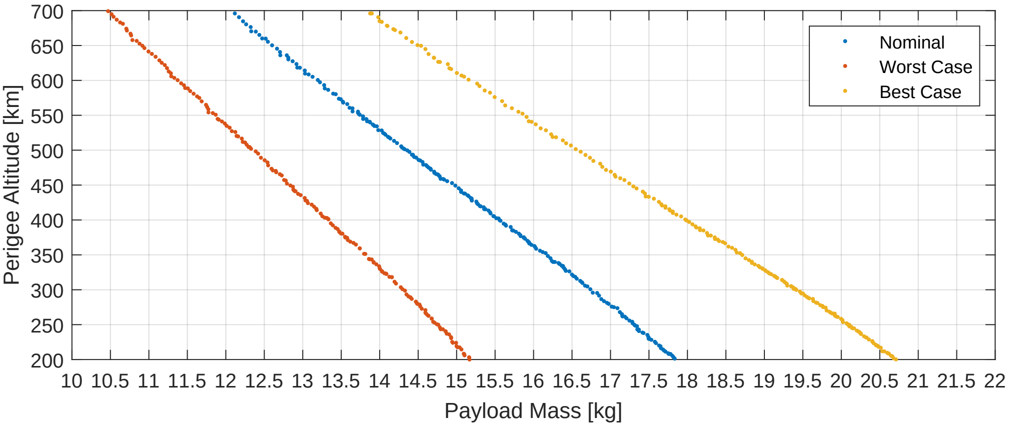

Figure 7.16: Perigee altitude vs payload mass of the Pareto fronts of the best and worse case performances and the nominal solution

perigee altitude is larger than 10 kg at 10.5 kg. At 200 km perigee altitude the payload mass reduces to 15.2 kg for the worst case. For the best case, the payload mass at 200 km becomes 20.7 kg and 13.9 kg at 700 km.

7.8. Sensitivity Analysis Conclusions

None of the uncertainties evaluated have an effect on the payload mass per perigee altitude that it prevents the launch vehicle to launch a microsatellite. The largest sensitivity occurs for the available length where the difference can be almost 1 kg at 200 km perigee altitude. However, other uncertain parameters, such as the normal force coefficient and the maximum bending load, showed no significant difference in the solutions. For most uncertainties the performance boost or reduction reduced as the perigee altitude increased. This does not apply to the coefficient of convective heat transfer, where the performance changes are roughly constant along the entire range of perigee altitudes. Combining the maximum uncertainties in the parameters shows that the performances changes add up. Even with all unfavourable uncertainties applied, the payload mass at 700 km perigee altitude remained above 10 kg.

With certain variable design parameters it is possible to increase the performance. Lowering the chamber pressure to 20 bar resulted in a performance increase of roughly 0.4 kg payload mass along the range of perigee altitudes. The optimal solutions also showed a high sensitivity to the burn rate exponent. Decreasing the burn rate exponent to 0.2 can increase payload mass with roughly 1 kg. However, increasing the value to 0.4 can reduce the payload mass with more than 1 kg.

To summarize the sensitivity analysis results, the percentage of payload difference at 200 km and 700 km perigee altitude of each case has been put in Table 7.1. To find the payload differences at the exact altitudes of 200 km and 700 km linear interpolation was performed between the closest individual below and above the required perigee altitude. The differences in percent are rounded to one decimal. Table 7.1 shows that the performance of the combined effect of the uncertainties is slightly better than when the individual performance changes would be simply added up.

Table 7.1: Summary of sensitivity analysis results

Sensitivity Parameter	**Margin**	**Payload difference at 200 km perigee altitude [%]**	**Payload difference at 700 km perigee altitude [%]**
Axial Force Coefficient	+12%	-2.4	-1.7
	-12%	2.7	2.2
Normal Force Coefficient	+3%	0.0	0.0
	-3%	-0.1	-0.2
Available Length	+0.05 m	5.0	3.5
	-0.05 m	-5.2	-3.7
Required Volume Factor	+0.5	-4.7	-3.8
	-0.5	2.6	2.6
Bending Load Constraint	+1000 Pa·rad	0.3	0.0
Coeff. of Conv. Heat Transfer	+40%	-4.3	-4.6
	-40%	3.8	4.7
Chamber Pressure Lower Boundary	-10 bar	2.1	3.0
Burn Rate Exponent	+0.1	-6.6	-6.5
	-0.1	5.6	5.8
Combination of Uncertainties	Best	16.0	14.7
	Worst	-15.0	-13.2

8

Conclusions and Recommendations

In this chapter the conclusion will be presented that can be obtained from the results. Furthermore, recommendations are given for the improvement of the models for future research.

8.1. Conclusions

The dependency on space capabilities of military entities can become a weakness when enemy forces establish counter-space capabilities. It may therefore become important to be able to replenish lost capabilities and/or grant additional capabilities from space assets quickly, which is called Responsive Space. The continuous miniaturization of technologies has enabled small satellites to fulfill many desired functions. To launch such satellites, it might be possible to modify a missile to a small launch vehicle that can be launched from a naval ship, thereby giving the military autonomous space launch capability.
The following research question was established:

Is it technically feasible to launch a microsatellite from the Mark 41 Vertical Launching System by modifying an already integrated missile?

To help answer the research question, a sub-question was established:

What is the optimal performance in terms of payload mass in orbit of the new launch vehicle?

another sub question was:

How does a change in launch conditions and target orbit affect the optimal design?

and also:

How sensitive is the optimal solution to uncertainties in parameters?

To answer these questions a Multidisciplinary Design Optimization was performed to optimize a launch vehicle that is modified from the existing SM-3 Block IIA. The tool optimizes two objectives: the payload mass and the perigee altitude of the orbit.

The maximum payload mass is achieved when launched for an equatorial orbit from the equator. This gives a payload mass of 17.8 kg at an orbit with a perigee altitude of 200 km which decreases almost linearly to 12.1 kg at 700 km perigee altitude. It must be noted that the payload mass determined here includes the mass of the payload adapter and avionics of the upper stage.
The largest value for the GTOW was 2346 kg occurring for the lower orbital altitudes, while the smallest value of 2316 kg occurred at the higher orbital altitudes. These are only small increases from the estimated GTOW of the SM-3 Block IIA of 2312 kg.

Another launch site and other orbital inclinations were also evaluated. The launch location has a latitude angle of 52.958 degrees and a longitude angle of 4.786 degrees. From this location it will be launched to an orbit with a 58 degrees inclination angle and a polar orbit with 90 degrees inclination.
For both inclinations the payload mass at a certain perigee altitude decreases compared to the equatorial orbit, as expected. For a 58 degrees inclination orbit a payload mass of 15.8 kg at 200 km perigee altitude is reached and for the polar orbit 13.6 kg can be launched at the same perigee altitude. At 700 km perigee altitude, the values are 10.7 kg and 9.2 kg, respectively.

Sensitivity analyses have been performed with a one-at-a-time approach to evaluate the sensitivity of the optimal solutions to uncertainty in several parameters. The comparison is made for an equatorial orbit.
Firstly, an uncertainty of 12% in the axial force coefficient is analysed. An increase of 12% reduces the payload mass over the whole range of perigee altitudes. The reduction is ~0.4 kg at 200km and ~0.2 kg at 700 km perigee altitude. A reduction of 12% in the axial force coefficient gives a payload increase over the whole range with ~0.5 kg at 200 km and ~0.3 kg at 700 km perigee altitude.
The uncertainty of 3% in the normal force coefficient is not significant as the performance change is negligible.
Secondly, the uncertainty in the lengths of the second and third stages of the SM-3 Block IIA is analysed. The uncertainty in these lengths creates an uncertainty in the available length for the upper stage. An increase in available length of 0.05 m increases the payload mass at 200 km perigee altitude to 18.7 kg, while a reduction of 0.05 m reduces the payload mass to 16.9 kg at the same altitude. At 700 km perigee altitude the payload mass reduces to 11.6 kg and increases to 12.5 kg for a available length reduction and increase, respectively.
The estimated factor of 1.5 for the required volume of the fairing is also investigated. Changing the factor to 1.0 increases the payload mass over the entire range of perigee altitudes. At 200 km perigee altitude the payload mass becomes 18.3 kg and at 700 km 12.4 kg. Increasing the factor to 2.0 has a notably larger effect on the payload mass. It decreases the payload mass to 17 kg at 200 km and to 11.6 kg at 700 km perigee altitude.
The solution is insensitive to the maximum bending load constraint as increasing the value to 11000 shows only a very small increase for lower orbital altitudes. At all other altitudes the difference is negligible.
Lowering the lower boundary for the chamber pressure to 20 bar resulted in a better per-

formance of the launch vehicle. The increase of 0.4 kg is roughly constant across the total range of perigee altitudes.
Lastly, changing the burn rate exponent had a significant effect on the payload mass per perigee altitude. Lowering the exponent to 0.2 increased the payload mass at 200 km perigee altitude to 18.8 kg and at 700 km to 12.8 kg. A burn rate exponent of 0.4 decreased the performance at 200 km to 16.7 kg and to 11.3 kg at 700 km.

Concluding, it follows from the results and the sensitivity analyses that it is technically feasible to develop a micro satellite launch vehicle that can be launched from the Mark 41 Vertical Launching System by modifying an already integrated missile. Using the SM-3 Block IIA with an additional upper stage, over a large range of the evaluated orbital altitudes a payload mass of over 10 kg can be launched. Also for less advantageous orbits as an equatorial orbit the payload mass remained over 10 kg for most of the evaluated perigee altitudes. However, for a polar orbit with a perigee altitude of over 600 km, it is not possible anymore to launch to launch a payload of over 10 kg. It must be noted, however, that the payload mass includes the payload adapter and avionics mass of the upper stage. Thus, the range of perigee altitudes to which 10 kg of actual payload mass can be launched is actually smaller.
The results from the sensitivity analysis show that none of the uncertainties in the parameters had such a large effect on the payload mass that they would prevent the launch vehicle from launching a payload mass of over 10 kg over the whole range of orbital altitudes. The largest effect was seen for the available length for the upper stage and fairing where a change of 0.05 m caused a change in payload mass of almost 1 kg at 200 km perigee altitude. Also, combining the uncertainties showed that even for the worst case the payload mass at 700 km perigee altitude remained larger than 10 kg. Additionally, decreasing the chamber pressure and/or choosing a propellant with a smaller burn rate exponent could even improve performance.

8.2. Recommendations

In this section several recommendations will be given to improve the models used here for future research.

- The nozzle has been modeled as a slightly submerged nozzle. However, in the model the propellant grain is not modeled around the submerged part of the nozzle. Doing so would increase the propellant mass fraction and therefore also the performance. However, the model is not able to calculate thrust profiles of such grain configurations. Therefore, it is recommended to improve the propulsion model so that more thrust profiles can be evaluated. This could also create the opportunity to optimize the grain shape.

- Not many small launch vehicles have yet been put into operation. Therefore, not much data is available on such systems or their subsystems. It is likely that in the future more data will become available and, if so, it is recommended to update the mass estimation relationships etc. Also, the avionics and payload adapter mass may then be more accurately estimated.

- It is recommended to improve the estimation of the thermal protection system mass.

Firstly, the thermal protection material used in the upper stage is chosen based on the material used in the STAR series motors. This material has good insulation properties and reasonable ablation properties. In the model the thickness has only been determined with the ablation properties. A material with better ablative properties could increase performance. Additionally, the thermal properties of the structural material have not been taken into account. Including this would improve the model and could also enable a better material selection.

- As explained in the Introduction, it was unfortunately not possible to create an accurate cost model to analyze the cost of the new launch vehicle. However, to draw a conclusion on the cost-effectiveness, a cost estimate is needed. To be able to do this in the future, it is recommended to obtain cost data from the SM-3 Block IIA or similar systems. Also, to evaluate the differences with a completely new launch vehicle, more accurate cost models are needed for small launch vehicles. The cost models that exist, even for small launch vehicles, are not valid for a launch vehicle of the scale of the SM-3. Lastly, a study is needed to determine whether the strategic value this new capability brings is worth the cost.

A

TPH-3340 Thermodynamic Data

This appendix includes the thermodynamic data for the propellant TPH-3340. The data has been determined with the software CEA. The propellant is composed of 11% HTPB, 71% ammonium-perchlorate and 18% of aluminium powder. Ammonium-perchlorate and aluminium are available in the CEA database. HTPB is input manually with a heat of decomposition of -52.58 kJ/mol and a chemical formula of C 10, H 15.09, O 0.23, N 0.10 [50].

Table A.1: Temperature, molar mass and specific heat ratio for TPH-3340 propellant for different chamber pressures

Chamber pressure	**Temperature**	**Molar mass**	**Specific heat ratio**
[bar]	**[K]**	**[g/mol]**	**[-]**
20	3462.48	29.345	1.1207
21	3468.09	29.365	1.1209
22	3473.42	29.383	1.1211
23	3478.5	29.401	1.1213
24	3483.36	29.418	1.1214
25	3488.01	29.434	1.1216
26	3492.47	29.450	1.1218
27	3496.75	29.465	1.1219
28	3500.87	29.480	1.1220
29	3504.83	29.494	1.1222
30	3508.65	29.507	1.1223

Chamber pressure	**Temperature**	**Molar mass**	**Specific heat ratio**
[bar]	**[K]**	**[g/mol]**	**[-]**
31	3512.34	29.520	1.1225
32	3515.91	29.533	1.1226
33	3519.36	29.545	1.1227
34	3522.69	29.557	1.1228
35	3525.93	29.568	1.1229
36	3529.07	29.580	1.1230
37	3532.12	29.590	1.1231
38	3535.08	29.601	1.1232
39	3537.96	29.611	1.1233
40	3540.76	29.621	1.1234
41	3543.48	29.631	1.1235
42	3546.14	29.641	1.1236
43	3548.73	29.650	1.1237
44	3551.25	29.659	1.1238
45	3553.72	29.668	1.1239
46	3556.12	29.677	1.1240
47	3558.47	29.685	1.1241
48	3560.77	29.693	1.1241
49	3563.02	29.702	1.1242
50	3565.21	29.709	1.1243
51	3567.36	29.717	1.1244
52	3569.47	29.725	1.1244
53	3571.53	29.732	1.1245
54	3573.55	29.740	1.1246
55	3575.53	29.747	1.1247
56	3577.47	29.754	1.1247
57	3579.37	29.761	1.1248
58	3581.24	29.768	1.1248
59	3583.08	29.775	1.1249
60	3584.87	29.781	1.1250
61	3586.64	29.788	1.1250
62	3588.38	29.794	1.1251
63	3590.08	29.800	1.1252
64	3591.76	29.806	1.1252
65	3593.41	29.812	1.1253
66	3595.03	29.818	1.1253
67	3596.62	29.824	1.1254
68	3598.19	29.830	1.1254
69	3599.73	29.836	1.1255
70	3601.25	29.841	1.1255

Chamber pressure	**Temperature**	**Molar mass**	**Specific heat ratio**
[bar]	**[K]**	**[g/mol]**	**[-]**
71	3602.74	29.847	1.1256
72	3604.22	29.852	1.1256
73	3605.67	29.858	1.1257
74	3607.09	29.863	1.1257
75	3608.5	29.868	1.1258
76	3609.89	29.873	1.1258
77	3611.25	29.879	1.1259
78	3612.6	29.884	1.1259
79	3613.93	29.889	1.1260
80	3615.24	29.893	1.1260
81	3616.53	29.898	1.1260
82	3617.8	29.903	1.1261
83	3619.06	29.908	1.1261
84	3620.3	29.912	1.1262
85	3621.52	29.917	1.1262
86	3622.73	29.921	1.1263
87	3623.93	29.926	1.1263
88	3625.1	29.930	1.1263
89	3626.27	29.935	1.1264
90	3627.42	29.939	1.1264
91	3628.55	29.943	1.1264
92	3629.67	29.948	1.1265
93	3630.78	29.952	1.1265
94	3631.87	29.956	1.1266
95	3632.95	29.960	1.1266
96	3634.02	29.964	1.1266
97	3635.08	29.968	1.1267
98	3636.12	29.972	1.1267
99	3637.16	29.976	1.1267
100	3638.18	29.980	1.1268

B

Solid Rocket Motor Database

To validate the propulsion model, a database is made of solid rocket motors and their parameters. As the propulsion model is used only for the modelling of the upper stage, only data of relatively small SRMs is used. The data is obtained from the Northrop Grumman Propulsion Products Catalog [46]. To obtain the required units, the values from the catalog must be multiplied with a conversion factor. The conversion factors used in this report are given in Table B.1.

Table B.1: Conversion factors for different units

inch to meter	0.0254
psia to bar	0.06894757
lbf to Newton	4.44822162
lbm to kg	0.45359237

The solid rocket motors and their properties are given in Table B.2.

Table B.2: STAR series SRMs and their properties

	12GV	**13B**	**15G**	**24**	**27H**
Diameter [in]	12.24	13.57	15.04	24.5	27.3
Total length [in]	22.5	25.11	31.57	40.5	48
Burn time [s]	13.9	14.8	33.3	29.6	46.3
Average chamber pressure [psia]	1550	823	885	486	596
Maximum chamber pressure [psia]	1950	935	1585	524	633
Effective specific impulse [s]	282.4	285	281.8	282.9	291.4
Average thrust [lbf]	1455	1708	1470	4170	4650
Maximum thrust [lbf]	1980	2160	2800	4420	5250
Expansion ratio [-]	58	49.8	70	37.8	81.7
Total mass [lbm]	92.5	103.7	206.6	481	810.9
Propellant mass [lbm]	72.6	90.9	175.5	440.6	744.8
Motor case mass [lbm]	14.3	5.6	22.6	13	21.8
Nozzle mass [lbm]	4.5	3.7	4.6	13.1	29
Total inert mass [lbm]	19.8	12.8	30.9	40.4	66.1
Propellant mass fraction [-]	0.79	0.88	0.85	0.92	0.92
Measured pressure at start of burn [psia]	760	-	1090	-	590
Measured thrust at start of burn [lbf]	530	-	1460	-	4240
Initial throat diameter [in]	0.691	-	0.97	-	2.2
Motor case length [in]	-	15.6	-	24.5	30.2
Case material	Graphite-Epoxy composite	Titanium	Graphite-Epoxy composite	Titanium	Titanium
Included in performance validation?	Yes	No	Yes	No	Yes
Included in motor case mass validation?	No	Yes	No	Yes	Yes
Included in nozzle mass estimation?	No	Yes	Yes	Yes	Yes

	30BP	**30CBP**	**30E**	**31**	**37FM**
Diameter [in]	30	30	30	30.1	36.8
Total length [in]	59.3	64.3	66.3	113	66.5
Burn time [s]	54	51	51.1	45	62.7
Average chamber pressure [psia]	514	552	537	712	540
Maximum chamber pressure [psia]	595	604	590	865	642
Effective specific impulse [s]	292.3	291.8	290.4	293.5	289.8
Average thrust [lbf]	5985	7400	7900	18500	10827
Maximum thrust [lbf]	6945	8550	8850	21500	12325
Expansion ratio [-]	73.7	63.2	58.6	58	48.2
Total mass [lbm]	1196.7	1393.6	1485.7	3072	2530.8
Propellant mass [lbm]	1113.6	1302.5	1392	2835	2350.1
Motor case mass [lbm]	30.5	35.7	37.9	92	71.1
Nozzle mass [lbm]	33.8	34.5	33.6	65.5	75
Total inert mass [lbm]	83.1	90.6	93.7	237	180.1
Propellant mass fraction [-]	0.930	0.930	0.930	0.920	0.930
Measured pressure at start of burn [psia]	430	445	462	630	505
Measured thrust at start of burn [lbf]	4500	5530	6170	13500	9080
Initial throat diameter [in]	2.68	2.89	3	3.74	3.52
Motor case length [in]	35.3	40.1	41.9	-	48.6
Case material	Titanium	Titanium	Titanium	Kevlar-Epoxy composite	Titanium
Included in performance validation?	Yes	Yes	Yes	Yes	Yes
Included in motor case mass validation?	Yes	Yes	Yes	No	Yes
Included in nozzle mass estimation?	Yes	Yes	Yes	No	Yes

	37FMV	**37XFP**	**48ASN**	**48ALN**	**48BSN**	**48BLN**
Diameter [in]	36.8	36.7	49	49	49	49
Total length [in]	75.5	59.2	80	88	72	80
Burn time [s]	62.7	66	87.2	87.2	84.1	84.1
Average chamber pressure [psia]	540	527	543	543	579	579
Maximum chamber pressure [psia]	642	576	607	607	618	618
Effective specific impulse [s]	293.7	290	283.4	289.9	286	292.1
Average thrust [lbf]	10980	8550	17350	17750	15100	15430
Maximum thrust [lbf]	12500	9550	21150	21650	17110	17490
Expansion ratio [-]	70	54.8	31.2	43.1	39.6	54.8
Total mass [lbm]	2578.8	2107.1	5673.7	5691.1	4705.4	4720.8
Propellant mass [lbm]	2345.3	1948.2	5357.2	5357.2	4431.2	4431.2
Motor case mass [lbm]	71.1	58.1	153.6	153.6	128.5	128.5
Nozzle mass [lbm]	99	70	84.4	101.8	81.2	96.6
Total inert mass [lbm]	236.7	159.6	316.5	333.9	274.2	289.6
Propellant mass fraction [-]	0.910	0.925	0.940	0.940	0.940	0.940
Measured pressure at start of burn [psia]	495	520	460	450	555	560
Measured thrust at start of burn [lbf]	9130	7750	13200	12750	13000	13260
Initial throat diameter [in]	3.52	3.18	4.49	4.49	3.98	3.98
Motor case length [in]	-	41.5	64	59.3	52.5	51
Case material	Titanium	Titanium	Titanium	Titanium	Titanium	Titanium
Included in performance validation?	Yes	Yes	Yes	Yes	Yes	Yes
Included in motor case mass validation?	No	Yes	Yes	Yes	Yes	Yes
Included in nozzle mass estimation?	No	Yes	Yes	Yes	Yes	Yes

C

Derivation Tangent Ogive Nose Cone Volume

Figure 4.1 shows the cross section of a tangent ogive nose cone. To calculate the volume of the nose cone, an x-axis is established that runs along the axis of symmetry with length L. Then, using the same notation as in the figure, the height of the nose cone, denoted with y, becomes:

$$y = \sqrt{\rho^2 - (L - x)^2} + R - \rho \tag{C.1}$$

Determining the volume is done by integrating the cross-sectional area of the nose cone along the length L:

$$V = \int_0^L \pi y^2 \, \mathrm{d}x \tag{C.2}$$

Substituting y and expanding gives:

$$\begin{aligned} V = & 2\pi(R-\rho) \cdot \int_0^L \sqrt{\rho^2 - (x-L)^2} \mathrm{d}x \\ & - \pi \int_0^L x^2 \mathrm{d}x \\ & + 2\pi L \cdot \int_0^L x \mathrm{d}x \\ & + \pi \left((R-\rho)^2 + \rho^2 - L^2 \right) \cdot \int_0^L 1 \mathrm{d}x \end{aligned} \tag{C.3}$$

Now the resulting integrals will be solved one by one. First substituting:

$$u = x - L \longrightarrow \mathrm{d}u = \mathrm{d}x \tag{C.4}$$

gives:

$$\int \sqrt{\rho^2 - (x-L)^2} \mathrm{d}x = \int \sqrt{\rho^2 - (u)^2} \mathrm{d}u \tag{C.5}$$

u can then be substituted as:

$$u = \rho \sin v \longrightarrow v = \left(\arcsin \frac{u}{\rho} \right), \mathrm{d}u = \rho \cos v \tag{C.6}$$

This results in:

$$\int \rho \cos(v)\sqrt{p^2 - \rho^2 \sin^2(v)}\mathrm{d}v \tag{C.7}$$

This can be simplified to:

$$\rho^2 \int \cos^2(v)\mathrm{d}v \tag{C.8}$$

Now applying the reduction formula with $n = 2$:

$$\int \cos^n(v)\mathrm{d}v = \frac{n-1}{n}\int \cos^{n-2}(v)\mathrm{d}v + \frac{\cos^{n-1}(v)\sin(v)}{n} \tag{C.9}$$

gives:

$$\rho^2 \int \cos^2(v)\mathrm{d}v = \rho^2\left(\frac{\cos(v)\sin(v)}{2} + \frac{1}{2}\int 1\mathrm{d}v\right) \tag{C.10}$$

Solving the integral and undoing the substitution $v = \left(\arcsin \frac{u}{\rho}\right)$ yields:

$$\rho^2\left(\frac{\cos(v)\sin(v)}{2} + \frac{1}{2}\int 1\mathrm{d}v\right) = \frac{\rho^2 \arcsin\left(\frac{u}{\rho}\right)}{2} + \frac{\rho u\sqrt{1-\frac{u^2}{\rho^2}}}{2} \tag{C.11}$$

Then undoing the substitution $u = x - L$ yields:

$$\frac{\rho^2 \arcsin\left(\frac{u}{\rho}\right)}{2} + \frac{\rho u\sqrt{1-\frac{u^2}{\rho^2}}}{2} = \frac{\rho^2 \arcsin\left(\frac{x-L}{\rho}\right)}{2} + \frac{\rho(x-L)\sqrt{1-\frac{(x-L)^2}{\rho^2}}}{2} \tag{C.12}$$

The other integrals from Equation C.3 are more easily solved:

$$\int x^2\mathrm{d}x = \frac{x^3}{3} \tag{C.13}$$

and:

$$\int x\mathrm{d}x = \frac{x^2}{2} \tag{C.14}$$

and lastly:

$$\int 1\mathrm{d}x = x \tag{C.15}$$

Substituting everything into Equation C.3 gives:

$$\begin{aligned} V = \Big[&\pi\rho^2(R-\rho)\arcsin\left(\frac{x-L}{\rho}\right) \\ &+ \pi\rho(R-\rho)(x-L)\sqrt{1-\frac{(x-L)^2}{\rho^2}} \\ &- \frac{\pi x^3}{3} + \pi L x^2 + \pi\left((R-\rho)^2 + \rho^2 - L^2\right)x + C\Big]_0^L \end{aligned} \tag{C.16}$$

Solving yields the final solution:

$$\begin{aligned} V_{\mathrm{f}} = \pi \cdot \Big(&- (L \cdot \rho - L \cdot R) \cdot \sqrt{\rho^2 - L^2} \\ &- \arcsin\left(\frac{L}{\rho}\right) \cdot \rho^3 \\ &+ \frac{6 \cdot L \cdot \rho^2 - 6 \cdot L \cdot R \cdot \rho + 3 \cdot L \cdot R^2 - L^3}{3} \\ &+ R \cdot \arcsin\left(\frac{L}{\rho}\right) \cdot \rho^2 \Big) \end{aligned} \tag{C.17}$$

This solution has been verified with Matlab. Calculating the solution with Equation C.17 by filling in $R = 0.2$ m and $L = 0.5$ m gives a volume of 0.035003580233536 m^3. When using the function 'int' in Matlab, which directly calculates the integral from Equation C.2 with y substituted, it gives the exact same solution for all decimals. It is therefore concluded that the derivation of the equation for the volume is correct.

D

Test Results

In this appendix results are given for several tests that were performed. The tests have been performed with a population of 150 individuals and run for 400 generations.

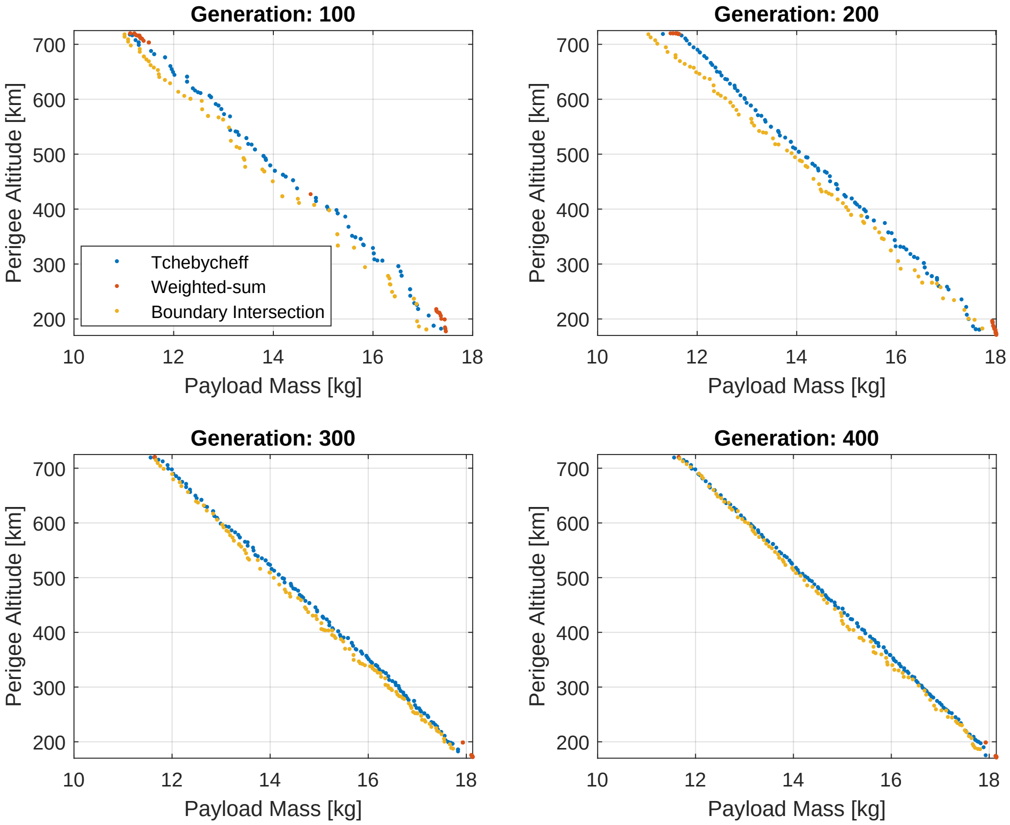

Figure D.1: Comparison of decomposition methods for MOEA/D optimizer for several generations

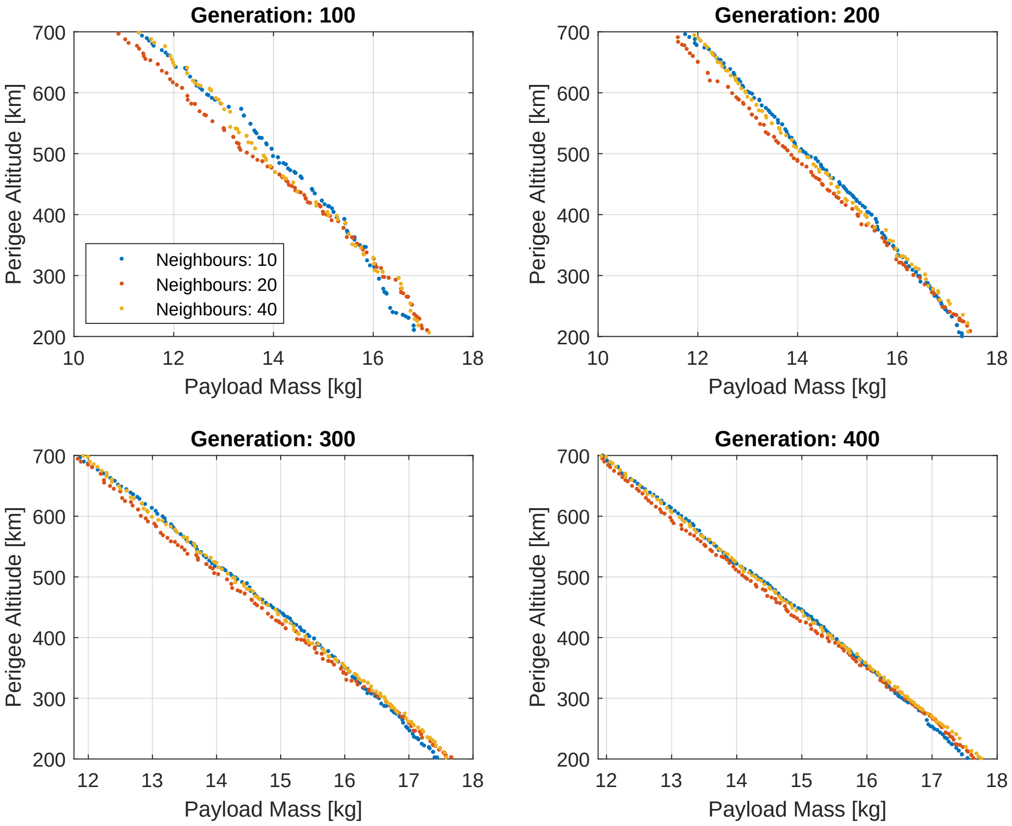

Figure D.2: Comparison of different values for the neighbours setting for MOEA/D optimizer for several generations

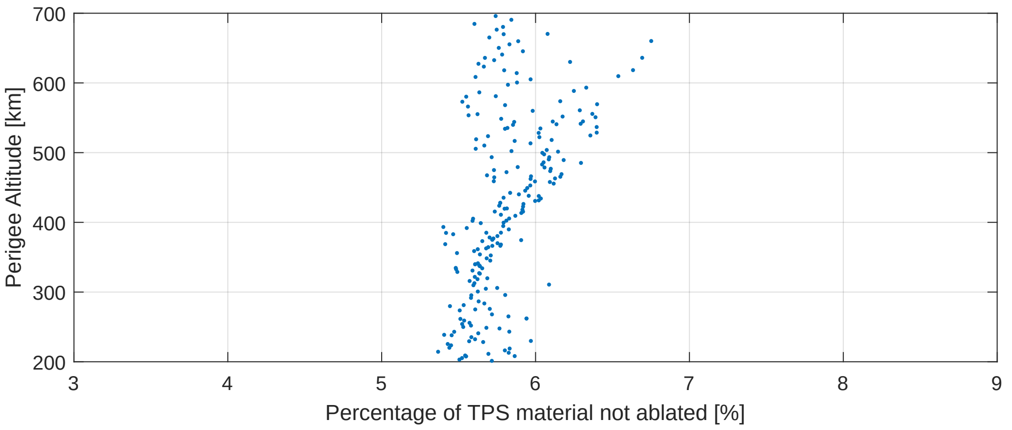

Figure D.3: Percentage of TPS material that is not ablated of a population that occurred during a test run of the MDO

Bibliography

[1] R. Carneal and R. Chang. *Sea-Launched TacSats for Responsive Space (STaRS).* 7th Responsive Space Conference, 2009.

[2] Lockheed Martin. *MK 41 VERTICAL LAUNCHING SYSTEM.* `https://www.lockheedmartin.com/content/dam/lockheed-martin/rms/documents/naval-launchers-and-munitions/MK41_VLS_Vertical_Launching_System_Product%20Card_8.5x11_042419.pdf`, 2019.

[3] E. Mooij and D. Dirkx. *Propagation and Optimization Global Optimization Lecture Slides.* TU Delft, 2019.

[4] M. Turner. *Rocket and Space Propulsion.* Springer/Praxis Publishing, 2009.

[5] B.T.C. Zandbergen. *Thermal Rocket Propulsion Lecture Notes (Version 2.07).* TU Delft, 2018.

[6] Sonia Chalia and Manish Kumar Bharti. *Mathematical Modeling of Ogive Forebodies and Nose Cones.* International Research Journal of Engineering and Technology (IRJET): Vol. 03 Issue: 03, 2016.

[7] MDAA. *Standard Missile-3.* https://missiledefenseadvocacy.org/standard-missile-3/, (Visited on 02-04-2020).

[8] Theodore A. Postol. *How Strategic Anti-Missile Defense of the United States Could be Made to Work.* Princeton University, 2011.

[9] J. Johnson-Freese and R. Savelsberg. *Why Russia Keeps Moving The Football On European Missile Defense: Politics.* `https://breakingdefense.com/2013/10/why-russia-keeps-moving-the-football-on-european-missile-defense-politics/`, 2013.

[10] E. Mooij. *The motion of a vehicle in a planetary atmosphere.* Delft University of Technology, 1994.

[11] M. Balesdent. *Multidisciplinary Design Optimization of Launch Vehicles.* Ecole Centrale de Nantes, 2011.

[12] A. W. Markl. *An Initial Guess Generator for Launch and Reentry Vehicle Trajectory Optimization.* Fakultät Luft- und Raumfahrttechnik der Universität Stuttgart, 2001.

[13] R. Noomen. *Mission Geometry & Orbit Design: Integrators Lecture slides, V4-11.* TU Delft, 2018.

[14] M. W. van Kesteren. *Air Launch versus Ground Launch: a Multidisciplinary Design Optimization Study of Expendable Launch Vehicles on Cost and Performance.* TU Delft, 2013.

[15] L. Doggrell. *Operationally Responsive Space: A Vision for the Future ofMilitary Space.* Air & Space Power Journal Summer 2006, 2006.

[16] W. Frick, J. Guerci, and B. Horais. *Responsive Air Launch.* 2nd Responsive Space Conference, 2004.

[17] A. van Kleef and N. Bernving. *Verkenningsonderzoek: (on)mogelijkheden om vanaf een fregat satellieten te lanceren.* NLR, 2019.

[18] Yoshifumi Inatani and Hirohito Ohtsuka. *SS-520 Nano satellite launcher and its flight result.* Japan Aerospace Exploration Agency, Institute of Space and Astronautical Science (JAXA/ISAS), 2018.

[19] The Committee on an Assessment of Concepts and Systems for U.S. Boost-Phase Missile Defense in Comparison to Other Alternatives. *Making Sense of Ballistic Missile Defense: An Assessment of Concepts and Systems for U.S. Boost-Phase Missile Defense in Comparison to Other Alternatives.* The National Academies Press, 2012.

[20] *Strategic Capabilities of SM-3 Block IIA Interceptors.* `https://mostlymissiledefense.com/2016/06/30/strategic-capabilities-of-sm-3-block-iia-` (Visited on 27-01-2020).

[21] A. Kumpel, P. Barros, C. Burg, F. Villeneuve, and D. Mavris. *A Conceptual Design for the Space Launch Capability of the Peacekeeper ICBM.* Georgia Institute of Technology, 2002.

[22] N. Zafar and H. Linshu. *Multidisciplinary Design Optimization of Solid Launch Vehicle Using Hybrid Algorithm.* Beihang University of Aeronautics & Astronautics (BUAA), 2010.

[23] F. Castellini. *Multidisciplinary Design Optimization for Expendable Launch Vehicles.* Politecnico di Milano, 2012.

[24] M. Ebrahimi, M. Reza Farmani, and J. Roshania. *Multidisciplinary design of a small satellite launch vehicle using particle swarm optimization.* K.N. Toosi Universityof Technology, 2011.

[25] D. J. Bayley. *Design Optimization of Space Launch Vehicles Using a Genetic Algorithm.* Auburn University, 2007.

[26] F. Miranda. *Design Optimization of Ground and AirLaunched Hybrid Rockets.* TU Delft, Master's thesis, 2015.

[27] A. F. Rafique, H. LinShu, A. Kamran, and Q. Zeeshan. *Multidisciplinary design of air launched satellite launch vehicle:Performance comparison of heuristic optimization methods.* School of Astronautics, Beijing University of Aeronautics and Astronautics (BUAA), 2010.

[28] K. F. Wakker. *Fundamentals of Astrodynamics.* TU Delft, 2015.

[29] John Keller. *Air Force eyes next-generation tactical data links gateway for jet fighter communications.* Military & Aerospace Electronics, 2016.

[30] Jason B. Cutshaw. *Future Army nanosatellites to empower Soldiers.* US Army, 2015.

[31] Sandra Erwin. *Air Force launches new project to update missile-warning ground software.* `https://spacenews.com/air-force-launches-new-project-to-update-missile-warning-ground-software/`, (Visited on 15-05-2020).

[32] Georgios Mantzouris, Periklis Papadopoulos, Nikitas Nikitakos, Marco Manso, Alex Bordetsky, Zacharias Sarris, Garik Markarian, and Kyriakos Kourousis. *Picosatellites for Maritime Security Applications - the Lambdasat Case.* Journal of Aerospace Technology and Management: Vol. 7, No. 4, 2015.

[33] L. Fathurrohim, R. E. Poetro, B. Kurniadi1, P. A. Fadillah, and M. Iqbal. *Preliminary Design of Nano Satellite for Regional Navigation System.* Journal of Physics Conference Series, 2018.

[34] H. Visser. *Aircraft Performance Optimization.* TU Delft, 2014.

[35] PaGMO development team. *`https://esa.github.io/pagmo2/docs/problem_list.html`*. ESA, 2019.

[36] R. Noomen. *Mission Geometry & Orbit Design: Optimization Lecture slides, V4-17.* TU Delft, 2018.

[37] Mohammad M. Hamdan. *The Distribution Index in Polynomial Mutation for Evolutionary Multiobjective Optimisation Algorithms: An Experimental Study.* Proceedings of International Conference on Electronics Computer Technology, 2012.

[38] S.A. Moosavi, M. Mirzaei, and J. Roshanian. *The Multidisciplinary Design Optimization of a Reentry Vehicle Using Parallel Genetic Algorithms.* Journal of Aerospace Science and Technology, Vol 7, No. 1, 2010.

[39] Claudio Cavallero, Cosimo Chiarelli, Vincenzo Mareschi, Alessio Davite, Federico Gallizio, Edmondo Minisci, and Martins Sudars. *Multi-disciplinary shape optimization of an entry capsule integrated with custom neural network approximation and multi-delity approach.* Eurogen 2011 Conference, 2011.

[40] Hui Li and Qingfu Zhang. *Comparison Between NSGA-II and MOEA/D on a Set of Multiobjective Optimization Problems with Complicated Pareto Sets.* Technical Report CES-476, University of Essex, 2009.

[41] Yang Ma, Tao Yang, Zhiwei Feng, and Qingbin Zhang. *Hypersonic lifting body aerodynamic shape optimization based on the multiobjective evolutionary algorithm based on decomposition.* Proc IMechE Part G:J Aerospace Engineering, 2014.

[42] Hui Li and Qingfu Zhang. *MOEA/D: A Multiobjective Evolutionary Algorithm Based on Decomposition.* IEEE Transactions on Evolutionary Computation. Vol. 11, Issue 6, p. 712-731, 2007.

[43] J.E. Spillenaar Bilgen. *Global Ascent Trajectory Optimization of a Space Plane.* TU Delft, Master's thesis, 2017.

[44] H. Li and Q. Zhang. *Multiobjective Optimization Problems With Complicated Pareto Sets, MOEA/D and NSGA-II.* IEEE Transactions on Evolutionary Computation: Vol. 11, Issue 2, April, 2009.

[45] G.P. Sutton and O. Biblarz. *Rocket Propulsion Elements, Seventh Edition.* John Wiley & Sons, Inc, 2001.

[46] Northrop Grumman Corporation. *Propulsion Products Catalog.* Northrop Grumman Corporation, 2018.

[47] Charles D. Brown. *Elements of Spacecraft Design.* American Institute of Aeronautics and Astronautics Inc., 2002.

[48] A. I. Atwood, K. P. Ford, and C. J. Wheeler. *High-Pressure Burning Rate Studies of Solid Rocket Propellants.* EDP Sciences, 2013.

[49] B.J. McBride and S. Gordon. *Computer Program for Calculation of Complex Chemical Equilibrium Compositions and Applications II. User's Manual and Program Description.* NASA, 1996.

[50] Niklas Wingborg and Max Calabro. *Green Solid Propellants for Launchers.* GRAIL project, 2016.

[51] B.T.C. Zandbergen. *TYPICAL SOLID PROPELLANT ROCKET MOTORS, version 2.0.* TU Delft, 2013.

[52] Ashraf F. Ahmed and Suong V. Hoa. *Thermal insulation by heat resistantpolymers for solid rocket motor insulation.* Journal of Composite Materials, 2011.

[53] K. Srinivasan, S. Narayanan, and O. P. Sharma. *Numerical studies on erosive burning in cylindrical solid propellant grain.* Heat Mass Transfer: Vol. 44, pp. 579–585, 2008.

[54] Maurizio Natali, Ivan Puri, Marco Rallini, Josè Kenny, and Luigi Torre. *Ablation modeling of state of the art EPDM based elastomeric heat shielding materials for solid rocket motors.* Computational Materials Science: Vol. 111, January, pp. 460-480, 2016.

[55] C.M. Bhuvaneswari, S.D. Kakade, V.D. Deuskar, A.B. Dange, and Manoj Gupta. *Filled Ethylene-propylene Diene Terpolymer Elastomer as ThermalInsulator for Case-bonded Solid Rocket Motors.* Defence Science Journal: Vol. 58, No. 1, January, pp. 94-102, 2008.

[56] Algimantas Fedaravičius, Sigitas Kilikevičius, and Arvydas Survila. *Investigation on the aerodynamic characteristics of a rocket-target for the system "Stinger".* Kaunas University of Technology, 2015.

[57] Anna Tombazzi. *Design of Shape-Conforming Nosecone forOptimal Fluid Flow from Transonic to SupersonicRange.* Honors Research Projects, 2018.

[58] Y.Amini, H.Emdad, K.Akramian, and F.Bordbar. *Investigation of the common nose cone shapes in different gas mixtures in high Knudsen numbers.* Scientia Iranica: Volume 19, Issue 6, Pages 1511-1518, 2012.

[59] B.T.C. Zandbergen. *AE1222-II: Aerospace Design Sy stems Engineering Elements I.* TU Delft, 2019.

[60] NASA CubeSat Launch Initiative. *Basic Concepts and Processes for First-Time CubeSat Developers.* NASA, 2017.

[61] *ISIS ISIPOD 1-Unit CubeSat deployer.* https://www.cubesatshop.com/product/1-unit-cubesat-deployer/, (Visited on 13-03-2020).

[62] *Payload Adapter Systems for Small Satellites.* https://www.cubesatshop.com/product/payload-adapter-systems-small-satellites/, (Visited on 13-03-2020).

[63] ISIS. *ISIPOD CubeSat Deployer.* https://www.isispace.nl/product/isipod-cubesat-deployer/, (Visited on 13-03-2020).

[64] Austin Williams, Jordi Puig-Suari, and Marco Villa. *Low-cost, low mass avionics system for a dedicated Nano-Satellite launch vehicle.* IEEE, 2015.

[65] W.B. Blake. *Missile DATCOM User Manual-1997 FORTRAN 90 Revision.* Wright Patterson Air Force Base, AFRL-VA-WP-TR-1998-3009, 1998.

[66] F. Castellini. *Global optimization techniques in space mission design.* Politecnico di Milano, 2008.

[67] F.M. Engelen. *Quantitative risk analysis of unguided rocket trajectories.* TU Delft, Master's thesis, 2012.

[68] A. Pagano. *Global Launcher Trajectory Optimization for Lunar Base Settlement.* TU Delft, 2010.

[69] Jan Vandamme. *Assisted-Launch Performance Analysis.* TU Delft, Master's Thesis, 2012.

[70] Thomas J. Sooy and Rebecca Z. Schmidt. *Aerodynamic Predictions, Comparisons, and Validations Using Missile DATCOM (97) and Aeroprediction 98 (AP98).* JOURNAL OF SPACECRAFT AND ROCKETS: Vol. 42, No. 2, March–April, 2005.

[71] Jane's Strategic Weapon Systems. *RIM-66/-67/-156 Standard SM-1/-2 and Standard SM-3.* `http://www.airbase.ru/forum/files/00000359/Standart_missiles.pdf`, 2002.

[72] Missile Threat: CSIS. *Standard Missile-3 (SM-3).* https://missilethreat.csis.org/defsys/sm-3/, 2018.

[73] Ankit Panda. *US to Test SM-3 Block IIA Missile Against ICBM Target By End of 2020.* The Diplomat, 2020.

[74] Mark Cancian. *Project on Nuclear Issues: A Collection of Papers from the 2016 Nuclear Scholars Initiative and PONI Conference Series.* Rowman Littlefield, 2017.

[75] *U.S. Navy Standard Missile Family.* `https://www.alternatewars.com/BBOW/Weapons/US_Standard_Missiles.htm`, (Visited on 08-10-2019).

[76] J.W.Cornelisse, H.F.R. Schoyer, and K.F. Wakker. *Rocket Propulsion and Spaceflight Dynamics.* Pitman, 1979.

[77] E. Mooij and D. Dirkx. *Propagation and Optimization Environment Models Lecture Slides.* TU Delft, 2019.

[78] E. Mooij. *Re-entry Systems Lecture Notes.* TU Delft, 2017.

[79] COESA. *1976: U.S. Standard Atmosphere.* NOAA, 1976.

[80] K. H. Well. *Neighbouring vehicle design for a two-stage launch vehicle.* Advanced Design Problems in Aerospace Engineering: Advanced Aerospace Systems. Vol. 1. Springer US, 2004.

[81] R. G. Brusch. *Trajectory optimization for the atlas/centaur launch vehicle.* Conference on Decision and Control and Symposium on Adaptive Processes, 1976.

[82] F. M. Perkins. *Derivation of Linear-Tangent Steering Laws.* Aerospace Corporation, 1966.

[83] A. E. J. Bryson and Y. C. Ho. *Applied Optimal Control.* John Wiley and Sons Inc., 1979.

[84] P. Riatti. *Optimal Control and Near-Optimal Guidance for the Ascent of ARIANE 5.* Master Thesis, University of Stuttgart, 1997.

[85] J. D. Anderson. *Fundamentals of Aerodynamics.* McGRAW-HILL Education, 2016.

[86] D. R. Chapman. *An approximate analytical method for studying entry into planetary atmospheres.* NASA, 1959.

[87] ASTOS. *Astos Model Reference Manual.* Astos Solutions, 2007.

[88] Orbital Sciences Corporation. *Pegasus User's Guide.* Orbital Sciences Corporation, 2007.

[89] Michael R. Mendenhall, Daniel J. Lesieutre, C. Helen Whittaker, Robert E. Curry, and Bryan Moulton. *Aerodynamic Analysis of Pegasus - Computations vs Reality.* AIAA: 31 st Aerospace Sciences Meeting Exhibit, 1993.

[90] K. R. Jackson, W. H. Enright, and T. E. Hull. *A Theoretical Criterion for Comparing Runge-Kutta Formulas.* SIAM Journal on Numerical Analysis: Vol. 15, No. 3, pp. 618-641, 1978.

[91] O. Montenbruck and E. Gill. *Satellite Orbits: Models, Methods, Applications.* Springer, 2005.

[92] Erwin Fehlberg. *Low-order classical Runge-Kutta formulas with stepsize control and their application to some heat transfer problems.* NASA, 1969.

[93] *VEGA User's Manual Issue 4.* Arianespace, 2014.

[94] *VEGA: Realising Europe's Small Launcher.* ESA, 2002.

[95] M. Calabro, A. Dufour, and A. Macaire. *Optimization of the Propulsion for Multistage Solid Rocket Motor Launchers.* Acta Astronautica: Vol.50, No.4, pp.201–208, 2002.

[96] C. Zanotti and P. Giuliani. *Pressure deflagration limit of solid rocket propellants: Experimental results.* Combustion and Flame: Vol. 98, Issues 1–2, 1994.

[97] Edward T. McHale and Guenther von Elbe. *The Deflagration of Solid Propellant Oxidizers.* Combustion Science and Technology: Vol. 2, Issue 4, 1970.

[98] Thomas Pedersen and Flemming Nyboe. *HEAT-1X / Tycho Brahe.* Copenhagen Suborbitals, 2011.

[99] Rainer Storn. *On the Usage of Differential Evolution for Function Optimization.* 1996.

[100] *Electron Payload User's Guide.* Rocket Lab, 2019.